

Analog Alchemy: Neural Computation with In-Memory Inference, Learning and Routing

Dissertation

zur

Erlangung der naturwissenschaftlichen Doktorwürde

(Dr. sc. UZH ETH Zürich)

vorgelegt der

Mathematisch-naturwissenschaftlichen Fakultät der Universität Zürich

und der

Eidgenössischen Technischen Hochschule Zürich

von

Yiğit Demirağ

aus der

Türkei

Promotionskommission

Prof. Dr. Giacomo Indiveri (Vorsitz und Leitung)

Prof. Dr. Melika Payvand

Prof. Dr. Benjamin Grewe

Zürich, 2024

YIGIT DEMIRAG

ANALOG ALCHEMY: NEURAL COMPUTATION WITH IN-MEMORY
INFERENCE, LEARNING AND ROUTING

To the engineers and scientists
who will one day build superintelligence;
from whatever materials and circuits,
in whatever form.

ABSTRACT

As neural computation is revolutionizing the field of Artificial Intelligence (AI), rethinking the ideal neural hardware is becoming the next frontier. Fast and reliable von Neumann architecture has been the hosting platform for neural computation. Although capable, its separation of memory and computation creates the bottleneck for the energy efficiency of neural computation, contrasting the biological brain. The question remains: how can we efficiently combine memory and computation, while exploiting the physics of the substrate, to build intelligent systems? In this thesis, I explore an alternative way with memristive devices for neural computation, where the unique physical dynamics of the devices are used for inference, learning and routing. Guided by the principles of gradient-based learning, we selected functions that need to be materialized, and analyzed connectomics principles for efficient wiring. Despite non-idealities and noise inherent in analog physics, I will provide hardware evidence of adaptability of local learning to memristive substrates, new material stacks and circuit blocks that aid in solving the credit assignment problem and efficient routing between analog crossbars for scalable architectures. First, I address limited bit precision problem in binary Resistive Random Access Memory (RRAM) devices for stable training. By introducing a new device programming technique that precisely controls the filament growth process, we enhance the effective bit precision of these devices. Later, we prove the versatility of this technique by applying it to novel perovskite memristors. Second, I focus on the hard problem of online credit assignment in recurrent Spiking Neural Networks (SNNs) in the presence of memristor non-idealities. I present a simulation framework based on a comprehensive statistical model of Phase Change Material (PCM) crossbar array, capturing all major device non-idealities. Building upon the recently developed e-prop local learning rule, we demonstrate that gradient accumulation is crucial for reliably implementing the learning rule with memristive devices. Moreover, I introduce PCM-trace, a scalable implementation of synaptic eligibility traces, a functional block demanded by many learning rules, using volatile characteristics by specifically fabricated PCM devices. Third, I present our discovery of a novel memristor material capable of switching between volatile and non-volatile modes. This reconfigurable memristor, based on halide perovskite nanocrystals, offers a significant advancement in emerging memory technologies, enabling the implementation of both static and dynamic neural variables with the same material and fabrication technique, while holding the world record in endurance. Finally, I introduce Mosaic, a memristive systolic architecture for in memory computing and routing. Mosaic, trained with our novel layout-aware training methods, efficiently implements small-world graph connectivity and demonstrates superior energy efficiency in spike routing compared to other hardware platforms.

ACKNOWLEDGEMENTS

This thesis wouldn't have been possible without many people: scientists, friends, and family. I'm honored to have shared this journey with such curious and driven individuals. Among the many who contributed, there are a few exceptional individuals who were absolutely core to making this happen:

First I'd like to thank my supervisor, Giacomo Indiveri, who is a rare scientist truly channeling his work towards a dream. Over these 5 years, he gave me complete freedom to explore what I believe are the most exciting problems, while providing me with high-bandwidth feedback on demand, with more than 500 emails and many thousands of DMs. He taught me the importance of pushing unusual ideas to the limit. Whenever I came up with an ambitious project goal, he always reminded me to deeply consider the efficiency on the silicon, first. I'm grateful for having been his student.

I've been very fortunate to coincide with Melika Payvand, my co-supervisor, in this particular academic space and time. She is the most curious mind craving to understand the emergence of intelligence from the physics of computation, and her passion is infectious. Together, we traversed the probability trees for nearly every projects in my PhD, and executed against the entropy. Her close friendship is the cherry on the cake; I enjoyed and valued every second of it.

Then there are people I am very lucky to collaborate with and learn from. Rohit A. John, an extraordinary person who taught me the importance of grinding with massive focus while solving hard problems. And Elisa Vianello, who always provided her seamless support and insights that have made hard projects a joyful exploration. And Emre Neftci, whose disruptive scientific ideas deeply resonated with me, and with whom I always enjoyed discussing ideas.

I have to thank Alpha, Anqchi, Arianna, Chiara, Dmitrii, Farah, Filippo, Jimmy, Karthik, Manu, Maryada, Nicoletta, Tristan, and many others, who I hope will forgive me for not being mentioned individually or for resorting to alphabetical order when I did. Thank you for inspiring conversations in INI hallways, night walks in Zurich, and giving me the privilege of calling you, my friends.

During my PhD, I completed two internships at Google Zurich and one research visit at MILA. All of these were fantastic learning experiences, where I got a chance to reshape my research scope. From these experiences, I would especially like to thank Jyrki Alakuijala, Johannes von Oswald, Eyvind Niklasson, Ettore Randazzo, Alexander Mordvintsev, Esteban Real, Arna Ghosh, Jonathan Cornford, Joao Sacramento, Blake Richards, Guillaume Lajoie, and Blaise Aguera y Arcas.

I would also like to extend my thanks to my professors from my Master's degree, particularly Ekmel Ozbay, Bayram Butun and Yusuf Leblebici, for their invaluable support and inspiration.

And to Gizay, for sharing most of the journey and everything we created together.

But most of all, I want to express my deepest gratitude to my mom and dad, who inspired me to be curious, to take the world as a playground, and provided me with a loving home. And to my little brother, Efe, who is the best teammate in every game we play and in life's adventures.

CONTENTS

1	Introduction	1
2	Enhancing Bit Precision of Binary Memristors for Robust On-chip Learning	9
2.1	Introduction	9
2.2	ReRAM Device Modeling	10
2.3	Bit-Precision Enhancing Weight Update Rule	10
2.4	Learning Circuits and Architecture	12
2.5	System-level Simulations	13
2.6	Discussion	14
3	Online Temporal Credit Assignment with Non-volatile and Volatile Memristors	15
3.1	Framework for Online Training of RSNNs with Non-volatile Memristors	15
3.1.1	Introduction	15
3.1.2	Building blocks for training on in-memory processing cores	16
3.1.3	PCM device modeling and integration into neural networks	16
3.1.4	Discussion	23
3.2	Implementing Online Training of RSNNs on a Neuromorphic Hardware	25
3.2.1	From the simulation to an analog chip	25
3.2.2	Discussion	26
3.3	Scalable Synaptic Eligibility Traces with Volatile Memristive Devices	28
3.3.1	Introduction	28
3.3.2	PCM-trace: Implementing eligibility traces with PCM drift	30
3.3.3	Multi PCM-trace: Increasing the dynamic range of traces	31
3.3.4	Circuits and Architecture	32
3.3.5	Discussion	34
4	Discovering Single Material that Switches Between Volatile or Non-Volatile Modes	37
4.1	Introduction	37
4.2	Diffusive Mode of the Perovskite Reconfigurable Memristor	40
4.3	Drift Mode of the Perovskite Reconfigurable Memristor	40
4.4	Reservoir Computing with Perovskite Memristors	42
4.5	Diffusive Perovskite Memristors as Reservoir Elements	43
4.6	Drift Perovskite Memristors as Readout Elements	43
4.7	Classification of Neural Firing Patterns	44
4.8	Discussion	44
4.9	Methods	45
5	Mosaic: An Analog Systolic Architecture for In-Memory Computing and Routing	49
5.1	Introduction	49
5.2	Mosaic Hardware Computing and Routing Measurements	51
5.3	Analog Hardware-aware Simulations	55
5.4	Benchmarking Routing Energy in Neuromorphic Platforms	56
5.5	Discussion	58
5.6	Methods	60
6	Conclusions	65
A	Appendix	69
	Bibliography	93
	Contributions	113
	Publications	115

INTRODUCTION

You've got to listen to the silicon, because it's always trying to tell you what it can do.

Carver Mead

How do we imbue the spark of intelligence into lifeless computational physical substrates? This question has been my quest, inspired by the early pioneers such as McCulloch and Pitts [1], Alan Turing [2] and von Neumann [3], who laid the foundation of modern neural computing. As the field of AI progressively gains superiority in numerous benchmarks, the quest to understand intelligence and to rethink its ideal implementation on a physical substrate has never been more pressing.

While intelligence remains elusive with numerous definitions, learning¹ seems to me to be a cornerstone of intelligence. Whether it is *natural* or *artificial*, the intelligent agent must adapt to survive and replicate. Bacteria can learn to swim away from environments that lower the probability of successful replication [4]. And Artificial Neural Network (ANN) architectures absorbing the datasets better are preferred by AI researchers and industry [5]. This is a common theme; intelligent systems should learn well to last. And any physical implementation of an intelligent system, likewise, needs to implement learning dynamics. However, the computational demands of learning place an enormous burden on existing hardware.

For over 75 years, computing hardware has relied on the von Neumann architecture: synchronous, deterministic, binary logic driving a processing unit that interfaces with a separate memory subsystem. This design excels at executing arbitrary sequential instructions, but it necessitates constant shuttling of data between memory and compute.² Memory hierarchies, with their layers of progressively larger and slower storage, have been the stopgap solution, but fundamentally the bottleneck remains. This non-local memory access is a leading factor in the latency and energy consumption of modern AI systems. In stark contrast, neural computation in biology is inherently intertwined with memory, operating asynchronously, sparsely, and stochastically. This calls for a fundamental rethinking of computing, where neural models and hardware are co-designed with locality and physics-awareness as first principles.

An Alternative Path

This thesis departs from the well-established path of digital accelerator design. The inherent noise tolerance of neural networks presents an opportunity to relax strict precision and determinism requirements in both compute and memory subsystems of digital electronics. In turn, this relaxation unlocks some exotic modes of computation, where subthreshold regime of transistors and raw physics of novel materials can be exploited for neural computation and storage. Historically, this is the essence of neuromorphic engineering, where a deliberate trade-off can be made, favoring low-power and scalability offered by statistical physical processes over theoretical precision of boolean algebra.

This thesis optimizes neural computation across Marr's computational, algorithmic, and implementational levels [6], advocating for the co-design of neural models and hardware with locality and physics-awareness as guiding principles. By pushing critical neural operations to the fundamental level of material physics, engaging electrical, chemical, or even mechanical properties, we explore a new frontier in low-power neural computing.

Specifically, we investigate the following key strategies, which are detailed in the subsequent sections:

¹ dynamic process of adapting to the environmental pressure to improve the probability of survival or replication.

² partially due to the rapid time-multiplexing of resources.

- **Analog In-Memory Computing:** We exploit the physics of volatile (temporary) or non-volatile (permanent) materials to perform critical neural network operations directly within the memory units. This non-von Neumann architecture fundamentally eliminates the need for data movement between memory and compute units, which are traditionally decoupled systems.
- **Local Learning:** We depart from the computationally intensive Back-Propagation Through Time (BPTT) for training, opting instead for local and online gradient-based learning rules. These rules inherently exhibit varying degrees of variance and bias in their estimates of the gradient of an objective function [7]. However, they offer significant advantages in hardware in terms of power efficiency and simplified implementation due to local availability of weight update signals and the elimination of the need for buffering intermediate values.
- **Analog In-Memory Routing:** We bring out locally dense and globally sparse connectivity on neural networks. This connectivity prior allows high utilization of routers with non-volatile materials to efficiently transmit neural activations within cores of analog systolic arrays.
- **Physics-aware Training:** We utilize data-driven optimization to counteract non-idealities inherent to analog technologies. This involves collecting extensive component measurements to model their collective behavior, tailoring learning algorithms and circuits accordingly. Additionally, we employ gradient-based architectural adaptations and weight re-parameterizations for robust on-chip inference and training. Our methods are validated on small-scale fabrications to assess their on-device performance and scalability potential.

In the following section, I will explain memristors, the *prima materia* of our endeavor, that enables and unifies these strategies explored in this thesis.

Memristors for Analog in Memory Neural Operations

Neural network computation, biological or artificial, is fundamentally memory-centric. The human brain operates on $\mathcal{O}(10^{15})$ synapses [8], while Large Language Models (LLMs) like GPT-4 perform non-linear operations on $\mathcal{O}(10^{12})$ parameters [9]. Scaling laws reveal a direct link between parameter count and performance [10], suggesting increasing network size is a reliable path to improved performance in future neural networks.

Given that memory requirements scale quadratically with the number of layers, memory becomes the primary design constraint in neural computing hardware, impacting scalability, throughput, and power efficiency.³

An ideal memory system for neural computing should be high density, low-energy, quick access, and on-chip. However, an ideal memory does not yet exist, as these requirements are often conflicting. High density memories (i.e., DRAM, High Bandwidth Memory (HBM), 3D NAND flash) are off-chip with long time to access, faster memories that don't use capacitors (i.e. SRAM) are larger in area due to transistor count, and high-bandwidth memories (i.e., HBM) are expensive as they require additional banks, ports and channels. That's why memory hierarchy exists, to address this trade-off by using multiple levels of progressively larger and slower storage. Yet, the von Neumann bottleneck persists, with memory access to each layer in the hierarchy (i.e., DRAM \rightarrow on-chip SRAM \rightarrow local SRAM), incurring roughly an order of magnitude more energy and latency penalty. Even in the ideal case of local SRAM, the cost of memory access exceeds that of computation by an order of magnitude. *In-memory computing* offers a compelling

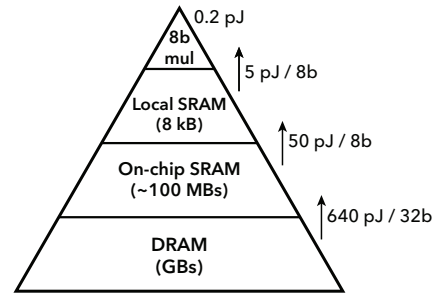


FIGURE 1.1: Importance of data locality is shown in the memory hierarchy as the computation (8b multiplication) costs only the fraction of the energy of memory access, in 45 nm CMOS [11].

³ On edge Tensor Processing Unit (TPU) for instance, memory access can consume over 90% of the total energy, throttle throughput to below 10% peak capacity, and in general dominate the majority of chip area [12].

alternative to data movement by processing data where it is stored, and one of the most promising technologies for in-memory computing is memristors.

Memristors are two-terminal analog resistive memory devices capable of both computation and memory [13]. They have a unique ability to encode and store information in their electrical conductance, which can be altered based on the history of applied electrical pulses [14]. Because a single memristor’s conductance can transition between multiple levels between Low Conductive State (LCS) and High Conductance State (HCS), it can store more than one bit of information (typically between 3 and 5 bits) improving the memory density.⁴ Various memristor types exist, each with distinct operating principles and advantages. For example, PCM relies on the contrasting electrical resistance of amorphous and crystalline phases in chalcogenide materials [16, 17], RRAM operates by altering the resistance of dielectric material through the drift of oxygen vacancies or the formation of conductive filaments [18], and Ferroelectric Random Access Memory (FeRAM) uses the polarization of ferroelectric materials to store and change information [19]. Although the electrical interface to these types does not differ significantly (applying electrical pulses to read or program the conductance), these underlying mechanisms determine the device’s switching speed, footprint, stochasticity, endurance, and energy efficiency.

When implementing functions with memristor forms, it is helpful to categorize by volatility. Non-volatile memristors retain conductance after programming, ideal for weight storage in neural networks. This property extends to in-memory computing to perform dot-product operations [20–22]. When an array of N memristive devices store vector elements G_i in their conductance states, applying voltages V_i to the devices and measuring the resulting currents I_i , the dot product $\sum_{i=1}^N G_i V_i$ can be computed with $\mathcal{O}(1)$ complexity by Ohm’s Law and Kirchoff’s current law. This principle extends to matrix-vector multiplication, enabling neural network inference directly through the analog substrate’s physics. In-memory neural inference has been demonstrated in large prototypes like the PCM-based HERMES chip [23] and RRAM-based NeuRRAM chip [18].

Volatile memristors, however, provide functionality beyond mere storage, and are often less explored. Their conductance decay within 10 ms to 100 ms allows for continuous-time, stochastic accumulate-and-decay functions, approximating low-pass filtering, signal averaging, or time tracking. In neural computations, volatile memristors have been used to implement short-term synaptic [24, 25] and neuronal dynamics [26, 27].

WHY SPIKES? In this thesis, I focus on SNNs, where neural activations are represented as discrete pulses called spikes. This choice is primarily motivated by hardware considerations. Spikes enable extreme spatiotemporal sparsity, aligning well with asynchronous computation where energy consumption directly correlates with spiking events that trigger localized circuits [28]. Mixed-signal spiking neuron circuits inherently act as sigma-delta Analog-to-Digital Converters (ADCs), converting analog neural computation into digital spikes [29] for noise-robust transmission over long distances without signal degradation [30]. Additionally, spiking neurons seamlessly interface with reading and programming of memristive devices and also with event-based sensors [31, 32] through Address-Event Representation (AER) [33] protocol. Spiking communication has even been proposed to mitigate severe heating issues in 3D fabrication using n -ary coding schemes [34].

From a computational perspective, a common argument for spikes is efficient information encoding through precisely utilizing the temporal dimension (e.g., time-to-first-spike [35], phase-coding [36], or inter-spike-interval [37]). Furthermore, the spiking framework allows to formulate hypotheses about biophysical spike-based learning mechanisms in the brain [38–40] and explore the computational capabilities of spiking neural networks [41], as demonstrated in our recent work. While a comprehensive exploration of the advantages of spikes is beyond this thesis’s scope, the primary focus here is their potential for energy-efficient communication on analog substrates, as their unique computational benefits remain to be conclusively demonstrated.

⁴ These attributes are interestingly similar to biological synapses, where the synaptic efficacy is modulated by the history of pre- and post-synaptic activity, and is suggested to take 26 distinguishable strengths (correlated with spine head volume) [15].

State of the Art

Despite their potential, memristors are not without their challenges for neural computing. In this section, I will outline some of these challenges in inference, learning and routing, and state-of-the-art attempts to address them.

Limited bit precision. Programming nanoscale memristive devices, modifies their atomic arrangement, inherently stochastic, non-linear and of limited granularity [42–45]. This analog non-idealities are known to cause significant performance drops in training networks compared to software simulations [46]. Controlled experiments by Sidler *et al.* [22] have demonstrated that the poor training performance is primarily due to insufficient number of pulses switching the device between High Resistive State (HRS) and Low Resistive State (LRS).

Following this, various attempts have been made to improve the bit precision of memristive devices. Optimizing RRAM materials has increased the number of bits per device, but often at the cost of lower ON/OFF ratios (i.e., the ratio of the LRS and HRS), making it harder to distinguish states with small footprint circuits [47–50]. Furthermore, architectural optimizations have been explored, including using multiple binary devices per synapse [51], assigning a number system to multiple devices [52], leveraging stochastic switching [53, 54], and complementing binary memristive devices with capacitors [55]. However, these methods still require complex and large synaptic architectures, limiting scalability.

In Chapter 2, we propose a novel approach to program intrinsically 1-bit RRAM devices to increase their effective bit resolution by precise control of the filament formation.

The credit assignment problem. Learning in any systems is fundamentally about adjusting its parameters to improve its performance. In neural networks, learning involves adjusting weights, represented by the vector W , to optimize the performance, measured by an objective function, $F(W)$. The credit assignment problem refers to the challenge of determining the precise weight adjustments needed for improvement, especially in deep networks where the relationship between individual neurons and overall performance is less clear [56].

Traditionally, Hebbian mechanisms [57] leveraging the timing of pre- and post-synaptic spikes, have been the go-to solution for on-chip learning in the neuromorphic field. This is because Hebbian rules explain a numerous neuroscientific observations [58, 59], possess interesting variance maximization properties [60] but more practically, utilize local signals to the synapse in a simple way, making them easily adaptable to silicon circuits [61–64]. However, Hebbian rules alone had limited success while scaling to large networks, and require heavily crafted architectural biases to achieve hierarchical, disentangled representations.⁵

Backpropagation [68], on the other hand, remains the state-of-the-art algorithm for training modern ANNs, and is one of the pillars of the deep learning revolution. To give an intuition why it works, following the insight from Richards *et al.* [7], let's consider weight changes, ΔW , to be small and objective function to be maximized, F , to be locally smooth, then resulting ΔF can be approximated as $\Delta F \approx \Delta W^T \cdot \nabla_W F(W)$, where $\nabla_W F(W)$ is the gradient of the objective function with respect to the weights. This means that to guarantee improving learning performance ($\Delta F \geq 0$), a principled approach to weight adjustment is to take a small step in the direction of the steepest performance improvement, guided by the gradient ($\Delta F \approx \eta \nabla_W F(W)^T \cdot \nabla_W F(W) \geq 0$). Backpropagation explicitly calculating gradients, while powerful, is unsuitable for online learning on analog substrates due to its need for symmetric feedback weights and distinct forward/backward phases [56]. And for temporal credit assignment, BPTT unrolls the network in reverse time to backpropagate the error gradients, resulting in memory complexity scaling with $\mathcal{O}(kT)$, where k is the number of time steps and T is the number of neurons. This temporal non-locality, necessitates the usage of memory hierarchy to save silicon space, resulting in sacrificing energy efficiency and latency. For this reason, various alternatives have been proposed to estimate gradients while offering better locality, such as feedback alignment [69], Q-AGREL [70], difference

⁵ While this is true, it is possible that end-to-end credit assignment might not be needed [65]. Recent works successfully replacing global backpropagation with truncated layer-wise backpropagation supports this view [66, 67]. Nevertheless, designing the right architecture and local loss functions to guide the truncated credit assignment is still an open question.

target propagation [71], predictive coding [72] and weight perturbation-based methods [73]. These methods exhibit varying degrees of variance (resulting in slower convergence) and bias (leading to poor generalization [74]) in their estimations [7].

However, as long as variance and bias are within reasonable bounds, the learning rule can still be effective, potentially offering a favorable sweet spot between locality and performance. The challenge of local and effective spatio-temporal credit assignment is still a critical frontier in neural processing in analog substrates, demanding new and creative approaches.

In Chapter 3, we address this challenge for the first time, designing material and circuits evolved around gradient calculations, and implementing e-prop [75] local learning rule for Recurrent Spiking Neural Networks (RSNNs) on a memristive chip.

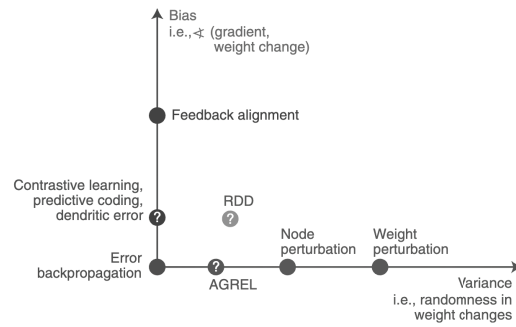


FIGURE 1.2: Bias and variance in learning rules which estimate the gradients, even if they are not explicitly compute gradients. Figure taken from [7].

Programming memristors with non-idealities

for online learning. On-chip learning requires the ability to program the network weights in accordance with the demands of the learning rule. While digital systems often rely on quantization to optimize memory access [76] and associated mitigation techniques such as stochastic rounding [77], gradient scaling [78], quantization range learning [79] and optimizing the weight representation [80], analog memristive systems present unique challenges due to non-idealities such as conductance-dependent, non-linear, stochastic, and time-varying programming responses [81]. Then, it is crucial to identify which digital methods can be effectively transferred to analog systems while promising small footprint and energy overhead.

In Section 3.1 and 3.2, we analyze several practical weight update schemes implementing an online learning rule for mixed-signal systems on a custom simulator, and later validate on a real neuromorphic chip.

Scalable synaptic eligibility traces for local learning. Many high-performing local rules rely on eligibility traces [39, 82–86], slow synaptic memory mechanisms that carry information forward in time. These traces bridge the temporal gap between synaptic activity occurring on millisecond timescale with network errors arising seconds later, helping to solve the distal reward problem [87, 88]. While several neuromorphic platforms [89–91] have incorporated synaptic eligibility traces for learning, this mechanism is one of the most costly building blocks in neural computation, due to quadratic scaling of the number of synapses. Digital implementations suffer from the memory-intensive nature of numerical trace calculations, leading to a von Neumann bottleneck [92, 93]. Even in mixed-signal designs, the slow dynamics of eligibility traces require large capacitors leading to sacrifice of the scalability [94].

In Section 3.3, we propose a novel and scalable implementation of synaptic eligibility traces using volatile memristors.

Unifying volatile and non-volatile materials. Different neural building blocks require different volatility, bit precision, and endurance characteristics from the memristive devices, which are then tailored to meet these demands. For example, ANN inference workloads require linear non-volatile conductance response over a wide dynamic range for optimal weight update and minimum noise for gradient calculation [21, 22, 95]. Whereas SNNs often demand richer and multiple synaptic dynamics simultaneously e.g., short term conductance decay (to implement Short-Term Plasticity (STP) and eligibility traces [82]), non-volatile device states (to represent synaptic efficacy) and a probabilistic nature (to mimic synaptic vesicle releases [24]). However, optimizing different active memristive material for each of these features limits their suitability to a wide range of computational frameworks and ultimately increases the system complexity for most demanding applications. Moreover, these diverse specifications cannot always be implemented by combining

different types of memristors on a monolithic circuit e.g., volatile and non-volatile, binary and analog, due to the incompatibility of the fabrication processes. Although some prototype materials have been proposed to exhibit dual-functional memory [96, 97], the dominance of one of the mechanisms often results in poor switching performance. Therefore, the lack of universal memristors capable of realizing diverse computational primitives has been a challenge.

In Chapter 4, we present our discovery of a novel memristor type that can be used for both volatile and non-volatile operations based on a simple programming scheme, while achieving a world-record in endurance.

Routing of multi-crossbar arrays for scaling. Scaling neural networks, by increasing layer width or depth, has proven to be a powerful technique for improving performance [98]. However, scaling memristive crossbar array dimensions is hindered by analog non-idealities such as current sneak-paths, parasitic resistance, capacitance of metal lines, and yield limitations [99–101]. For this reason, large-scale systems need to adapt multiple crossbars of manageable dimensions [102], but this introduces the overhead of routing activities, especially with long wires along the source, router and destination. To reduce wiring length, three-dimensional (3D) technology to vertically stack logic, crossbar arrays, and routers has been proposed [34, 102], but the fabrication complexity and cost of 3D integration are currently prohibitive. Today’s most advanced multi-crossbar neuromorphic chips, e.g., HERMES [23] and NeuRRAM [18], still rely on off-chip communication for routing, strongly diminishing communication energy efficiency. This necessitates the development of efficient on-chip routing mechanisms to achieve energy-efficient communication. When the routing is optimized for communicating events through the on-chip AER protocol, the designer faces a trade-off between source-based and destination-based routing. Source-based routing offers the flexibility of per-neuron Content Addressable Memory (CAM) memory as used by DYNAP-SE [103], but this comes at the cost of increased chip area and slower memory access. Destination-based routing, while more area-efficient, sacrifices some degree of network configurability.

In Chapter 5, we propose and fabricate a novel memristive in-memory routing core that can be reconfigured to route signals between crossbars, enabling dense local, sparse global connectivity with orders of magnitude more routing efficiency compared to other SNN hardware platforms.

Thesis Overview

This thesis explores the path towards intelligent and low-power analog computing substrates, embracing the Bitter Lesson [104] and addressing some of the challenges in learning and scale. It consists of six selected publications, which I have coauthored with amazing electrical engineers, computer scientists, material designers and neuroscientists. My individual contributions to the work presented in each chapter are clarified and outlined in Appendix 4.

In the first part, we focus on developing mixed-signal learning circuits targeting memristive weights in single-layer feedforward SNN architectures. We address the limited resolution and device-to-device and cycle-to-cycle variability of binary RRAM weights, aiming to enable on-chip learning. Building upon the observation of Ielmini [105] that filament size in RRAM can be precisely controlled by compliance current, we introduce a programming circuitry that modulates synaptic weights based on the estimated gradients using a modified Delta Rule [106]. This approach achieves multi-level weight resolution within the conductance of intrinsically binary switching RRAM devices. We model variability of device responses to our new compliance current programming scheme, I_{CC} to G_{LRS} , from experimental measurements on a 4kb HfO₂-based RRAM array, and adjust our implementation accordingly. We validate our approach and circuits through simulations for standard Complementary Metal-Oxide-Semiconductor (CMOS) 180nm processes and system simulations on the MNIST dataset. This codesign of algorithm, material, and circuit properties establishes a significant building block for single-layer on-chip learning with memristive devices. Furthermore, in Chapter 4, we demonstrate that our programming

scheme can also be applied, with even more linear response, to novel perovskite memristors.

In Chapter 3, we extend our focus to more challenging task of training RSNNs on-chip, addressing the complexities of online temporal credit assignment with memristive devices for in-memory computing. Our work encompasses three complementary efforts: 1) given a recent local learning rule development for RSNNs [75], investigating how to reliably program analog devices based on a realistic PCM model on simulations, 2) validating these results on a PCM-based neuromorphic chip, and 3) proposing a scalable implementation of synaptic eligibility traces, a crucial component of many local learning rules, using volatile memristors.

To achieve this, we start with developing a PyTorch [107]-based simulation framework based on a comprehensive statistical model of a PCM crossbar array, capturing the major device non-idealities: programming noise, read noise, and temporal drift [81]. Our selected learning rule, e-prop, estimates the gradient with nice locality constraints, but it is not known how to reflect the gradient signal reliably while programming memristors with non-idealities. This framework enables benchmarking four commonly practiced memristor-aware weight update mechanisms (Sign-Gradient Descent [108], stochastic updates [81], multi-memristor updates [109] and mixed-precision [110]), to reliably program memristors conductances based on estimated gradients on generic regression tasks. We show that mixed-precision update scheme is superior by accumulating gradients on a high-precision memory (similar to quantization-aware-training methods [111]), allowing for a lower learning rate and improved alignment of weight update magnitudes with the PCM’s minimum programmable conductance change. It also reduces the total number of write pulses by 2-3 orders of magnitude, reducing energy spent on costly memristive programming and mitigating potential endurance issues. Furthermore, we verified previous digital implementations [77] of the stochastic update working well down to 8-bit precision digital simulations.

Following simulations, the next step is to validate it on a physical neuromorphic chip. We implemented the e-prop learning rule on the HERMES chip [23], fabricated in 14nm CMOS, with four 256x256 PCM crossbar arrays in a differential parallel setup. We programmed all weights of a RSNN onto physical PCM devices across HERMES cores for in-memory inference. On-chip training was controlled by a digital coprocessor implementing a mixed-precision algorithm to accumulate gradients on a high-precision memory unit. Our mixed-precision training on HERMES achieved performance competitive with conventional software simulations, maintained a regularized firing rate, and significantly reduced the number of PCM programming pulses, enhancing energy efficiency. Our results demonstrates the first successful implementation of a gradient-based, powerful online learning rule for RSNNs on an analog substrate. While the mixed-precision technique requires an additional high-precision memory unit, we demonstrate that inference can be in-memory, and off-chip guided learning can be activated as needed with minimal analog device programming.

Local learning rules, including e-prop, often require synaptic eligibility traces [39, 82–86], posing a scaling challenge for analog hardware due to their $O(N^2)$ area scaling, where N is the number of neurons. This challenge is exacerbated by increased time-constant requirements, as larger capacitors are needed for implementation. To address this, we introduce PCM-trace, a novel small-footprint circuitry leveraging the inherent conductance drift of PCM to emulate eligibility traces for local learning rules. We exploit the material bug - the structural relaxation and temporal conductance drift in PCM’s amorphous regime [112], described by $R(t) = R(t_0)(\frac{t}{t_0})^\nu$ - turning it into a feature. Our optimized material choice allows gradual SET pulses to accumulate the trace, while conductance naturally decays over seconds. We also introduce a multi-PCM-trace configuration, distributing synaptic traces across multiple PCM devices to significantly improve dynamic range. Experimental results on 130nm CMOS technology confirm that PCM-trace can maintain eligibility traces for over 10 seconds while offering more than 11x area savings compared to conventional capacitor-based trace implementations [94].

In Chapter 4, we introduce a state-of-the-art memristive material based on halide perovskite nanocrystals that can be dynamically reconfigured to exhibit volatile or non-volatile behavior. This is motivated by the fact that many in-memory neural computing systems demand devices with specific switching characteristics, and existing memristive devices cannot be reconfigured to meet these diverse volatile and non-volatile switching requirements. To achieve this, we develop a cesium lead bromide nanocrystals capped with organic ligands as the active switching matrix and silver as the active electrode. This design leverages the low activation energy of ion migration in halide perovskites to achieve both diffusive (volatile) and drift (non-volatile) switching. By actively controlling the compliance current (I_{cc}) following our prior work at Chapter 2, the magnitude of ion flux is adjusted, enabling on-demand switching between the two modes. This control mechanism allows for the selection of diffusive dynamics with low I_{cc} ($1\mu\text{A}$) for volatile behavior and drift kinetics with higher I_{cc} (1 mA) for non-volatile memory operation. Moreover, our measurements demonstrated that memristors using perovskite nanocrystals capped with OGB, achieve a record endurance in both volatile and non-volatile modes. We attribute this superior performance to the larger OGB ligands, which better insulate the nanocrystals and regulate the electrochemical reactions responsible for switching behavior.

In Chapter 5, we switch gears and focus on the scalability of memristive architectures in neuro-morphic systems, a challenge hindered by analog non-idealities of crossbar arrays. We introduce Mosaic, a novel memristive systolic array architecture consisting of interconnected Neuron Tiles and Routing Tiles, both implemented with RRAM integrated 130nm CMOS technology.

Each Neuron Tile, per usual, is a crossbar array of memristors storing network weights for a RSNN layer with Leaky Integrate-and-Fire (LIF) neurons. These neurons emit spikes based on integrated synaptic inputs, transmitting them to neighbouring tiles through Routing Tiles. The Routing Tiles, also based on memristor arrays, define the connectivity patterns between Neuron Tiles. The resulting structure then becomes a small-world graph with dense local and sparse long-range connections, similar to the connectivity found in biological brains ⁶.

Our in-memory routing approach necessitates careful optimization of connectivity during offline training to prune RSNNs into a Mosaic-compatible, small-world graph. We introduce a novel hardware layout-aware training method that considers the physical layout of the chip and optimizes neural network weights using either gradient-based or evolutionary algorithms [113].

In-memory routing and optimization for sparse long-range and locally dense communication in Mosaic result in significant energy efficiency in spike routing, surpassing other SNN hardware platforms by at least one order of magnitude, as demonstrated by hardware measurements and system-level simulations. Notably, due to its layout-aware structured sparsity, Mosaic achieves competitive accuracy in edge computing tasks like biosignal anomaly detection, keyword spotting, and motor control.

⁶ It may not be a coincidence that some of the solutions proposed in this thesis can also be found in the biological brain, whispering of a deep connection between highly optimized silicon substrates and the evolved neural tissue.

ENHANCING BIT PRECISION OF BINARY MEMRISTORS FOR ROBUST ON-CHIP LEARNING

This chapter's content was published in IEEE International Symposium on Circuits and Systems (ISCAS). The original publication is authored by Melika Payvand, Yigit Demirag, Thomas Dalgaty, Elisa Vianello, Giacomo Indiveri.

Analog neuromorphic circuits with memristive synapses offer the potential for power-efficient neural network inference, but limited bit precision of memristors poses challenges for gradient-based training. In this chapter, we introduce a programming technique of the weights to enhance the effective bit precision of initially binary memristive devices, enabling more robust and performant on-chip training. To overcome the problems of variability and limited resolution of ReRAM memristive devices used to store synaptic weights, we propose to use only their HCS and control their desired conductance by modulating their programming compliance current, I_{CC} . We introduce spike-based CMOS circuits for training the network weights; and demonstrate the relationship between the weight, the device conductance, and the I_{CC} used to set the weight, supported with experimental measurements from a 4kb array of HfO₂-based devices. To validate the approach and the circuits presented, we present circuit simulation results for a standard CMOS 180 nm process and system-level simulations for classifying hand-written digits from the MNIST dataset.

2.1 INTRODUCTION

The neural networks deployed on the resource-constrained devices can benefit greatly from online training to adapt to shifting data distributions, sensory noise, device degradation, or new tasks that are not seen in the pretraining. While CMOS architectures with integrated memristive devices offer ultra-low power inference, their use for online learning has been limited [114, 115].

In this chapter, we propose novel learning circuits for SNN architectures implemented by 1T1R arrays. These circuits enable analog weight updates on binary ReRAM devices by controlling their SET operation I_{CC} . In addition to increasing the bit precision of network weights, the proposed strategy allows compact, fast, and scalable event-based learning scheme compatible with the AER interface [116].

Previously significant efforts have aimed to increase the bit precision of memristive devices for online learning through material and architectural optimizations.

MATERIAL OPTIMIZATION Several groups reported TiO₂-based [47–49] and HfO₂-based [50] ReRAM devices with up to 8 bits of precision. However, in all these works, the analog behavior is traded off with the lower available ON/OFF ratio. While the analog behavior is an important concern for training neural networks, cycle-to-cycle and device-to-device variability harms the effective number of bits further when ON/OFF ratio is small. Also, tuning the precise memory state is not always easily achievable in a real-time manner, requiring recursively tuning with an active feedback scheme [50, 117]. Furthermore, some efforts have been focused on carefully designing a barrier level using exhaustive experimental search over a range of materials [47, 48] which makes it difficult to fabricate.

ARCHITECTURE OPTIMIZATION Increasing the *effective* bit resolution has also been demonstrated with architectural advancements. Strategies such as using multiple binary switches to emulate n-bit synapses [51] or exploiting stochastic switching properties for analog-like adaptation [53, 54] have been explored. Alternatively, IBM's approach of using a capacitor alongside two PCM devices to act as an analog volatile memory, increases combined precision but incurs significant area overhead [55]. Recently, a mixed-precision approach has been employed to train

the networks using a digital coprocessor for weight update accumulation [118], but requires digital buffering of weights, gradients and suffers of domain-conversion costs.

Thus, neither device nor architecture optimizations have fully resolved the challenges of low bit precision in memristors for online learning. Prior work by Ielmini [105] observed that the electrical resistance of memristors after a SET operation follows a linear relationship with I_{CC} in a log-log scale, by control over the size of the filament. This critical observation underpins our approach, where we exploit this relationship to directly control device conductance.

To minimize the effect of variability, we adopt an algorithm-device codesign approach. We restrict devices to stay only in their HCS and modulate their conductance by adjusting the programming I_{CC} . Specifically, we derive a technologically feasible online learning algorithm based on the Delta rule [106], mapping weight updates onto the I_{CC} used for setting the device. This co-design offers several advantages: (i) relaxed fabrication constraints compared to multi-bit devices, and (ii) increased state stability due to the use of only two levels per device.

2.2 RERAM DEVICE MODELING

To find the average relationship between the mean of the cycle-to-cycle distribution of the HCS and the SET programming I_{CC} , we performed measurements on a 16×256 (4kb) array of HfO_2 -based ReRAM devices integrated onto a 130 nm CMOS process between metal layers 4 and 5 [119]. Each device is connected in series to the drain of an n-type selector transistor which allows the SET programming I_{CC} to be controlled based on the voltage applied to its gate. The 1T1R structure allows a single device to be selected for reading or programming by applying appropriate voltages to a pair of Source/Bit Lines (SL/BL) and a single Word Line (WL).

All 4kb devices were initially formed in a raster scan fashion by applying a large voltage (4V typical) between the SL and BL to induce a soft breakdown in the oxide layer and introduce conductive oxygen vacancies. After forming, each device was subject to sets of 100 RESET/SET cycles over a range of SET I_{CC} s between $10\mu\text{A}$ and $400\mu\text{A}$, where the resistance of each device was recorded after each SET operation. The mean of all devices' median resistances over the 100 cycles, at a single I_{CC} , gives the average relationship between HCS median and SET I_{CC} as in Fig. 2.1. The relationship is seen to follow a line in the log-log plot (power law) and over this I_{CC} range, it allows precise control of the conductance median of the cycle-to-cycle distribution between $50\text{k}\Omega$ and $2\text{k}\Omega$.

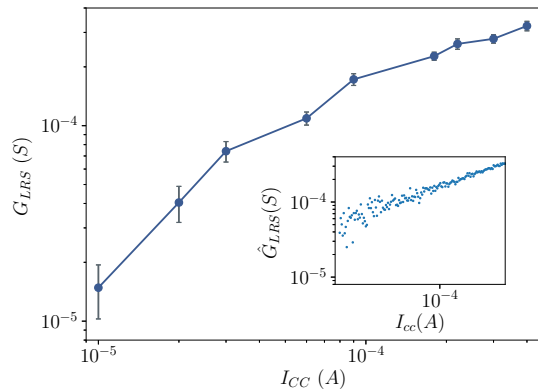


FIGURE 2.1: Mean and standard deviation of the device conductance as a function of the I_{CC} s. The inset shows the samples from the fitted mean and standard deviation used for the simulations.

2.3 BIT-PRECISION ENHANCING WEIGHT UPDATE RULE

The learning algorithm is based on the Delta rule, the simplest form of the gradient descent for single-layer networks. In our implementation, the objective function is defined as the difference between the desired target output signal y and the network prediction signal \hat{y} , for a given set of input patterns signals x , weighted by the synaptic weight parameters w . Then the Delta rule can be used to calculate the change of the weights connecting a neuron i in the input layer and a neuron j at the output layer as follows:

$$\Delta w_{ji} = \eta(y_j - \hat{y}_j)x_i = \eta\delta_j x_i, \quad (2.1)$$

Algorithm 1: Delta Rule implementation with dual-memristors

```

 $w_{ji1} = \text{rand}(), w_{ji2} = \text{rand}();$ 
while  $t < \text{simDuration}$  do
     $\delta_j = |\hat{y} - y|;$ 
    if @Pre and  $\delta_j > \delta_{th}$  then
        forall  $w_{ji}$  do
             $I_{ji1}, I_{ji2} = \text{READ}(w_{ji1}, w_{ji2});$ 
             $I_1 = I_{ji1} * c_1;$ 
             $I_2 = I_{ji2} * c_1;$ 
            if  $(\hat{y} - y) > 0$  then
                 $S_1 = I_1 + \eta \delta_j;$ 
                 $\text{ICC}_{ji1} = S_1 * c_2;$ 
                 $S_2 = I_2 - \eta \delta_j;$ 
                 $\text{ICC}_{ji2} = S_2 * c_2;$ 
            else
                 $S_1 = I_1 - \eta \delta_j;$ 
                 $\text{ICC}_{ji1} = S_1 * c_2;$ 
                 $S_2 = I_2 + \eta \delta_j;$ 
                 $\text{ICC}_{ji2} = S_2 * c_2;$ 
            end
             $\text{RESET}(w_{ji1}, w_{ji2});$ 
             $\text{SET}(w_{ji1}, w_{ji2});$ 
        end
    end
end

```

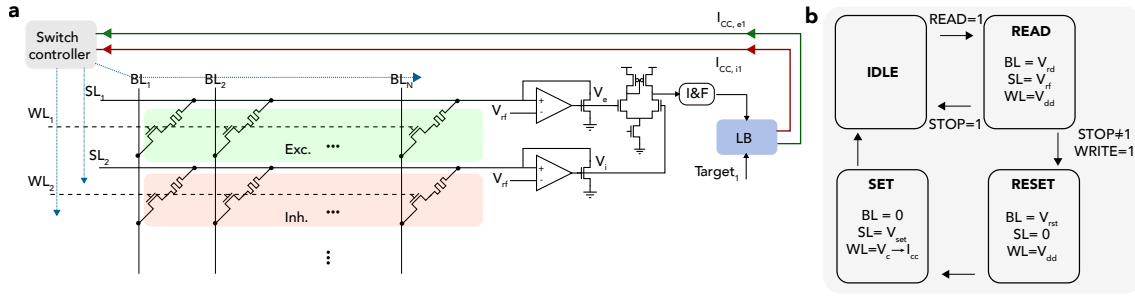


FIGURE 2.2: Event-based neuromorphic architecture using online learning in a 1T1R array (a), and the asynchronous state machine used as the switch controller applying the appropriate voltages on the BL, SL and WL of the array for online learning.

where δ_j is the error, and η is the learning rate. To implement this using memristive synaptic architecture, we represent each synaptic weight w , by the combined conductance of two memristors, w_{ji1} and w_{ji2} , arranged in a push-pull differential configuration. This scheme extends the effective dynamic range of a single synapse to capture the negative values.

During the network operation, the target and the prediction signals are compared continuously to generate the error signal. With the arrival of a pre-synaptic event, if the error signal is larger than a small error threshold, the weight update process is initiated. The small error threshold that creates the "stop-learning" regime has been proposed to help the convergence of the neural networks with stochastic weight updates [120].

The implementation of the synaptic plasticity consists of three phases (Alg. 1). First, a READ operation is performed on every excitatory and inhibitory memristor to determine their conductance. Then the resulting current values (I_{ji1} and I_{ji2}) are scaled to the level of the error signal. Second, the current value proportional to the amount of the weight change $\eta\delta_j x_i$ is summed up with the scaled READ current to represent the desired conductance strength to be programmed. Finally, these currents are further scaled to a valid I_{CC} range using linear scaling constants c_1 and c_2 . To provide a larger dynamic range per synapse, the conductance of both memristors are updated with a push-pull mechanism considering the sign of the error (i.e. if the conductance of one memristor increased, the conductance of the complementary memristor is decreased, and vice-versa).

2.4 LEARNING CIRCUITS AND ARCHITECTURE

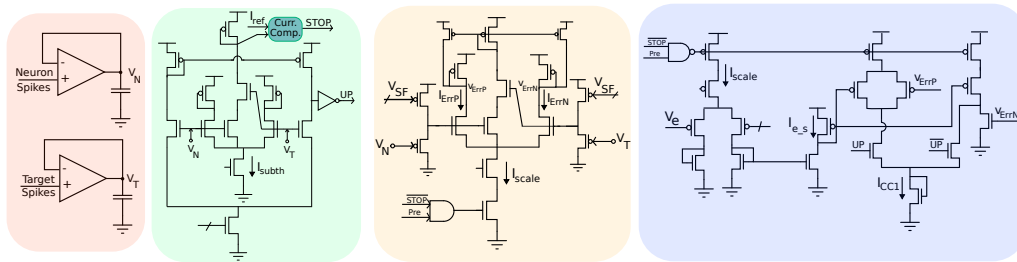


FIGURE 2.3: Learning circuits generating the I_{CC} for updating the devices based on the distance between the neuron and its target frequency. Highlighted in red is the Gm-C filters, low pass filtering the neuron and target spikes giving rise to V_N and V_T . In green and orange, the error between the two is calculated generating positive (I_{ErrP}) and negative (I_{ErrN}) errors, unless error is small and STOP signal is high. In purple, V_e , the excitatory voltage from Fig.2.2, regenerates the read current and is scaled to I_{scale} producing I_{e_s} . Based on the error sign (UP), I_{CC1} is either the sum of I_{e_s} and I_{Err} or the subtraction of the two.

NEUROMORPHIC ARCHITECTURE Figure 2.2a illustrates the event-based neuromorphic architecture encompassing the learning algorithm. It consists of a 1T1R array, a Switch Controller,

Leaky Integrate and Fire (I&F) neurons and a learning block (LB). Every neuron receives excitatory and inhibitory currents from two rows of the 1T1R array respectively.

With the arrival of every event through the AER interface (not shown), two consecutive READ and WRITE signals are generated [115]. Based on these signals, the asynchronous state machine in Fig. 2.2b controls the sequence so that the SLs, BLs and the WLs of the array are driven by the appropriate voltages such that: device is read, its value is integrated by the I&F neuron; the error value is updated through the learning block (LB), generating I_{CC1} and I_{CC2} (section 2.3); Based on these values, the excitatory and inhibitory devices are programmed.

LEARNING CIRCUITS Based on Alg. 1 and data from Fig. 2.1, we have designed circuits that generate the appropriate I_{CC} , based on the firing rate distance between the neuron and its target. Figure 2.3 presents these circuits. The spikes from the neurons and the target are integrated using subthreshold Gm-C filters highlighted in red generating V_N and V_T . These voltages are subtracted from one another using a subthreshold "Bump" (*subBump*) circuit [121] highlighted in green, and an above-threshold "Bump" circuit (*abvBump*) in orange.

subBump circuit compares V_N and V_T giving rise to the error currents when neuron and the target frequencies are far apart and generates the STOP signal when the error is small and in the stop-learning range (δ_{th}) [120, 122]. STOP signal gates the tail current of all the above-threshold circuits and thus substantially reduce the power consumption when the learning is stopped. Moreover, input events are also used as another gating mechanism. *abvBump* circuit subtracts V_N and V_T and scales it to I_{scale} , equal to the maximum I_{CC} required based on Fig. 2.1. Based on the error sign (UP), the scaled error current is summed with or subtracted from the scaled device current generating the desired I_{CC} (Alg. 1). This circuit is highlighted in purple.

CIRCUIT SIMULATIONS RESULTS Figure 2.4a depicts the positive and negative error currents, STOP-learning signal, and the I_{CC1} and I_{CC2} currents. The error currents follow a Sigmoid which can be approximated by a line for error values between -1 and 1. As is explained in Alg. 1, for positive errors, I_{CC2} (I_{CC1}) follows the summation (subtraction) of the error current with the scaled device current, while for the negative errors, it is the opposite. Figure 2.4b illustrates the dependence of the I_{CC} on the current value of the devices which shifts the error current curve up or down.

2.5 SYSTEM-LEVEL SIMULATIONS

We performed SNN simulations with BRIAN2 [123] to evaluate the performance of our proposed update scheme, incorporating the device models (see Fig. 2.1) with stochastic weight changes. Our goal was to achieve a test accuracy comparable to the artificial neural networks trained with backpropagation with Single-precision floating-point format (FP32) precision on the digital hardware.

We evaluated our network on the MNIST handwritten digits dataset [124] using the first five classes (30596 training and 5139 testing images, each 28×28 pixels). We trained a fully connected, single-layer spiking network with 784 input LIF neurons and 5 output LIF neurons. Each input image was presented for 100 ms, with pixel intensity encoded as Poisson spikes with a rate of $[0, 200]$ Hz. At the output layer, spikes were counted per neuron during each stimulus, and the neuron with the maximum firing rate was selected as the network prediction. The error signal was calculated as the difference between low-pass filtered network output spikes and low-pass filtered target spikes, encoded as Poisson spikes at 40 kHz.

We modeled the cycle-to-cycle variability of I_{CC} dependent G_{LRS} conductance using a Gaussian distribution with I_{CC} -dependent mean and standard deviation, as described in Section 2.2. This variability model was applied to all synaptic devices in the simulation, and we achieved the test accuracy of 92.68% after training for three epochs.

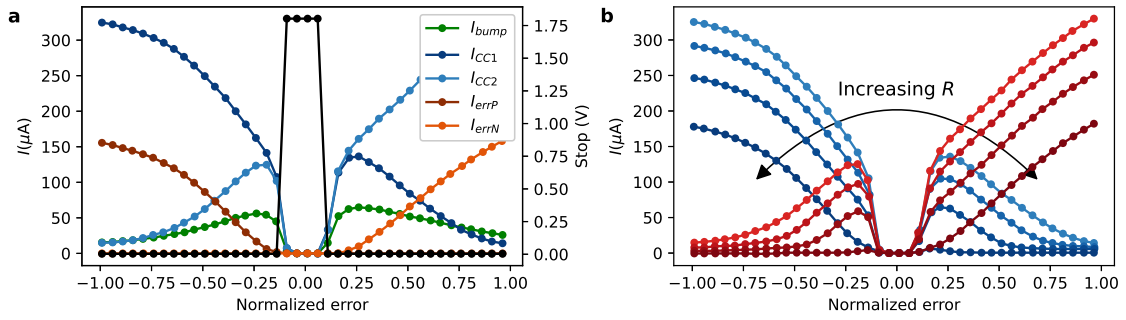


FIGURE 2.4: (a) Error current, STOP learning signal and I_{CC} as a function of the normalized error between the target and the neuron frequencies. (b) Change of the I_{CC1} (red) and I_{CC2} (blue) as a function of the error and the resistance value of the devices.

2.6 DISCUSSION

Significant effort is underway to develop learning algorithms for SNNs due to their potential for highly parallel, low-power processing. However, a substantial gap exists between these algorithms and their hardware implementation due to noise, variability, and limited bit precision. This gap underscores the importance of technologically plausible learning algorithms rooted in device physics and measurements [125]. Our work, exploiting ReRAM current compliance I_{CC} for weight updates, represents a step in this direction.

POWER CONSUMPTION AND SCALABILITY While the learning block can generate up to 100s of μA s of I_{CC} for large errors, design considerations such as event and STOP-learning signal gating mitigate average power consumption. Peak current per learning block ranges from 1 to 600 μA , depending on the network error. Leveraging the Poisson distribution of events (due to thermal noise), we can assume that only one column of devices is programmed at a time. Therefore, peak power scales sublinearly with the number of neurons (linear in the worst case). This sublinear scaling implies that power consumption does not fundamentally limit scalability. However, with Poisson-distributed input events and a maximum frequency per input channel, an upper bound for array size exists, determined by event pulse width and tolerance to missing events [54].

THE NONLINEAR EFFECT The power-law relationship between $I_{CC} \rightarrow G_{LRS}$ (Fig. 2.1) introduces a nonlinear mapping of weight updates. This nonlinearity slightly biases the weight update away from the optimal values calculated by the Delta rule. Further investigation into mitigating this bias through calibration or algorithmic compensation could improve learning accuracy.

In this chapter, I presented a technologically plausible learning algorithm that leverages the compliance current of binary ReRAMs to generate variable, multi-level conductance changes. Our comprehensive co-design approach spans multiple levels of abstraction, from device measurements to algorithm, architecture, and circuits. We believe this work represents a significant step toward realizing always-on, on-chip learning systems. As we will see in Chapter 4, our method can be extended to other non-volatile materials, providing a broader pathway for on-chip learning hardware.

ONLINE TEMPORAL CREDIT ASSIGNMENT WITH NON-VOLATILE AND VOLATILE MEMRISTORS

This chapter builds upon three conceptually linked works. My initial concept of investigating the online credit assignment problem for recurrent neural networks implemented with non-ideal non-volatile memristive devices [126], and the subsequent utilization of eligibility traces with volatile memristors for scalability [127], laid the foundation for this research. These concepts were further validated through real-hardware testing in collaboration with IBM Research Zürich [128].

3.1 FRAMEWORK FOR ONLINE TRAINING OF RSNNs WITH NON-VOLATILE MEMRISTORS

Training RSNNs on ultra-low-power hardware remains a significant challenge. This is primarily due to the lack of spatio-temporally local learning mechanisms capable of addressing the credit assignment problem effectively, especially with limited weight resolution and online training with a batch size of one. These challenges are accentuated when using memristive devices for in-memory computing to mitigate the von Neumann bottleneck, at the expense of increased stochasticity in recurrent computations.

To investigate online learning in memristive neuromorphic Recurrent Neural Network (RNN) architectures, we present a simulation framework and experiments on differential-architecture crossbar arrays based on an accurate and comprehensive PCM device model. We train a spiking RNN on regression tasks, with weights emulated within this framework, using the recently proposed e-prop learning rule. While e-prop truncates the exact gradients to follow locality constraints, its direct implementation on memristive substrates is hindered by significant PCM non-idealities. We compare several widely adopted weight update schemes designed to cope with these non-idealities and demonstrate that only gradient accumulation can enable efficient online training of RSNNs on memristive substrates.

3.1.1 Introduction

RNNs are a remarkably expressive [129] class of neural networks, successfully adapted in domains such as audio/video processing, language modeling and Reinforcement Learning (RL) [130–135]. Their power lies in their architecture, enabling the processing of long and complex sequential data. Each neuron contributes to network processing at various times in the computation, promoting hardware efficiency by the principle of reuse and being the dominant architecture observed in the mammalian neocortex [136, 137]. However, training RNNs under constrained memory and computational resources remains a challenge [83].

Current hardware implementations of neural networks still lag behind the energy efficiency of biological systems, largely due to data movement between separate processing and memory units in von Neumann architectures. Compact nanoscale memristive devices have gained attention for implementing artificial synapses [99, 138–142]. These devices enable calculating synaptic propagation *in-memory* between neurons, breaking the von Neumann bottleneck [92, 93]

Memristive devices are particularly promising for SNNs, especially for low-power, sparse, and event-based neuromorphic systems that emulate biological principles [143, 144]. In these systems, synapses (memory) and neurons (processing units) are arranged in a crossbar architecture (Fig. 3.1a), with memristive devices storing synaptic efficacy in their programmable multi-bit conductance values. This architecture inherently supports the sparse, event-driven nature of SNNs, enabling in-memory computation of synaptic propagation through Ohm’s and Kirchhoff’s Laws. As demonstrated for 32 nm technology [145, 146], memristive crossbar arrays offer higher density and lower dynamic energy consumption during inference compared to traditional Static Random Access Memory (SRAM). Additionally, their non-volatile nature reduces static power consumption associated with volatile CMOS memory. Thus, in-memory acceleration of spiking

RNNs with non-volatile, multi-bit resolution memristive devices is a promising path for scalable neuromorphic hardware in temporal signal processing.

PCM devices are among the most mature emerging resistive memory technologies. Their small footprint, fast read/write operation, and multi-bit storage capacity make them ideal for in-memory computation of synaptic propagation [147, 148]. Consequently, PCM technology has seen increased interest in neuromorphic computing [138, 149–151].

While a single PCM device can achieve 3-4 bits of resolution [152], they exhibit significant non-idealities due to stochastic Joule heating-based switching physics. Molecular dynamics introduce $1/f$ noise and structural relaxation, leading to cycle-to-cycle variation in addition to device-to-device variability from fabrication.

Hardware-algorithm co-design with chip-in-the-loop setups is one approach to address these non-idealities [138]. However, neural network training necessitates iterative evaluation of architectures, learning rule modifications, and hyperparameter tuning on large datasets, which are time and resource-intensive with such setups. In contrast, a software simulation framework with highly accurate statistical model of memristive devices offers faster iteration and better understanding of device effects due to increased observability of internal state variables.

In this work, we investigate whether a RSNN can be trained with a local learning rule despite the adverse impacts of memristive in-memory computing, including write/read noise, conductance drift, and limited bit precision. We build upon the statistical PCM model from Nandakumar *et al.* [81] to faithfully model a differential memristor crossbar array (Section 3.1.3), define a target spiking RNN architecture, and describe the properties of an ideal learning rule, selecting the e-prop algorithm [75] for training (Section 3.1.3.1). We implement multiple memristor-aware weight update methods to map ideal e-prop updates to memristor conductances on the crossbar array, addressing device non-idealities (Section 3.1.3.2). Finally, we present a training scheme exploiting in-memory computing with extreme sparsity and reduced conductance updates for energy-efficient training (Section 3.1.3.4).

3.1.2 Building blocks for training on in-memory processing cores

In this section, we describe the main components of our simulation framework for training spiking RNNs with PCM synapses ¹.

3.1.3 PCM device modeling and integration into neural networks

The nanoscale PCM device typically consists of a $\text{Ge}_2\text{Sb}_2\text{Te}_5$ (GST) switching material sandwiched between two metal electrodes, forming a mushroom-like structure (Fig. 3.1b). Short electrical pulses applied to the device terminals induce Joule heating, locally modifying the temperature distribution within the PCM. This controlled temperature change can switch the molecular configuration of GST between amorphous (high-resistance) and crystalline (low-resistance) states [17].

A short, high-amplitude RESET pulse (typically 3.5 V amplitude and 20 ns duration) increases the amorphous state volume by melting a significant portion of the GST, which then rapidly quenches to form an amorphous configuration. Conversely, a longer, lower-amplitude SET pulse (3.5 V amplitude and 20 ns duration) increases the crystalline volume by raising the temperature to initiate crystal nuclei growth. To read the device conductance, a smaller-amplitude READ pulse (0.2 V amplitude 50 ns duration) is applied to avoid inducing phase transitions.

In practice, PCM programming operations suffer from write/read noise and conductance drift [153]. The asymmetry of SET and RESET operations, along with the nonlinear conductance response to pulse number and frequency, complicate precise programming. Accurately capturing these non-idealities and device dynamics in network models is crucial for realistic evaluation of metrics such as weight update robustness, hyperparameter choices, and training duration.

While comprehensive models exist for describing PCM electrical [45], thermal [154], structural [155, 156], and phase-change properties [157, 158], these models often involve on-the-fly differential equations with uncertain numerical convergence, lack incorporation of inter- and

¹ The code is available at <https://github.com/YigitDemirag/srnn-pcm>

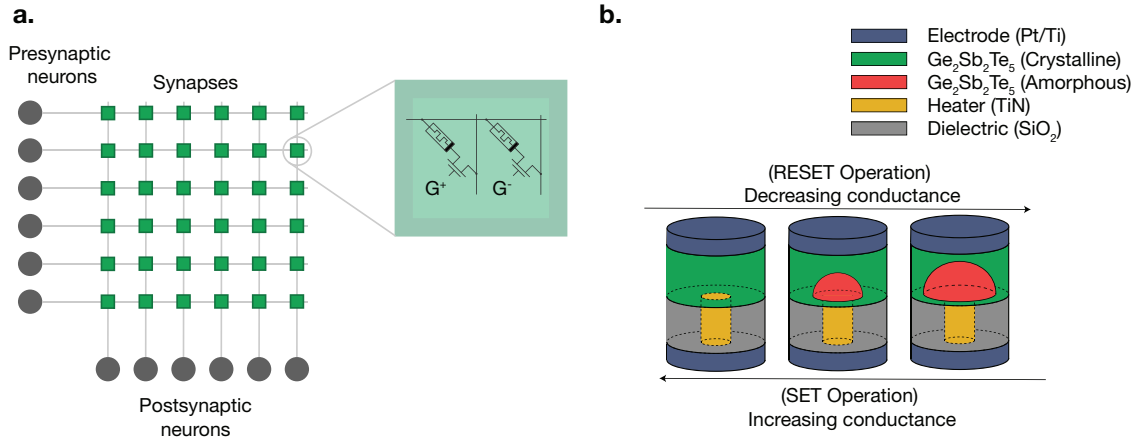


FIGURE 3.1: **a.** PCM devices can be arranged in a crossbar architecture to emulate both a non-volatile synaptic memory and a parallel and asynchronous synaptic propagation using in-memory computation. **b.** Mushroom-type geometry of a single PCM device. The conductance of the device can be reconfigured by changing the volume ratio of amorphous and crystalline regions.

intra-device stochasticity, or are designed for pulse shapes and current-voltage sweeps that do not reflect circuit operating conditions [17].

Therefore, we adopted the statistical PCM model by Nandakumar *et al.* [81], which captures major PCM non-idealities based on measurements from 10,000 devices. This model includes nonlinear conductance change with respect to applied pulses, conductance-dependent write and read stochasticity, and temporal drift (Fig. 3.2). A programming history variable represents the device's nonlinear response to consecutive SET pulses, updated after each pulse. After a new SET pulse, the model samples conductance change (ΔG) from a Gaussian distribution with mean and standard deviation based on programming history and previous conductance. Drift is included using the empirical exponential drift model [156] $G(t) = G(T_0) (t/T_0)^{-\nu}$, where $G(T_0)$ is the conductance after a WRITE pulse at time T_0 , and $G(t)$ is the final conductance after drift. The model also accounts for $1/f$ READ noise [159], which increases monotonically with conductance.

To integrate this model into neural network simulations, we developed a PyTorch-based PCM crossbar array simulation framework [107]. This framework tracks all simulated PCM devices in the crossbar simultaneously, enabling realistic SET, RESET, and READ operations (implementation details in Section A). Section 3.1.3.3 describes how this framework is used to represent synaptic weights in an RNN.

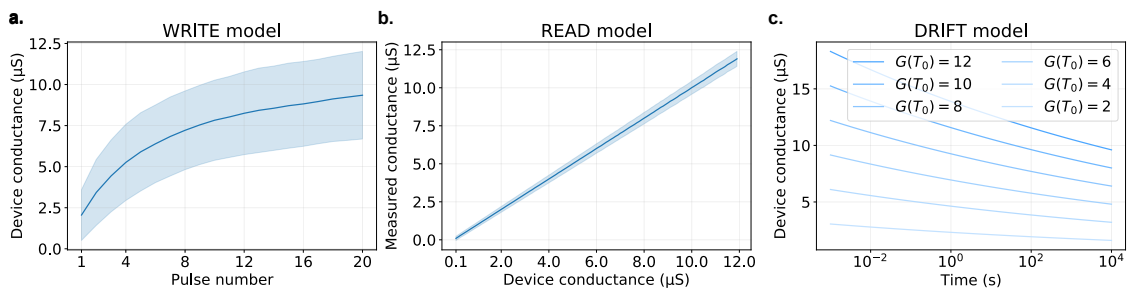


FIGURE 3.2: The chosen PCM model from [81] captures the major device non-idealities. **a.** The WRITE model enables calculation of the conductance increase with each consecutive SET pulse applied to the device. The band illustrates one standard deviation. **b.** The READ model enables calculation of $1/f$ noise, increasing as a function of conductance. **c.** The DRIFT model calculates the temporal conductance evolution as a function time. T_0 indicates the time of measurement after the initial programming of the device.

3.1.3.1 Credit Assignment Solutions for Recurrent Network Architectures

The credit assignment problem refers to the problem of determining the appropriate change for each synaptic weight to achieve the desired network behavior [7]. As the architecture determines the information flow inside the network, the credit assignment solution is intertwined with network architecture. Consequently, many proposed solutions in SNNs landscape are specific to architecture components e.g., eligibility traces [160], dendritic [161] or neuromodulatory [162] signals.

In our work, we select a RSNN with LIF neuron dynamics described by the following discrete-time equations [75]:

$$\begin{aligned} v_j^{t+1} &= \alpha v_j^t + \sum_{i \neq j} W_{ji}^{\text{rec}} z_i^t + \sum_i W_{ji}^{\text{in}} x_i^t - z_j^t v_{\text{th}} \\ z_j^t &= H \left(\frac{v_j^t - v_{\text{th}}}{v_{\text{th}}} \right) \\ y_k^{t+1} &= \kappa y_k^t + \sum_j W_{kj}^{\text{out}} z_j^t \end{aligned} \quad (3.1)$$

where v_j^t is the membrane voltage of neuron j at time t . The output state of a neuron is a binary variable, z_j^t , that can either indicate a spike, 1, or no spike, 0. The neuron spikes when the membrane voltage exceeds the threshold voltage v_{th} , a condition that is implemented based on the Heaviside function H . The parameter $\alpha \in [0, 1]$ is the membrane decay factor calculated as $\alpha = e^{-\delta t / \tau_m}$, where δt is the discrete time step resolution of the simulation and τ_m is the neuronal membrane decay time constant, typically tens of milliseconds. The network activity is driven by input spikes x_i^t . Input and recurrent weights are represented as W_{ji}^{in} and W_{ji}^{rec} respectively. At the output layer, the recurrent spikes are fed through readout weights W_{kj}^{out} into a single layer of leaky integrator units y_k with the decay factor $\kappa \in [0, 1]$. This continuous valued output unit is analogous to a motor function which generates coherent motor output patterns [163] of the type shown in Fig. 3.3.

Training goal is to find optimal network weights $\{W_{ji}^{\text{inp}}, W_{ji}^{\text{rec}}$ and $W_{kj}^{\text{out}}\}$, that maximize the task performance [7]. For an ideal neuromorphic hardware, the learning algorithm must (i) use spatio-temporally local signals (ii) be online and (iii) tested beyond the toy problems. As an example, FORCE algorithm [163, 164] performs well on motor tasks, but it violates the first requirement by requiring knowledge of all synaptic weights. BPTT with surrogate gradients [165, 166] has its own drawbacks due to the need to buffer intermediate neuron states and activations, violating the second requirement.

E-prop offers a local and online learning rule for single-layer RNNs [75] by factorizing the gradients into a sum of products between instantaneously available learning signals and local eligibility traces. Specially, the gradient $\frac{dE}{dW_{ji}}$ is represented as a sum of products over time t :

$$\frac{dE}{dW_{ji}} = \sum_t \frac{dE}{dz_j^t} \cdot \left[\frac{dz_j^t}{dW_{ji}} \right]_{\text{local}}, \quad (3.2)$$

where E is the loss term such as the mean squared error between the network output y_k^t and target $y_k^{*,t}$ for regression tasks.

The term $\left[\frac{dz_j^t}{dW_{ji}} \right]_{\text{local}}$ is not an approximation. It is computed locally, carries the factorization of the gradient (a local measure of the synaptic weight's contribution to the neuronal activity) forward in time, and is described as *the eligibility trace* for the synapse from neuron i to neuron j at time t . Ideally, the term $\frac{dE}{dz_j^t}$ would be the total derivative of the loss function with respect to the neuron's spike output. However, this is unavailable online as it requires information about the spike's future impact on the error. Therefore, e-prop approximates the learning signal using the partial derivative $\frac{\partial E}{\partial z_j^t}$, considering only the direct influence of the spike output on

the instantaneous error. This approximation enables e-prop to function as an online learning algorithm for RSNNs, at the cost of truncating the exact gradients.

E-prop’s performance is notable, achieving performance comparable results to Long Short-Term Memory (LSTM) networks [167] trained with BPTT on complex temporal tasks. While the OSTL algorithm [84] also supports complex recurrent architectures and generates exact gradients, its computational complexity makes it less suitable for hardware implementation compared to e-prop.

In this work, we focus on e-prop due to its

- **Sufficient gradient alignment:** while not exact, e-prop provides a sufficient approximation of the true gradient.
- **Relative simplicity:** computational locality and simplicity are well-suited for low-power neuromorphic hardware applications.
- **Neuroscientific relevance:** the employment of eligibility traces aligns with neuroscientific observations of synaptic plasticity.

3.1.3.2 Memristor-Aware Weight Update Optimization

In mixed-signal neuromorphic processors, Learning Blocks (LBs) are typically located with neuron circuits [143, 168, 169]. LBs continuously monitor signals available to the neuron (e.g., presynaptic activities, inference, feedback) and, based on the desired learning rule, instruct weight updates on the synapses. However, when network weights are implemented with memristive devices, weight updates are subject to analog non-idealities. Therefore, LB design must consider these device non-idealities, such as programming noise and asymmetric SET/RESET updates, to ensure accurate transfer of calculated gradients to device conductances. To save both energy and area, weight updates are typically implemented in a single-shot fashion, using one or multiple gradual SET pulses to update the device without requiring a read-verify cycle.

In the following, we describe four widely adopted weight update methods for LBs, implemented in our PCM crossbar array simulation framework. Each method is designed to cope with device non-idealities. In all experiments, our framework employs differential synaptic configuration [81, 109, 110], where each synapse has two sets of memristors (G^+ and G^-) whose difference represents the effective synaptic conductance (Fig. 3.1a)²

THE SIGN GRADIENT DESCENT (SIGNGD) In SignGD, synaptic weights W is updated based solely on the sign of the loss function gradient with respect to the weights, $\hat{\nabla}_W \mathcal{L}$, as approximated by the online learning rule. Updates only occur when the magnitude of the gradient for a weight exceeds a predefined threshold θ such that

$$\Delta W = -\delta \text{sign}(\hat{\nabla}_W \mathcal{L}) \odot \mathbb{I}(|\hat{\nabla}_W \mathcal{L}| > \theta) \quad (3.3)$$

where δ is a positive stochastic variable representing the conductance change due to a single SET pulse applied to the memristor, $\text{sign}(\cdot)$ is the element-wise sign function, \odot is Hadamard product, $\mathbb{I}(\cdot)$ is the indicator function implementing stop-learning regime (1 if true, 0 otherwise).

This approach ensures convergence under certain conditions [171]. Due to its simplicity, SignGD is popular in memristive neuromorphic systems [172–174]. Upon weight update onset, LB applies a single SET pulse to either the G^+ or the G^- PCM device, as determined by the gradient’s sign. The effective value of δ is not constant due to WRITE noise and can lead to biases in the weight update distribution, potentially impacting learning dynamics and convergence.

² In differential configuration, unidirectional updates can saturate one or both devices [81, 109, 110]. While push-pull mechanism [170] can address this issue in memristors with symmetric SET/RESET characteristics, it’s not feasible in PCMs since the abrupt nature of RESET operations [46]. This necessitates a frequent saturation check and refresh mechanism to reset and reprogram both memristors.

STOCHASTIC UPDATE (SU) Conventional optimization methods often require weight updates that are 3-4 orders of magnitude smaller than the original weight values [175], posing a challenge for PCM devices with limited precision [176]. To bridge this precision gap, SU stochastically executes updates based on the approximated gradient’s magnitude [81]:

$$P(\text{update}) = \min\left(1, \frac{|\hat{\nabla}_W \mathcal{L}|}{p}\right) \quad (3.4)$$

where p is a scaling factor controlling the update probability. Choosing p such that update probability $P(\text{update})$ is proportional to $\|\hat{\nabla}_W \mathcal{L}\|$ ensures that larger gradients are more likely to trigger updates, effectively adapting the learning rate to the limited precision of PCM devices.

In our implementation, we scale the gradient by $1/p$ before comparing it to a random uniform value to determine whether an update occurs. This approach, inspired by Nandakumar *et al.* [81], allows for fine-grained control over the effective learning rate. Unlike the original work, we perform the refresh operation before the update to prevent updates on saturated devices. This modification further enhances the stability and reliability of the learning process.

MULTI-MEMRISTOR UPDATE (MMU) MMU enhances synaptic weight resolution and mitigates write noise by utilizing $2N$ PCM devices per synapse, arranged in N differential pairs [109]. Updates are applied sequentially to these devices, effectively reducing the minimum achievable weight change by a factor of $2N$ and the variance due to write noise by a factor of $\sqrt{2N}$ (see Supplementary Note 3).

In our implementation, we estimate the number of SET pulses required to achieve the desired conductance change, assuming a linear conductance increase of $0.75 \mu\text{S}$ per pulse (see Section 3.1.3).³ These pulses are then applied sequentially to the PCM devices in a circular queue. A refresh operation is performed if the conductance of any device pair exceeds $9 \mu\text{S}$ and their difference is less than $4.5 \mu\text{S}$. This refresh mechanism helps maintain the dynamic range of the synaptic weights and ensures reliable long-term operation.

MIXED-PRECISION UPDATE (MPU) MPU addresses the discrepancy between the high precision of learning algorithms and the limited resolution of PCM devices by accumulating gradients on a high-precision co-processor until they reach a threshold that can be reliably represented in PCM. This approach is analogous to quantization-aware training techniques [110, 111].

In our implementation, approximated gradients calculated by e-prop are accumulated in FP32 memory until they are an integer multiple of the PCM update granularity ($0.75\mu\text{S}$). These accumulated values are then converted to the corresponding number of pulses and applied to the PCM devices. A refresh operation is triggered when the conductance of either device in a pair exceeds $9\mu\text{S}$, and their difference is less than $4.5\mu\text{S}$, maintaining synaptic efficacy and preventing saturation.

3.1.3.3 Training a Spiking RNN on a PCM Crossbar Simulation Framework

We used PCM crossbar array model to determine realistic values for the network parameters $\{W_{ji}^{\text{in}}, W_{ji}^{\text{rec}}$ and $W_{kj}^{\text{out}}\}$. To represent synaptic weights, $W \in [-1, 1]$, with PCM device conductance values, $G \in [0.1, 12] \mu\text{S}$ [81], we used the linear relationship $W = \beta[\sum_N G^+ - \sum_N G^-]$, where $\sum_N G^+$ and $\sum_N G^-$ are the total conductance of N memristors⁴ representing the potentiation and the depression of the synapse respectively [81].

The forward computation (inference) of Eq. 3.1 is simulated using the PCM crossbar simulation framework, incorporating the effects of READ noise and temporal conductance drift. Subsequently, the weight updates calculated by the e-prop algorithm are applied to the PCM-based crossbar arrays using each of the methods described in Section 3.1.3.2.

³ For a more precise pulse estimation method, refer to Nandakumar *et al.* [81].

⁴ $N = 1$ for all weight update methods, except multi-memristor updates.

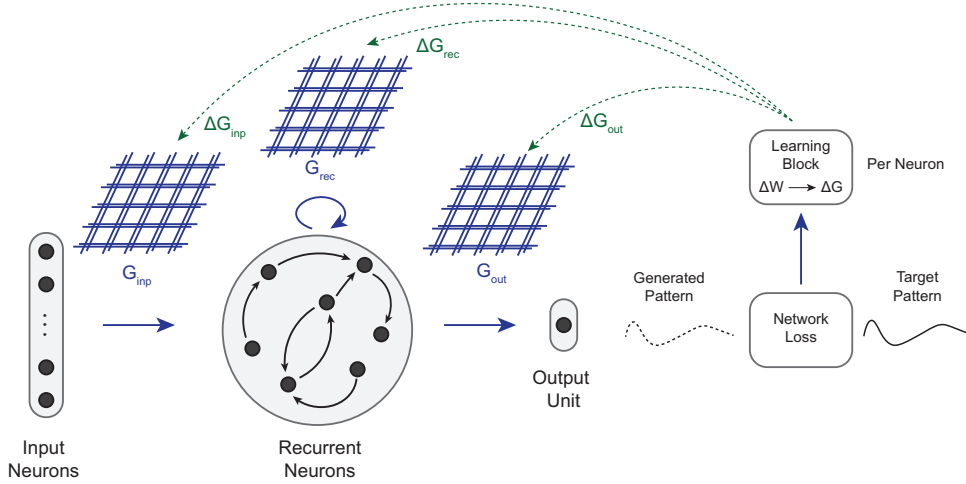


FIGURE 3.3: Overview of the spiking RNN training framework with the proposed PCM crossbar array simulation framework, illustrated for a pattern generation task. Network weights are allocated from three crossbar array models, G_{inp} , G_{rec} , G_{out} . The network-generated pattern is compared to the target pattern to produce a learning signal, which is fed back to each neuron. The LB calculates instantaneous weight changes ΔW using the e-prop learning rule and has to efficiently transfer the desired weight change to a conductance change, i.e. $\Delta W \rightarrow \Delta G$, while accounting for PCM non-idealities.

Method	Sign-gradient	Stochastic	Multi-mem (N=4)	Multi-mem (N=8)	Mixed-precision
MSE Loss	0.2080	0.1808	0.1875	0.1645	0.0380

TABLE 3.1: Performance evaluation of spiking RNNs with models of PCM crossbar arrays.

3.1.3.4 Results

We validated online training on a 1D continual pattern generation task [75], relevant for motor control and value function estimation in RL [163], using our analog crossbar framework (see Section 3.1.3.5)

Table 3.1 summarizes the training performance of the RSNN using different weight update methods on PCM crossbar arrays. We defined an MSE loss of <0.1 as the performance threshold for this task (see Section A for selection criteria). Among the five configurations, only the mixed-precision approach achieved this threshold, demonstrating sparse spiking activity and successful pattern generation.

During training, the weight saturation problem due to the differential configuration is rare ($< 1\%$), as shown in Fig 3.5 (right). We hypothesize that this is due to the mixed-precision algorithm reducing the total number of WRITE pulses through update accumulation (~ 12 WRITE pulses are applied per epoch, Fig. 3.6.). Fig. 3.5 (left) illustrates the effective weight distribution of the PCM synapses at the end of the training.

To assess performance loss due to PCM non-idealities (WRITE/READ noise, drift), we simulated an ideal 4-bit device model, effectively acting as a digital 4-bit memory (Section A).

Table 3.2 summarizes the performance of different update methods with this ideal model. Stochastic, multi-memristor ($N = 8$), and mixed-precision updates successfully solved the task, with mixed-precision achieving the best accuracy. All methods performed better without PCM non-idealities. Interestingly, stochastic updates outperformed both multi-memristor methods, suggesting the importance of few stochastic updates when training with quantized weights.

To further evaluate the impact of limited bit precision, we trained the same network with e-prop using standard FP32 weights. This high-resolution training yielded comparable results to mixed-precision training with either ideal quantized memory or the PCM cell model.

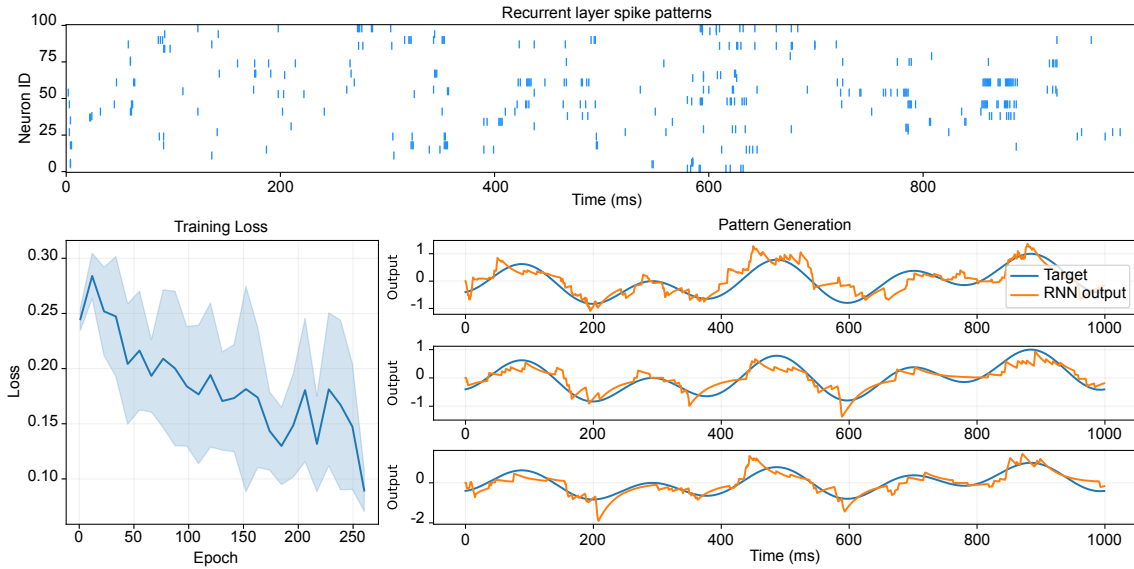


FIGURE 3.4: Dynamics of a network trained with the mixed-precision algorithm. The raster plot (top) shows the sparse spiking activity (~ 3.3 Hz) of recurrent-layer neurons. The training loss (bottom left) demonstrates MSE loss over 250 epochs is averaged over ten best network hyperparameters (see Fig A.8 for the best performing hyperparameter). Properly-tuned neuronal time constants and trained network weights result in generated patterns following the targets (bottom right). The generated patterns are extracted from three different spiking RNNs.

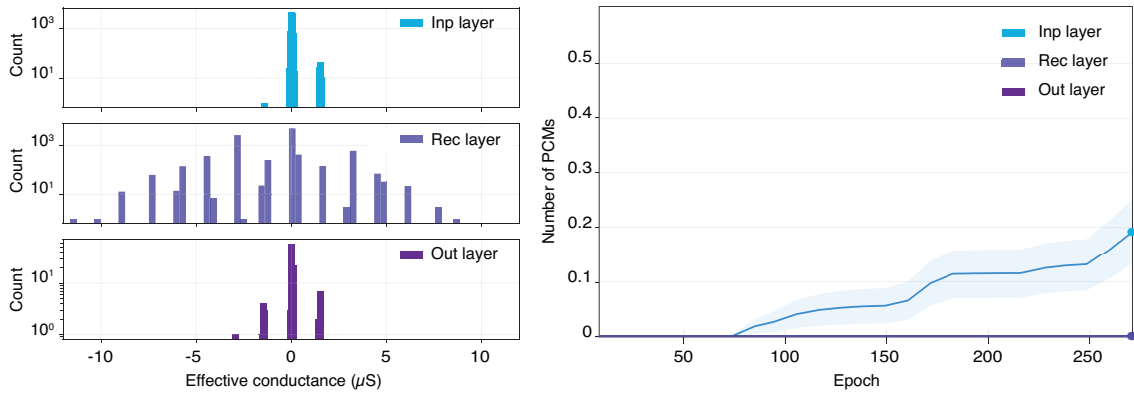


FIGURE 3.5: (left) The effective conductance distributions ($G^+ - G^-$) of the synapses in the input, recurrent and output layer, at the end of the training with the mixed-precision method. (right) Averaged over 50 training runs, the mean number of PCM devices requiring a refresh is shown for each layer. The refresh operation was not needed for recurrent and output layers.

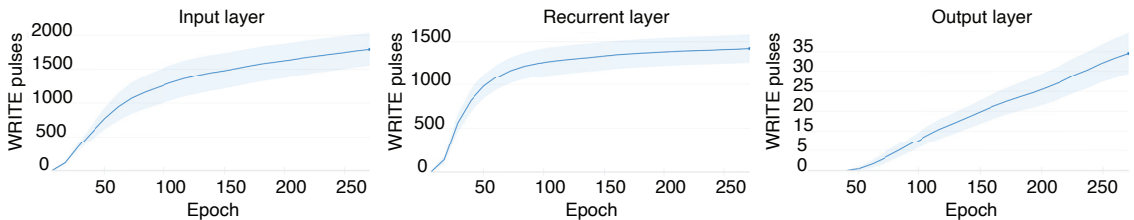


FIGURE 3.6: Total number of WRITE pulses applied to PCM devices are shown for the input, recurrent and output layers. Only 0.07%, 0.07% and 0.1% of PCM devices within each layer are programmed respectively during mixed-precision training.

Method	Sign-gradient	Stochastic	Multi-mem (N=4)	Multi-mem (N=8)	Mixed-precision
MSE Loss	0.1021	0.0758	0.1248	0.0850	0.0289

TABLE 3.2: Performance evaluation of spiking RNNs with an ideal crossbar array model⁵

Similar to Nandakumar *et al.* [81], we found that the probability scaling factor p in the stochastic update method allows tuning the number of devices programmed during training. Figure 3.7 shows that increasing p (decreasing update probability) can reduce WRITE pulses by up to an order of magnitude without degrading the loss. This result highlights the potential for optimizing energy efficiency in memristive online learning systems by strategically adjusting the update probability.

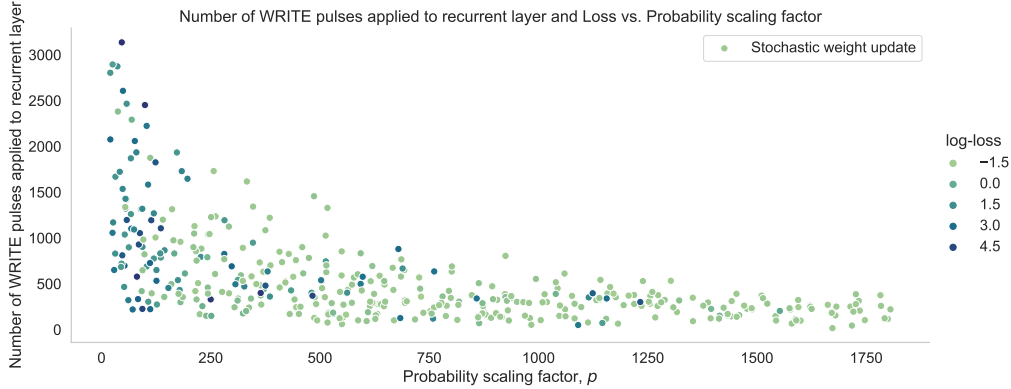


FIGURE 3.7: The stochastic update method enables tuning the number of WRITE pulses to be applied to PCM devices.

3.1.3.5 Methods

For the chosen pattern generation task, the network consists of 100 input and 100 recurrent LIF neurons, along with one leaky-integrator output unit. The network receives a fixed-rate Poisson input, and the target pattern is a one-second-long sequence defined as the sum of four sinusoids (1 Hz, 2 Hz, 3 Hz and 5 Hz), with phases and amplitudes are randomly sampled from uniform distributions $[0, 2\pi]$ and $[0.5, 2]$, respectively. Throughout the training, all layer weights $\{W_{ji}^{\text{in}}, W_{ji}^{\text{rec}}$ and $W_{kj}^{\text{out}}\}$, are kept plastic and the device conductances are clipped between 0.1 and 12 μS . This benchmark is adapted from [82].

We trained approximately 1000 different spiking RNNs for each weight update methods described in Section 3.1.3.2. Each network shared the same architecture, except for synapse implementations, some hyperparameters and weight initialization. As each update method requires specific additional hyperparameters and can significantly affect network dynamics, we tuned these hyperparameters for each method using Bayesian optimization [177]. We selected the best performing network hyperparameters out of 1000 candidates based on performance over 250 epochs of the pattern generation task.

3.1.4 Discussion

On-chip learning capability for RSNNS chips enables ultra-low-power intelligent edge devices with adaptation capabilities [178, 179]. This work focused on evaluating the efficacy of non-von Neumann analog computing with non-volatile emerging memory technologies in implementing

⁵ Multi-memristor configurations are implemented assuming a 4-bit resolution per memory cell. Hence $N = 4$ and $N = 8$ is equal to having 7-bit and 8-bit resolutions digital weights per synapse, respectively.

updates calculated by the spatio-temporally local e-prop learning rule. This task is particularly challenging due to the need to preserve task-relevant information in the network's activation dynamics for extended periods, despite analog weight non-idealities and the truncated gradients inherent to e-prop.

We developed a PyTorch-based PCM crossbar array simulation framework to evaluate four simplistic memristor update mechanisms. Through extensive hyperparameter optimization, we demonstrated that the mixed-precision update scheme yielded the best accuracy. This superior performance stems from the accumulation of instantaneous gradients on high-precision memory, enabling the use of a low learning rate. Consequently, the ideal weight update magnitude aligns closely with the minimum programmable PCM conductance change, leading to improved convergence.

However, the mixed-precision scheme necessitates high-precision memory for gradient accumulation. This could potentially be addressed by incorporating a co-processor alongside the memristor crossbar array, as demonstrated previously [110]. Despite this requirement, gradient accumulation enables training with high learning rates, reduces the number of programming cycles together with the total energy to train. The synergy between memristor-based synapses and learning rules and neural architectures inherently capable of gradient accumulation is a promising avenue for further research.

Memory resolution is a critical factor influencing learning performance, aligning with previous findings on mixed-precision learning [110]. However, increasing resolution often comes at the cost of larger synapses due to the increased number of devices. An alternative solution is to employ binary synapses with a stochastic rounding update scheme [180]. This approach can leverage the intrinsic cycle-to-cycle variability of memristive devices [143] to implement stochastic updates efficiently, effectively reducing the learning rate and guiding weight parameters towards their optimal binary values [181, 182]

From the computational neuroscience perspective, mixed-precision hardware resembles the concept of the cascade memory model in the neuroscience, where complex synapses hold a hidden state variable which only becomes visible after hitting a threshold [183]. Similar meta-plastic models has also recently been used for catastrophic forgetting [184].

To the best of our knowledge, this is the first report on the online training of RSNNs with e-prop learning rule based on realistic PCM synapse models. Our simulation framework enables benchmarking of common update circuits designed to cope with memristor non-idealities and demonstrates that accumulating gradients enhances PCM device programming reliability, reduces the number of programmed devices and outperforms other synaptic weight-update mechanisms.

In the following Section 3.2, we will present the implementation of the mixed-precision update scheme on a neuromorphic hardware with PCM devices. Later in Section 3.3, I will introduce how eligibility traces, a crucial building block of many local learning rules, can be implemented with volatile memristive devices.

3.2 IMPLEMENTING ONLINE TRAINING OF RSNNs ON A NEUROMORPHIC HARDWARE

Building upon the simulation results in the Section 3.1, we now present an implementation of e-prop on a neuromorphic hardware with in-memory computing capabilities. We embed all the network weights directly onto physical PCM devices and control the training procedure with a hardware-in-the-loop setup. We utilize the HERMES chip [185] fabricated in 14nm CMOS technology with 256x256 PCM crossbar arrays to validate the feasibility of on-chip learning under physical device constraints. Our experiments demonstrate that the mixed-precision training approach remains effective, achieving performance competitive with an FP32 realization while simultaneously equipping the RSNN with online training capabilities and leveraging the ultra-low-power benefits of the hardware.

3.2.1 From the simulation to an analog chip

The HERMES chip features two in-memory computing cores comprising PCM devices [23], with conductances (G) controlled by individual SET and RESET pulses. A low-amplitude SET pulse ($100 \mu\text{A}$, 600ns) gradually switches the material from amorphous to crystalline phase, while a high-amplitude RESET pulse ($700 \mu\text{A}$, 600 ns) rapidly switches it to HRS.

The crossbar array operates in a differential parallel setup, i.e., each element of the embedded weight matrices W is represented by four PCM devices in the following way: $W_{ij} = ((G_A^+ + G_B^+) - (G_A^- + G_B^-))/2$, indicated with the 8T4R quantifier in the system diagram of Fig. 3.8. The in-memory computing core allows feeding inputs, e.g., $\{x^t, z^{t-1}, z^t\}$, to the rows and through the application of Ohm's and Kirchhoff's law, it performs a fully parallel matrix-vector multiplication [23], approximately with a 4-bit precision [186].

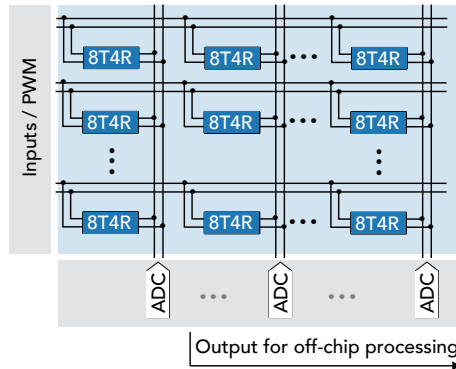


FIGURE 3.8: Illustration of the working principle of phase-change devices and their integration into a crossbar architecture. **a**, Phase switching behavior of PCM devices. SET and RESET pulses can be used to transition between the amorphous and the crystalline phase. **b**, The PCM devices from **a** can be incorporated into a crossbar array structure. In our work, four PCM devices are used in a differential manner to represent each weight element

Similar to Section 3.1, we tested the network on a 1D continual pattern regression task, using an RSNN architecture with 100 recurrently connected LIF neurons and one leaky-integrator output unit (Eq. 3.1) Again, the RSNN is driven by fixed-rate Poisson spikes from 100 input neurons, with a membrane decay time constant of 30 ms for both recurrent and output units.

To optimize resources allocation, we strategically embedded trainable parameters W_{in} , W_{rec} and W_{out} , within Core 1, and the feedback matrix B_{out} within Core 2. This architectural design, illustrated in Fig. 3.9, enables network inference on one core and error-based learning signal generation on the other. We use e-prop for computing the approximated gradients for network weights and leverage the mixed-precision algorithm to accumulate gradients in a high-precision unit. This unit also serves to store the dataset, to compute neuron activations and eligibility traces, and to calculate network error.

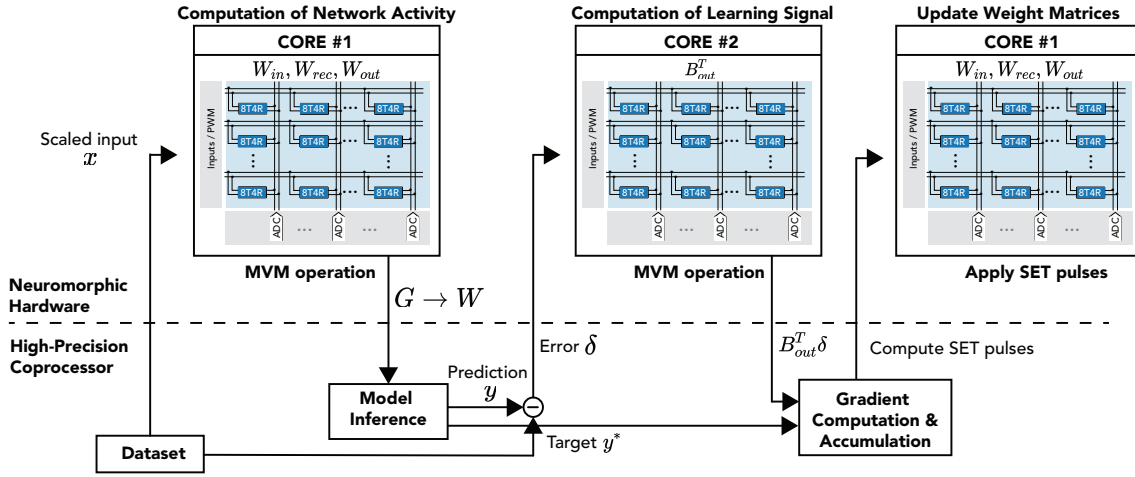


FIGURE 3.9: Task illustration and realization of the network on neuromorphic hardware. Realization of the regression task on a neuromorphic hardware using two cores with PCM crossbar arrays. The trainable parameters W_{in} , W_{rec} and W_{out} are placed into Core 1 and B_{out} is placed into Core 2. The neuromorphic is used to perform the matrix-vector multiplication required to compute the network activity and the learning signal. A high-precision unit is used to track the individual gradients which are applied to the trainable parameters.

Before transitioning to the hardware testing, a comprehensive investigation of network performance was conducted within a simulation framework, subjecting the network to various hardware constraints. This involved utilizing weights with varying precision levels, including 32-bit floating point (SW 32bit), 8-bit and 4-bit fixed-point (SW 8bit and SW 4bit), and weights based on a PCM model (SW PCM), as depicted in Fig. 3.2.

The results, illustrated in Figure 3.10, were obtained using four distinct random seeds. Notably, the performance metrics using 32-bit and 8-bit precision were comparable, affirming the robustness of the network under reduced precision. The network's performance remained resilient even with 4-bit ($E = 3.93 \pm 0.58$) or simulated PCM ($E = 3.72 \pm 0.53$). Although a slight degradation was observed with hardware ($E = 5.59 \pm 1.29$), the network succeeded in reproducing the target pattern (Fig. 3.10b). The individual subpanels within this figure effectively visualize the patterns at different stages of training: the beginning, after 30 iterations, and at the end of training.

The histograms in Fig. 3.10c show the distributions of trainable matrices before and after training. Notably, modifications in the output weights were instrumental in achieving accurate pattern generation. The average firing rate was maintained at approximately 10 Hz through regularization. This ensured sparsity in both communication and programming pulses, crucial for energy efficiency and extending device longevity. The sparse application of SET pulses, evident in Figure 3.10d, further underscores this efficiency. Specifically, only 2-3 pulses per iteration were required for the output weight matrix, even though it comprised 100 elements. This highlights the effectiveness of the gradient accumulation in reducing the number of programming pulses and, consequently, the overall energy consumption.

3.2.2 Discussion

We have demonstrated that training RSNNs with the e-prop local weight update rule, using a hardware-in-the-loop approach, can be robust to both limited computational precision and analog imperfections inherent to memristive devices. Furthermore, our experiments show that this system achieves performance competitive with conventional software implementations with full-precision. The RSNN neurons exhibited a low firing rate, and mixed-precision training significantly reduced the number of PCM programming pulses. This reduction in programming activity not only enhances energy efficiency but also mitigates potential endurance issues associated with frequent

device switching. Our findings enable RSNNs trained with biologically-inspired algorithms to be deployed on memristive neuromorphic hardware for sparse and online learning.

In the following Section 3.3, we will present how eligibility traces can be implemented with volatile memristive devices, enabling more scalable credit assignment on neuromorphic hardware.

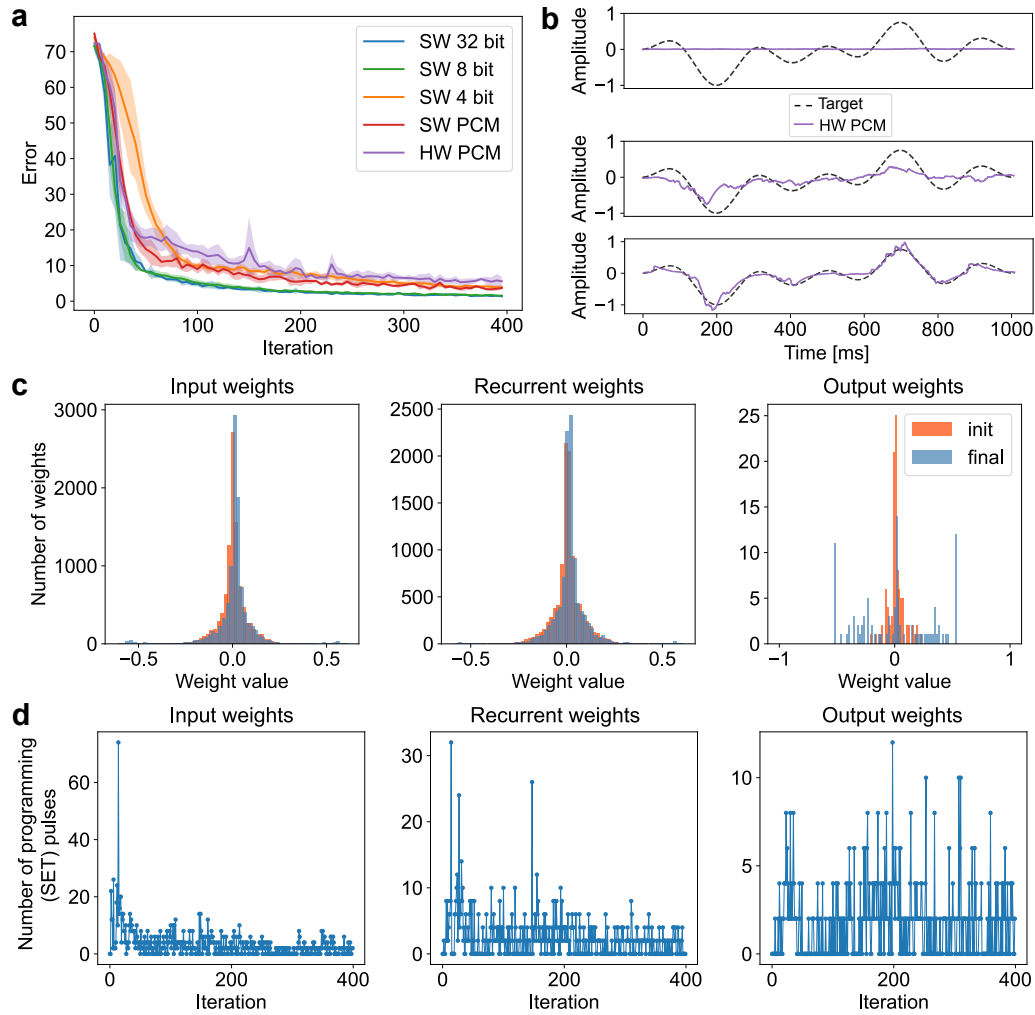


FIGURE 3.10: **Results of our training approach realized with different synapse models.** **a**, Evolution of the squared error using different synapse models, averaged over 4 random initializations. **b**, Visual comparison of the network output and the target pattern, at the beginning of training (first subpanel), after 30 training iterations (second subpanel) and after training (third subpanel). **c**, Histogram of the trainable weight matrices before and after training. **d**, Number of SET pulses applied to the individual weight matrices.

3.3 SCALABLE SYNAPTIC ELIGIBILITY TRACES WITH VOLATILE MEMRISTIVE DEVICES

Dedicated hardware implementations of spiking neural networks that combine the advantages of mixed-signal neuromorphic circuits with those of emerging memory technologies have the potential of enabling ultra-low power pervasive sensory processing. To endow these systems with additional flexibility and the ability to learn to solve specific tasks, it is important to develop appropriate on-chip learning mechanisms. Recently, a new class of *three-factor* spike-based learning rules have been proposed that can solve the temporal credit assignment problem and approximate the error back-propagation algorithm on complex tasks. However, the efficient implementation of these rules on hybrid CMOS/memristive architectures is still an open challenge. Here we present a new neuromorphic building block, called PCM-trace, which exploits the drift behavior of phase-change materials to implement long-lasting eligibility traces, a critical ingredient of three-factor learning rules. We demonstrate how the proposed approach improves the area efficiency by $> 10\times$ compared to existing solutions and demonstrates a technologically plausible learning algorithm supported by experimental data from device measurements.

3.3.1 Introduction

Neuromorphic engineering uses electronic analog circuit elements to implement compact and energy-efficient intelligent cognitive systems [187–190]. Leveraging substrate’s physics to emulate biophysical dynamics is a strong incentive toward ultra-low power and real-time implementations of neural networks using mixed-signal memristive event-based neuromorphic circuits [144, 191–193]. The majority of these systems are currently deployed in edge-computing applications only in *inference mode*, in which the network parameters are fixed. However, learning in edge computing can have many advantages, as it enables adaptation to changing input statistics, sensory degradations, reduced network congestion, and increased privacy. Indeed, there have been multiple efforts implementing Spike-Timing Dependent Plasticity (STDP)-variants and Hebbian learning using neuromorphic processors [168, 181, 194]. These methods control Long-Term Depression (LTD) or Long-Term Potentiation (LTP) by specific local features of pre- and post-synaptic activities. However, local learning rules themselves do not provide any guarantee that network performance will improve in multi-layer or recurrent networks. Local error-driven approaches, e.g., the Delta Rule, aim to solve this problem but fail to assign credit for neurons that are multiple synapses away from the network output [195, 196]. On the other hand, it has been recently shown that by using external *third-factor* neuromodulatory signals (e.g., reward or prediction error in reinforcement learning, teaching signal in supervised learning), this can be achieved in hierarchical networks [197, 198]. However, there needs to be a mechanism for synapses to remember their past activities for long periods of time, until the reward event or teacher signal is presented. In the brain, these signals are believed to be implemented by calcium ions, or CAMKII enzymes in the synaptic spine [199] and are called eligibility traces. In machine learning, algorithmic top-down analysis of the gradient descent demonstrated how local eligibility traces at synapses allow networks to reach performances comparable to error back-propagation algorithm on complex tasks [75, 85, 200].

There are already neuromorphic platforms that support the synaptic eligibility trace implementation such as Loihi [89], BrainScales [90] or SpiNNaker [91]. The learning (weight update) in these platforms is only supported through the use of digital processors, hence the numerical trace calculation leads to extremely memory intensive operations forming a von Neumann bottleneck [92, 93]. Especially when the eligibility trace calculation is per synapse (instead of per neuron) the memory overhead quickly becomes overwhelming as the number of traces scales quadratically with the number of neurons in the network. And unlike the convolutional architectures on digital neuromorphic processors, where weight sharing reduces the memory bandwidth, the eligibility traces cannot be shared due to their activity dependent nature.

On the other hand, mixed-signal neuromorphic processors that perform in-memory computation can emulate the desired neural and synaptic dynamics using the physics of the analog substrate [201, 202]. Differential-Pair Integrator (DPI) based circuits [202, 203] which rely on

Learning rule	Pre-synaptic terms	Post-synaptic terms
e-prop (LIF) [82]	x_j	-
e-prop (ALIF) [82]	x_j	ψ_i
Sparse RTRL [83]	x_j	-
BDSP [39]	x_j	-
SuperSpike [85]	$\epsilon * x_j$	ψ_i
Sparse Spiking G.D. [86]	x_j	-

TABLE 3.3: Eligibility Traces in Gradient-Estimating Learning Rules

accumulating volatile information on capacitors, in principle can be used to implement eligibility traces. Recently, a substantial progress has been made [94] in implementing slow-dynamics DPI synapse circuits using advanced Fully Depleted Silicon-On-Insulator (FDSOI) technologies. By combining reverse body biasing and self-cascoding techniques [204], these circuits can achieve ~ 6 s long synaptic traces [94]. However, resulting area due to large capacitor sizes and area-dependent leakage due to Alternate Polarity Metal On Metal (APMOM) structures hinder the *scalability* of such hardware implementations.

In this work, we present a novel approach to exploit the drift behavior of PCM devices to intrinsically perform eligibility trace computation over behavioral timescales. We present the *PCM-trace* building block as a hybrid memristive-CMOS circuit solution that can lead to record-low area requirements per synapse. To the best of our knowledge, this is the first work that uses a memristive device not only to store the weight of synapses, but also to keep track of synaptic eligibility to interact with a third factor toward scalable next-generation on-chip learning.

Eligibility traces in machine learning and neuroscience

Eligibility trace is a decaying synaptic state variable that tracks recency and frequency of synaptic events, as described in Eq. (3.5). The trace state, e_{ij} , of the synapse between pre-synaptic neuron j and post-synaptic neuron i is controlled by usually a linear function of pre-synaptic spiking activity $f_j(x_j)$ and non-linear function of the post-synaptic activity $g_i(x_i)$, such that

$$\frac{de_{ij}}{dt} = -\tau_e e_{ij} + \eta f_j(x_j) g_i(x_i) \quad (3.5)$$

, where τ_e is the time-constant of the trace and η is the constant scaling factor [197].

The function of eligibility trace is to keep the temporal correlation history of $f_j(x_j)$ and $g_i(x_i)$ available in the synapse, by accumulating instantaneous correlation events, called *synaptic tags*. From the top-down gradient-based machine learning perspective, various learning rules require eligibility trace functionality as a part of the network architecture and specifies their own synaptic tag requirements, $f_j \cdot g_i$, (i.e., what information to accumulate on the synapse).

Table 3.3 summarizes some of the recently developed biologically-plausible, local learning rules employing eligibility traces within the supervised learning framework. Most of the listed learning rules accumulate pre-synaptic events, x_j , seldom further smoothed with ϵ (causal membrane kernel), whereas some learning rules additionally require the information of a surrogate partial derivative function of post-synaptic state, ψ_i . By approximating the gradient-based optimization for spiking neural networks, these learning rules support competitive performance on standard audio and image classification datasets such as TIMIT Dataset [205], Spiking Heidelberg Digits [206], Fashion-MNIST [207], Neuromorphic-MNIST [208], CIFAR-10 [209] and even ImageNet [210].

In the RL, the advantages of having long-lasting synaptic eligibility traces are more evident. Eligibility traces carry the temporal *synaptic tag* information into the future, allowing *backward view* when the sparse reward arrives from the environment [211]. By doing so, eligibility traces assist solving the distal reward problem [88] (how the brain assigns credits/blame for neurons if

the activity patterns responsible for the reward are no longer exist when the reward arrives) by bridging the milli-second neuronal timescales and second-long behavioral timescales. Almost any Temporal Difference (TD) method e.g., Q-learning or SARSA can benefit from eligibility traces to learn more efficiently [211]. The policy gradient methods utilizing the temporal discounting operation e.g., discounted reward [211] or discounted advantage [212], naturally demands the synaptic eligibility traces. Moreover, some on-policy and off-policy RL models can explain behavioral and physiological experiments on multiple sensory modalities, only if they are equipped with synaptic eligibility traces with >10 s decay time [213].

Eligibility traces are also deeply rooted in neurobiology. The synaptic machinery that implements the eligibility trace might be calcium-based mechanisms in the spine e.g., CamKII [214, 215], or metastable transient state of molecular dynamics inside the synapse [216]. In the visual and frontal cortex, *in-vivo* STDP experiments suggest that pre-before-post pairings induces a *synaptic tagging* that decays over ~ 10 s and result in LTP with the arrival of the third-factor neuromodulator noradrenaline [217]. In the hippocampus, Brzosko, Schultz & Paulsen [218] found that post-before-pre pairings can result in LTP if the third-factor neuromodulator dopamine arrives in the range of minutes.

In summary, both top-down approaches following machine learning principles and bottom-up approaches built upon *in-vivo* and *in-vitro* synaptic plasticity experiments imply the importance of having eligibility traces in neural architectures.

3.3.2 PCM-trace: Implementing eligibility traces with PCM drift

3.3.2.1 PCM Measurements

Temporal evolution of electrical resistivity is a widely-observed phenomenon in PCM due to the rearrangements of atoms in the amorphous phase [219]. This behavior is commonly referred to as structural relaxation or drift. To start the drift, a strong RESET pulse is applied to induce a crystalline to amorphous phase transition where the PCM is melted and quenched. The low-ordered and highly-stressed amorphous state then evolves to a more energetically favorable glass state within tens of seconds [112].

At constant ambient temperature, the resistivity follows

$$R(t) = R(t_0) \left(\frac{t}{t_0} \right)^\nu, \quad (3.6)$$

where $R(t_0)$ is the resistance measured at time t_0 and ν is the drift coefficient. It has been experimentally verified by many groups that Eq. (3.6) can successfully capture the drift dynamics [112, 156, 220], from microseconds to hours range [221].

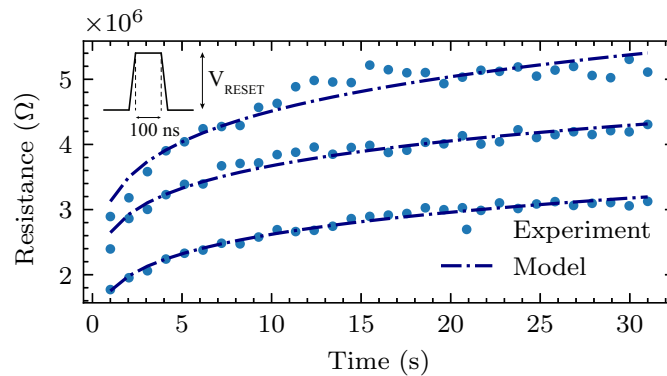


FIGURE 3.11: Experimental (dots), and simulated (dashed lines) resistance drift characteristics at constant room temperature.

With the collaboration of CEA-LETI, we integrated $\text{Ge}_2\text{Sb}_2\text{Te}_5$ -based PCM in state-of-the-art PCM heater-based devices fabricated in the Back-End-Of-Line (BEOL) based on 130 nm CMOS technology. The PCM thickness is 50 nm with the bottom size of 3600 nm^2 . Drift measurements

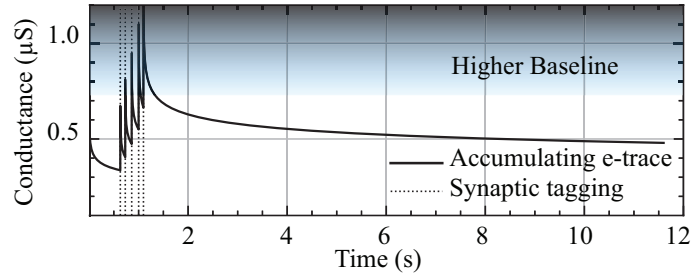


FIGURE 3.12: Accumulating eligibility trace using PCM-trace drift model (Eq. 3.7). After resetting the PCM-trace device at $t = 0$, 5 random synaptic tags are applied to the synapse, implemented by a gradual SET for each tag that results in 50% increase in the conductivity. The device can keep the eligibility trace for more than 10 s.

were performed on three devices to monitor the temporal evolution of the resistance in the HRS state, particularly confirming the model in Eq. (3.6). The test was conducted by first resetting all the cells by applying a RESET pulse to the heater, which has a width of 100 ns with 5 ns rising and falling times, and a peak voltage of 1.85 V. Then, an additional programming pulse is used to bring the devices to different initial conditions, corresponding to $R(t = 1 \text{ s}) = [1.77 \text{ M}\Omega, 2.39 \text{ M}\Omega, 2.89 \text{ M}\Omega]$. The low-field device resistances are measured every 1 s for 30 s by applying a READ pulse which has the same timing of the RESET pulse but a peak voltage of 0.05 V.

PCM-trace is a novel method to implement seconds-long eligibility trace for the synapse using the drift feature of PCM. By writing Eq. (3.6) as a difference equation of the conductance, we can show that the temporal evolution of the conductance has decay characteristics similar to Eq. (3.5) such that $G_{ij}^{t+\Delta t} = \left(\frac{t-t_p}{t-t_p+\Delta t}\right)^\nu G_{ij}^t$, where $G_{ij}^{t_0} = 1/R_{ij}^{t_0}$, and t_p is the last programming time as drift re-initializes with every gradual SET [81, 222]. The main difference is that the rate of change in PCM resistivity is a function of time; nevertheless, its time constant is comparable for behavioral time-scales as $\tau_{PCM} = -\Delta t / \log((t/(t+\Delta t))^\nu)$ is on the order of tens of seconds [213]. Therefore, the PCM-trace dynamics can emulate the eligibility trace of the synapse as follows:

$$G_{ij}^{t+\Delta t} = \left(\frac{t-t_p}{t-t_p+\Delta t}\right)^\nu G_{ij}^t + \eta f_j(x_j^t) g_i(x_i^t) \quad (3.7)$$

In the PCM-trace method (Eq. 3.7), the accumulating term on the eligibility trace is implemented by applying a gradual SET to the PCM device whenever the synapse is tagged. To maximize the number of accumulations a PCM device can handle without getting stuck in the LRS regime, some operational conditions need to be satisfied. We initialize the device to HRS by applying a strong RESET pulse, and wait for an initialization time t_{init} of at least 250 ms for the device resistance to increase. If t_{init} is too short, the device conductance would still be too high to be able to accumulate enough tags; and if it is too long, the decay will be weaker (see Eq. 3.6). Initialization time can be modulated to reach the desired drift speed depending on the material choice and the application. After the initialization time, whenever the synapse is tagged, a single gradual SET (with an amplitude of 100 μA and a pulse width of 100 ns with 5 ns rising and falling times) is applied. To make sure that the device stays in the HRS, a read-verify-set scheme can be used. Finally, the value of the eligibility trace can be measured after seconds by reading the conductance of the device (see Fig. 3.12).

3.3.3 Multi PCM-trace: Increasing the dynamic range of traces

The number of gradual SET pulses applied to a single PCM-trace device is limited, because each pulse partially increases the device conductivity and eventually move the device toward its LRS ($< 2 \text{ M}\Omega$), where the drift converges to a higher baseline level. This problem can be solved by storing the synaptic eligibility trace distributed across multiple PCM devices, as in Fig. 3.13.

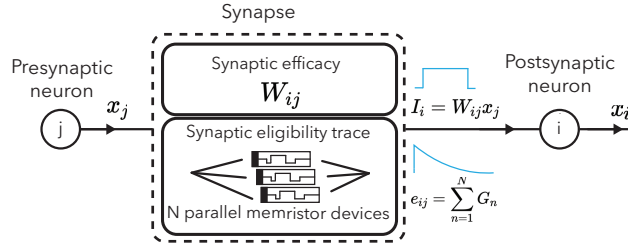


FIGURE 3.13: Multi PCM-trace concept. Each synapse has a weight and a PCM-trace block where multiple parallel PCM devices keep the eligibility trace of the synapse with their natural drift behavior.

By successively routing the tags to multiple PCM devices, the number of gradual SET pulses to be applied per single device is significantly reduced. The postsynaptic neuron receives the sum of product of the pre-synaptic activity and the weight block. In parallel, the PCM-trace block calculates the eligibility trace as a function of pre- and post-synaptic activities (Eq. 3.7), to be used in the weight update. Fig. 3.14 demonstrates the increase of effective dynamic range (number of updates to eligibility trace without getting stuck in the LRS) using multiple PCM devices.

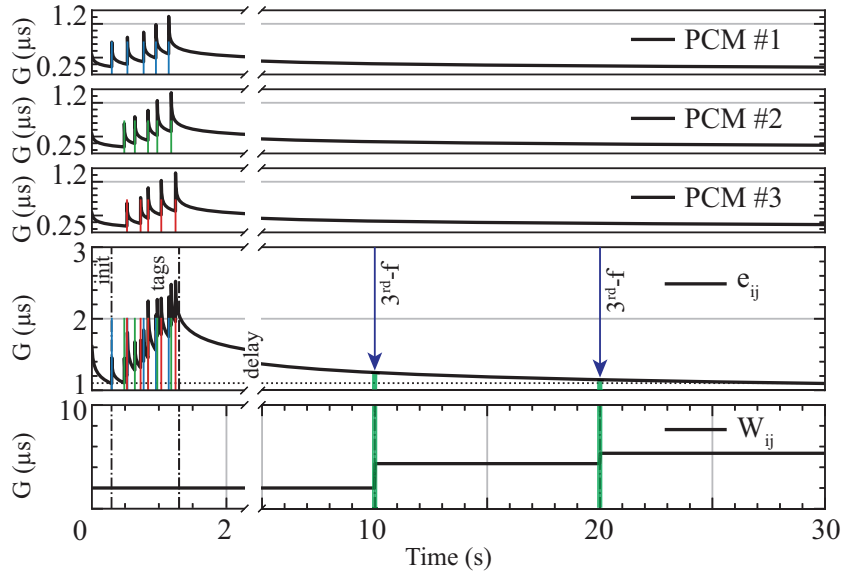


FIGURE 3.14: Accumulating eligibility trace using multi-PCM configuration. Synapse receives 15 tags between 300 ms to 1300 ms which are routed to three different devices shown in the top three plots. The effective eligibility trace is calculated by applying a READ pulse to the parallel PCM devices. The initialization duration and synaptic activity period are shown with dashed lines in the bottom plot. The synaptic efficacy W_{ij} is modified depending on the state of eligibility trace once the third-factor signal arrives.

3.3.4 Circuits and Architecture

3.3.4.1 PCM-trace Architecture

An example in-memory event-based neuromorphic architecture is shown in Fig. 3.15, where the PCM-trace is employed to enable three-factor learning on behavioral time scales.

Synapse: Each synapse includes a weight block W_{ij} in which two PCM devices are used in differential configuration to represent positive and negative weights [143]. The effective synaptic weight is calculated as the difference of these two conductance values, i.e., $W_{ij} = W_{ij}^+ - W_{ij}^-$. Also, each synapse has a PCM-trace block e_{ij} that keeps the eligibility trace. Inside the PCM-trace block, there are two PCM devices, keeping track of the positive and negative correlation between pre

and post-synaptic neurons. On the onset of the pre-synaptic input spike, PRE_j , (i) W_{ij} is read, and the current is integrated by the post-synaptic neuron i ; (ii) Based on the UP/DN signal from the learning block (LB), a gradual SET programming current is applied to positive/negative PCM-trace devices.

Neuron with Learning Block (LB): The LB estimates the pre-post synaptic neuron correlation using the Spike-Driven Synaptic Plasticity (SDSP) rule [223]. At the time of the pre-synaptic spike, the post-synaptic membrane variable is compared against a threshold, above (below) which an UP (DN) signal is generated representing the tag type. On the arrival of the third factor binary reward signal, REW , the state of the Eligibility Traces (ETs) devices is read by the V_{PROG} block (Fig. 3.16b) which generates a gate voltage that modulates the current that programs the weight devices W_{ij} (see Alg. 2).

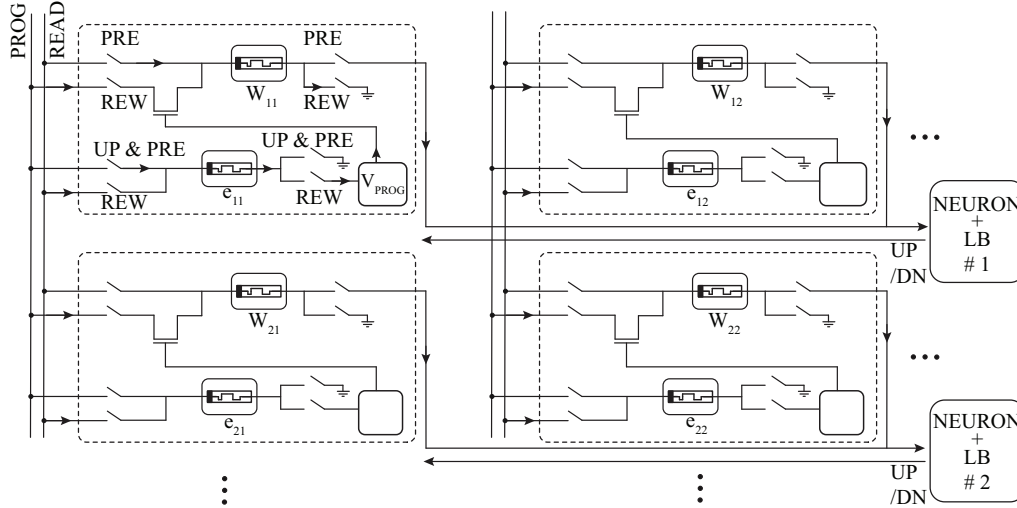


FIGURE 3.15: PCM-trace-based neuromorphic architecture for three-factor learning. Only positive eligibility trace (e_{ij}^+) and W_{ij}^+ are shown.

3.3.4.2 Circuit Simulation

Fig. 3.16 describes the block diagram of the LB implementing SDSP rule, which calculates the pre-post neurons' correlation. The membrane variable (described here as a current I_{mem} since circuits are in current-mode) is compared against a threshold value I_{th} through a Bump circuit [143, 224].

The output of this block is digitized through a current comparator (in our design chosen as a Winner-Take-All (WTA) block [225]) and generates UP/DN signals if the membrane variable is above/below the threshold I_{th} , and $STOP$, SP , if they are close within the dead zone of the bump circuit [224].

Fig. 3.16b presents the circuit schematic which reads the PCM-trace and generates V_{PROG} . To read the state of the device, a voltage divider is formed between the PCM device and a pseudo resistor, highlighted in green. As the device resistance changes, the input voltage to the differential pair, highlighted in red, changes. This change is amplified by the gain of the diff. pair and the device current is normalized to its tail current giving rise to I_{PROG}

which develops V_{PROG} through the diode-connected NMOS transistor. V_{PROG} is connected to the gate of the transistor in series with the weight PCM (see Fig. 3.15).

Fig. 3.17a plots PRE , I_{mem} , the output of the learning block at the time of the PRE , and the gradual

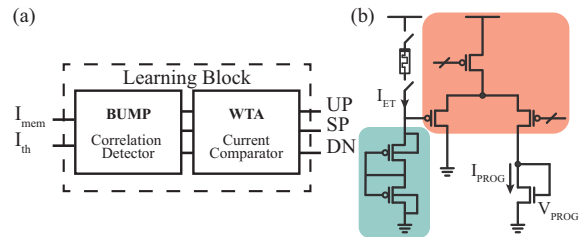


FIGURE 3.16: (a) Learning block diagram generating UP/DN signals as a function of the correlation between pre and post-synaptic activity. (b) V_{PROG} circuit reading from the eligibility trace device through the voltage divider (green) and generating I_{PROG} through the diff. pair (red) to program the weight device.

Algorithm 2: Three-factor learning with PCM-trace

```

 $W_{ij}^+ = \text{rand}(); W_{ij}^- = \text{rand}();$ 
 $\text{RESET}(e_{ij}^+); \text{RESET}(e_{ij}^-);$ 
while  $t < \text{taskDuration}$  do
   $I_{i,x} = 1 - (V_{i,th} - V_{i,mem}) / V_{i,th};$ 
  if @Pre and  $t > t_{init}$  then
    # Eligibility trace accumulation
    forall  $e_{ij}$  do
      if  $I_{i,x} > I_{th}^+$  then
         $\text{GRADUAL\_SET}(e_{ij}^+);$ 
      if  $I_{i,x} < I_{th}^-$  then
         $\text{GRADUAL\_SET}(e_{ij}^-);$ 
    # Third-factor
    if Reward then
      forall  $W_{ij}$  do
         $I_{ij,e^+}, I_{ij,e^-} = \text{READ}(e_{ij}^+, e_{ij}^-);$ 
         $I_{PROG}^+ = I_{ij,e^+} * \text{scale\_const};$ 
         $I_{PROG}^- = I_{ij,e^-} * \text{scale\_const};$ 
         $\text{GRADUAL\_SET}(W_{ij}^+, I_{PROG}^+);$ 
         $\text{GRADUAL\_SET}(W_{ij}^-, I_{PROG}^-);$ 

```

SET pulse applied to the device. As shown, the UP signal is asserted when the membrane current is higher than the threshold indicated in red, which causes a gradual SET pulse with $100 \mu\text{A}$ to be applied across the PCM-trace device upon PRE events. Fig 3.17b shows the generated I_{PROG} as a function of the state of the eligibility trace device. The higher the ET device's resistance, the less the accumulated correlation, thus the lower the programming current that should be applied to the weight device. The resistance on the x axis of the plot matches the measured resistance of PCM devices shown in Fig. 3.11.

3.3.5 Discussion

Long-lasting ETs enable the construction of powerful learning mechanisms for solving complex tasks by bridging the synaptic and behavioral time-scales. In this work, for the first time, we proposed to use the drift of PCM devices to implement ETs, and analyzed their feasibility for implementation in existing fabrication technologies.

The implementation of the three-factor learning rules with ETs per synapse requires complex memory structures for keeping track of the eligibility trace and the weight. Our proposed approach has clear advantages for scaling. Table 3.4 shows a comparison between our PCM synapse and a CMOS-only implementation in 22 nm FDSOI technology from [226].

PCM is among the most advanced emerging memory technology integrated into the neuro-morphic domain [109]. Our approach of using PCM to store both the synaptic weight and the eligibility trace requires no additional nano-fabrication methods.

	Area (μm^2)	τ (s)	Area/ τ ($\mu\text{m}^2 \text{s}^{-1}$)
CMOS [226]	20×17	6	56.6
PCM [This work]	12×12	> 30	< 4.8

TABLE 3.4: Area comparison of eligibility trace implementation

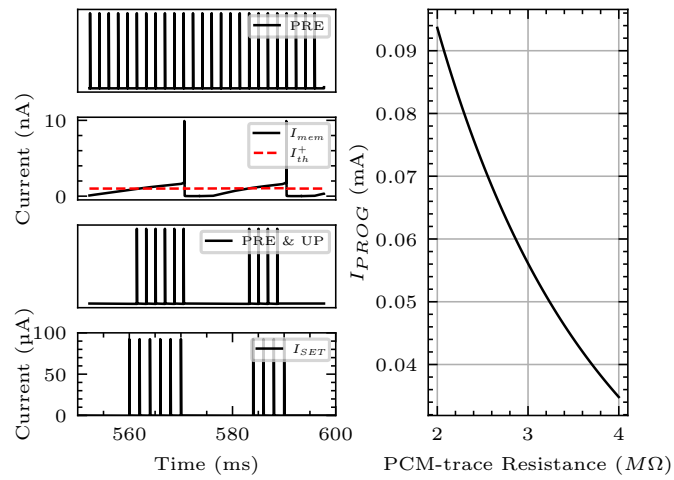


FIGURE 3.17: a) From the top: PRE events, POST membrane current (I_{mem}) and learning threshold (I_{th}), PRE events only when I_{mem} is higher than I_{th} , and corresponding gradual SET current pulse applied to PCM-trace. b) Programming current to be applied to the weight PCM as a function of eligibility trace state.

DISCOVERING SINGLE MATERIAL THAT SWITCHES BETWEEN VOLATILE OR NON-VOLATILE MODES

This chapter's content was published in Nature Communications, featured as one of 50 best papers recently published in the field and can be found online in an extended form including all experimental details which we omit here for clarity. The original publication is authored by Yigit Demiras, Rohit Abraham John*, Yevhen Shynkarenko, Yuliia Berezovska, Natacha Ohannessian, Melika Payvand, Peng Zeng, Maryna I. Bodnarchuk, Frank Krumeich, Gökhan Kara, Ioan Shorubalko, Manu V. Nair, Graham A. Cooke, Thomas Lippert, Giacomo Indiveri and Maksym V. Kovalenko.*

** These authors contributed equally.*

Many in-memory computing frameworks demand electronic devices with specific switching characteristics to achieve the desired level of computational complexity. Existing memristive devices cannot be reconfigured to meet the diverse volatile and non-volatile switching requirements, and hence rely on tailored material designs specific to the targeted application, limiting their universality. "Reconfigurable memristors" that combine both ionic diffusive and drift mechanisms could address these limitations, but they remain elusive. Here we present a reconfigurable halide perovskite nanocrystal memristor that achieves ondemand switching between diffusive/volatile and drift/non-volatile modes by controllable electrochemical reactions. Judicious selection of the perovskite nanocrystals and organic capping ligands enable state-of-the-art endurance performances in both modes - volatile (2×10^6 cycles) and non-volatile (5.6×10^3 cycles). We demonstrate the relevance of such proof-of-concept perovskite devices on a benchmark reservoir network with volatile recurrent and non-volatile readout layers based on 19,900 measurements across 25 dynamically-configured devices.

4.1 INTRODUCTION

The human brain operating at petaflops consumes less than 20 W, setting a precedent for scientists that real-time, ultralow-power data processing in a small volume is possible. Inspired by the human brain, the field of neuromorphic computing attempts to emulate various computational principles of the biological substrate by engineering unique materials [227–229] and circuits [29, 230, 231]. In the context of hardware implementation of neural networks, the discovery of memristors has been one of the main driving forces for highly efficient in-memory realizations of synaptic operations. Similar to evolution optimizing neurons and synapses by exploiting stable and metastable molecular dynamics [232], memristive devices of various physical mechanisms [25, 233, 234] have been discovered and developed with different volatile and non-volatile specifications. Since their inception, memristors have been utilized to implement a wide gamut of applications [235] such as stochastic computing [236], hyperdimensional computing [237], spiking [238] and artificial neural networks [95]. However, many of these frameworks often demand very different hardware specifications [16] (Fig. 1a). To meet these specifications, the memristor fabrication processes are often tediously engineered to reflect the requirements of targeted neural network configurations (e.g., neural encoding, synaptic precision, etc.). For example, the latest state-of-the-art spiking neural network (SNN) models [75, 197] require memory elements operating at multiple timescales, with both volatile and non-volatile properties (from tens of milliseconds to hours) [144]. The current approach of optimizing memristive devices to a single requirement hinders the possibility of implementing multiple computational primitives in neural networks and precludes their monolithic integration on the same hardware substrate.

In this regard, the realization of drift and diffusive memristors have garnered significant attention. Drift memristors portraying non-volatile memory characteristics are typically designed using oxide dielectric materials with a soft-breakdown behaviour. In combination with inert electrodes, the switching mechanism is determined by filaments of oxygen vacancies (valence change memory); whereas implementations with reactive electrodes rely on electrochemical

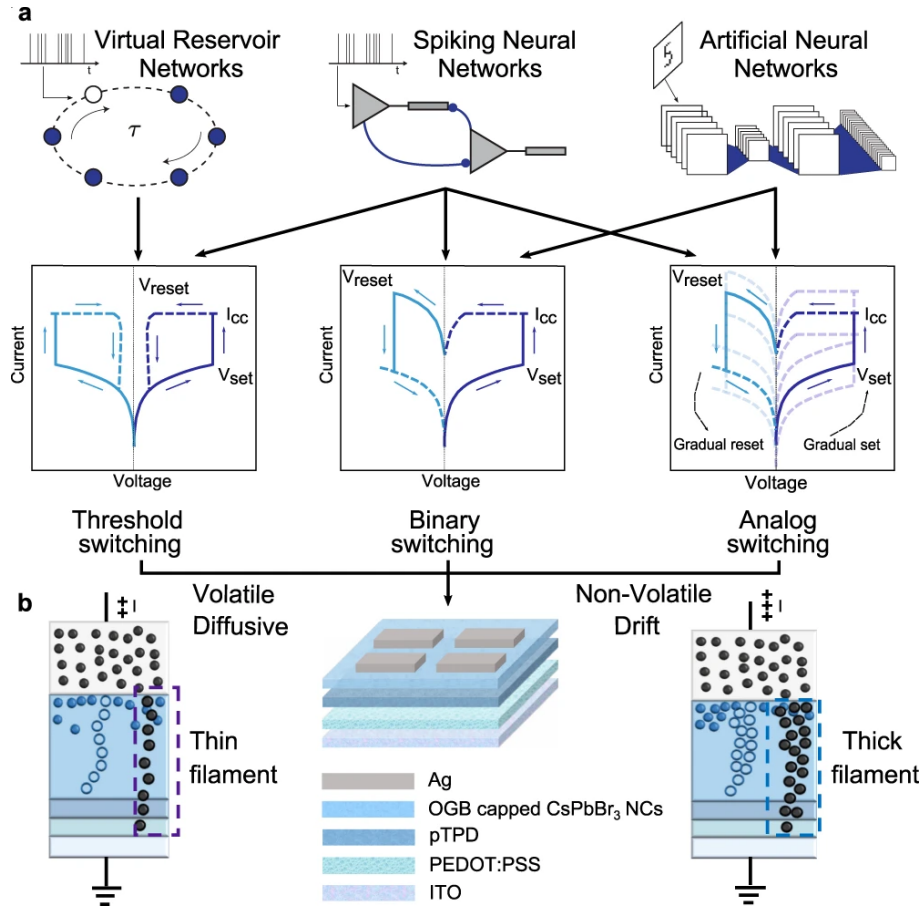


FIGURE 4.1: (a) Different neural network frameworks demand particular switching characteristics from in-memory computing implementations. For example, delay systems [239] (dynamical non-linear systems with delayed feedback such as virtual reservoir networks), should exhibit only a fading memory to process the inputs from the recent past. Such short-term dynamics are best represented by volatile thresholdswitching memristors [240]. SNNs often demand both volatile and non-volatile dynamics, simultaneously. Synaptic mechanisms requiring STP and eligibility traces [241] can be implemented using volatile memristors [24, 151] whereas synaptic efficacy requires either efficient binary-switching [20] or analog switching devices. Lastly, ANN performances specifically benefit from non-volatile features such as multi-level bit precision of weights and linear conductance response during the training phase [21, 22] (b) A reconfigurable memristor with active control over its diffusive and drift dynamics may be a feasible unifying solution. Schematic of the reconfigurable halide perovskite nanocrystal memristor is shown for reference. We utilize the same active switching material (CsPbBr₃NCs capped with OGB ligands) to implement two distinct types of computation in the RC framework. The volatile diffusive mode exhibiting short-term memory is utilized as the reservoir layer while the non-volatile drift mode exhibiting long-term memory serves as the readout layer.

reactions to form conductive bridges (electrochemical metallization memory) [242]. Such drift-based memristors fit well for emulating synaptic weights that stay stable between weight updates. In contrast, diffusive memristors are often built with precisely embedded clusters of metallic ions with low diffusion activation energy within a dielectric matrix [234]. The large availability of such mobile ionic species and their low diffusion activation energy facilitate spontaneous relaxation to the insulating state upon removing power, resulting in volatile threshold switching. Memristive devices with such short-term volatility, are better suited to process temporally-encoded input patterns [243]. Hence, the application determines the type of volatility, bit-precision or endurance of the memristors, which are then heavily tailored by tedious material design strategies to meet these demands [16]. For example, deep neural network (DNN) inference workloads require linear conductance response over a wide dynamic range for optimal weight update and minimum

noise for gradient calculation [21, 22, 95]. Whereas SNNs often demand richer and multiple synaptic dynamics simultaneously e.g., short term conductance decay (to implement synaptic cleft phenomena such Ca^{2+} -dependent short-term plasticity (STP) and CAMKII-related eligibility traces [244]), non-volatile device states (to represent synaptic efficacy) and a probabilistic nature (to mimic synaptic vesicle releases [243]) (Fig. 1a). However, optimizing the active memristive material for each of these features limits their feasibility to suit a wide range of computational frameworks and ultimately increases the system complexity for most demanding applications. Moreover, these diverse specifications cannot always be implemented by combining different types of memristors on a monolithic circuit e.g., volatile and non-volatile, binary and analog, due to the incompatibility of the fabrication processes. Therefore, the lack of universality of memristors that realize not only one, but diverse computational primitives is an unsolved challenge today.

A reconfigurable memristive computing substrate that allows active control over their ionic diffusive and drift dynamics can offer a viable unifying solution but is hitherto undemonstrated. Although dual-functional memory behaviour has been observed previously, the dominance of one of the mechanisms often results in poor switching performance for either one or both modes, limiting the employability of such devices for demanding applications [96, 97]. To the best of our knowledge, there is no report yet of a reconfigurable memristive material that can portray both volatile diffusive and multi-state non-volatile drift kinetics, exhibit facile switching between these two modes, and still pertain excellent performance.

Here we report a reconfigurable memristor computing substrate based on halide perovskite nanocrystals that achieves on-demand switching between volatile and non-volatile modes by encompassing both diffusive and drift kinetics (Fig. 1b). Halide perovskites are newcomer optoelectronic semiconducting materials that have enabled state-of-the-art solar cells [245], solid state light emitters [246, 247] and photodetectors [248–250]. Recently, these materials have attracted significant attention as memory elements due to their rich variety of charge transport physics that supports memristive switching, such as modulatable ion migration [251–253], electrochemical metallization reactions with metal electrodes [254] and localized interfacial doping with charge transport layers [255]. While most reports are based on thin films or bulk crystals of halide perovskites [251–253, 256], interestingly perovskite nanocrystal (NC)-based formulations have been much less investigated till date [244, 257]. NCs in general are recently garnering significant attention for artificial synaptic implementations because they support a wide range of switching physics such as trapping and release of photogenerated carriers at dangling bonds over a broad spectral region [258], and single-electron tunnelling [259]. They allow low-energy ($< \text{fJ}$), high-speed (MHz) operation, and can support scalable and CMOS-compatible fabrication processes. In the case of perovskite NCs, however, existing implementations often utilize NCs only as a charge trapping medium to modulate the resistance states of another semiconductor, in flash-like configurations a.k.a synaptic transistor [260–263]. The memristive switching capabilities and limits of the perovskite NC active matrix remains unaddressed, entailing significant research in this direction. Colloids of perovskite nanocrystals (NCs) are readily processable into thin-film NC solids and they offer a modular approach to impart mesoscale structures and electronic interfaces, tunable by adjusting the NC composition, size and surface ligand capping.

Our device comprises all-inorganic cesium lead bromide (CsPbBr_3) NCs capped with organic ligands as the active switching matrix and silver (Ag) as the active electrode. The design principle for realizing reconfigurable memristors revolves around two main factors. (i) From a material selection perspective, the low activation energy of migration of Ag^+ and Br^- allows easy formation of conductive filaments. The soft lattice of the halide perovskite NCs facilitates diffusion of the mobile ions. Moreover, the organic capping ligands help regulate the extent of electrochemical reactions, resulting in high endurance and good reconfigurability. (ii) From a peripheral circuit design perspective, active control of the compliance control (I_{cc}) determines the magnitude of flux of the mobile ionic species and in turn allows facile switching between volatile diffusive and multi-bit non-volatile drift modes of operation.

The surface capping ligands are observed to play a vital role in determining the switching characteristics and endurance performance. CsPbBr_3 NCs capped with didodecyldimethylammonium bromide (DDAB) ligands display poor switching performance in both volatile (10 cycles) and non-volatile (50 cycles) modes, whereas NCs capped with oleylguanidinium bromide (OGB)

ligands exhibit record-high endurance performances in both volatile (2 million cycles) as well as non-volatile switching (5655 cycles) modes [240, 255, 264]

To validate our approach and demonstrate the advantages of such reconfigurable memristive materials, we use a benchmark model of a fully-memristive reservoir computing (RC) framework interfaced to an artificial neural network (ANN) [240]. The reservoir is modelled as a network of recurrently-connected units whose dynamics act as short-term memory. Any temporal signal entering the reservoir is subject to a high-dimensional nonlinear transformation that enhances the separability of its temporal features. A linear read-out ANN layer is then connected to the reservoir units with all-to-all connections and trained to perform classification based on the temporal information maintained in the reservoir. Our RC implementation comprises perovskite memristors that are configured as diffusion-based volatile dynamic elements to implement the reservoir nodes and as drift-based non-volatile weights to implement the readout ANN layer. In their diffusive mode, the low activation energy of ion migration of the mobile ionic species (Ag^+ and Br^-) enables volatile threshold switching. The resulting short-term dynamics are essential for capturing temporal correlations within the input data stream. In the drift mode, stable conductive filaments formed by the drift of the ionic species facilitate programming of non-volatile synaptic weights in the readout layer for both training and inference. Furthermore, the readout layer can be trained online via active regulation of the I_{cc} which allows precise selection of the drift dynamics and enables multiple-bit resolution in the low resistive state (LRS). Using neural firing patterns, we show via both experiments and simulations that a RC framework based on reconfigurable perovskite memristors can accurately extract features in the temporal signals and classify firing patterns.

4.2 DIFFUSIVE MODE OF THE PEROVSKITE RECONFIGURABLE MEMRISTOR

We investigate two systems for diffusive dynamics—didodecyldimethylammonium bromide (DDAB) and oleylguanidinium bromide (OGB)-capped $\text{CsPbBr}_3\text{NCs}$. The device structure comprises indium tin oxide (ITO), poly(3,4-ethylenedioxythiophene) polystyrene sulfonate (PEDOT:PSS), poly(N,N'-bis-4-butylphenyl-N,N'-bisphenyl)benzidine (polyTPD), $\text{CsPbBr}_3\text{NCs}$ and Ag (see "Methods" section). With an I_{cc} of $1\mu\text{A}$, both material systems portray volatile threshold switching characteristics with diffusive dynamics and spontaneous relaxation back to the initial state, albeit with contrasting endurance. The DDAB-capped perovskite NCs exhibit a poor on-off ratio (volatile memory a.k.a. VM $I_{\text{power ON}}/I_{\text{power OFF}} \sim 10$) and quick transition to a non-volatile state, resulting in an inferior volatile endurance of ~ 10 cycles. On the other hand, the OGB-capped perovskite NCs depict a highly robust threshold switching behaviour with sub-1 V set voltages, VM $I_{\text{power ON}}/I_{\text{power OFF}} \sim 10^3$ and a record volatile endurance of 2×10^6 cycles (Fig. 3a). The volatile threshold switching behaviour can be attributed to the redistribution of Ag^+ and Br^- ions under an applied electric field, and their back-diffusion upon removing power [253, 265, 266]. It is also important to note that both these devices exhibit a unidirectional DC threshold switching behaviour with no switching occurring under reverse bias (negative voltage on the Ag electrode). This can be correlated to the dominant bipolar electrode effect over thermal-driven diffusion, in alignment with literature [267–269]

4.3 DRIFT MODE OF THE PEROVSKITE RECONFIGURABLE MEMRISTOR

Upon increasing the I_{cc} to 1 mA, both the DDAB and OGB-capped CsPbBr_3NC memristors portray typical non-volatile bipolar resistive switching characteristics, once again with contrasting endurance (Fig. 4.2, Fig. 4.3 and Supplementary Fig. A.22). Both systems depict forming-free operations and similar on-off ratios ($\geq 10^3$). However, the DDAB capped perovskite NCs quickly transit to a non-erasable non-volatile state, resulting in an inferior non-volatile endurance of -50 cycles (Supplementary Fig. A.23). On the other hand, the OGB-capped perovskite NC-based memristor portrays a highly robust switching behaviour with sub-1 V set voltages, and record-high non-volatile endurance and retention of 5655 cycles and 10^5 s, respectively (Fig. 4.3, Supplementary Fig. A.24). Similar to the volatile threshold switching mechanism, the nonvolatile resistive

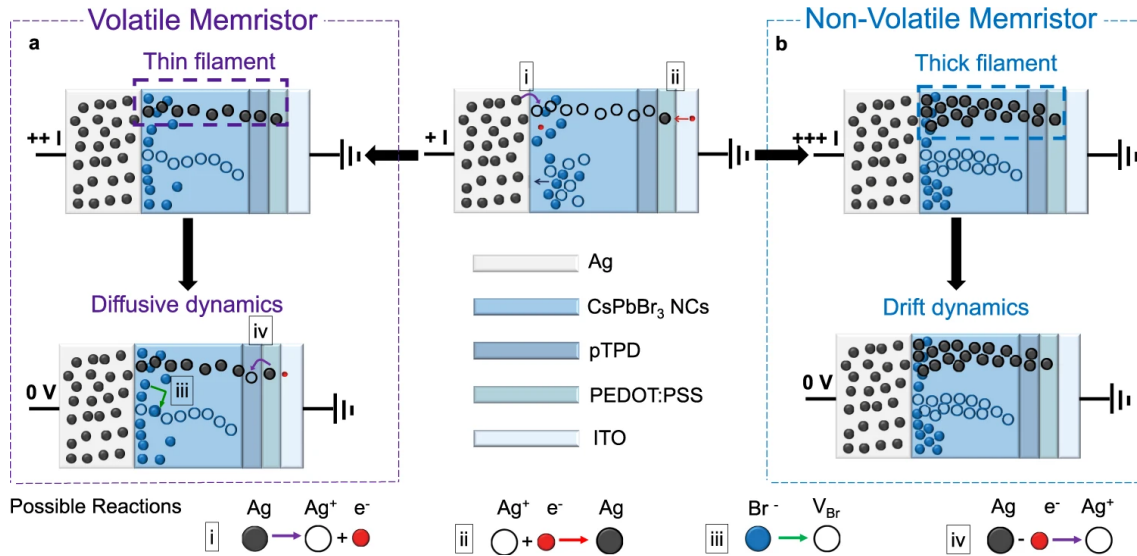


FIGURE 4.2: The device structure comprises ITO (100 nm), PEDOT:PSS (30nm), polyTPD (20 nm), OGB-capped CsPbBr₃NCs(20 nm) and Ag(150 nm). (a) Diffusive mode- illustration of the proposed volatile diffusive switching mechanism. (b) Drift mode-illustration of the proposed non-volatile drift switching mechanism. Additional note: The thickness of the individual layers in the device schematic are not drawn to scale to match the experimentally-measured thicknesses. The perovskite layer is not a bulk semiconductor, but 1-2 layers of nanocrystals (NCs). The schematic is drawn for simplicity, to illustrate the formation and rupture of conductive filaments (CFs) of Ag through the device structure.

switching can also be attributed to redistribution of ions, and electrochemical reactions under an applied electric field [251, 252]. The larger I_{cc} of 1 mA results in permanent and thicker conductive filamentary pathways, and the switching dynamics is now dominated by the drift kinetics of the mobile ion species Ag^+ and Br^- , rather than diffusion.

In the case of DDAB-capped CsPbBr₃NCs, the inferior volatile endurance, quick transition to a non-volatile state and mediocre non-volatile endurance indicates poor control of the underlying electrochemical processes and formation of permanent conductive filaments even at low compliance currents. On the other hand, capping CsPbBr₃NCs with OGB ligands enables better regulation of the electrochemical processes, resulting in superior on-off ratio, volatile endurance as well as non-volatile endurance. Scanning Electron Microscope (SEM) images indicate similar film thickness in both devices, ruling out dependence on the active material thickness (Fig. 4.3). Transmission Electron Microscopy (TEM) and Atomic Force Microscopy (AFM) images reveal similar nanocrystal size (~ 10 nm) and surface roughness for both films, dismissing variations in crystal size and morphology as possible differentiating reasons (Fig. 4.3 and Supplementary Fig. A.25). While the exact mechanism is still unknown, the larger size of the OGB ligands compared to DDAB (2.3 nm vs. 1.7 nm) could intuitively provide better isolation to the CsPbBr₃NCs and prevent excess electrochemical redox reactions of Ag^+ and Br^- , modulating the formation and rupture of conductive filaments. This comparison is further supported by photoluminescence measurements, pointing to a larger drop of luminescence quantum yield in the films of DDAB-capped NCs, arising from the stronger excitonic diffusion and trapping.

To probe the mechanism further, devices with Au as the top electrode were fabricated, but did not show any resistive switching behaviour. The devices do not reach the compliance current of 1 mA during the set process and do not portray the sudden increase in current, typical of filamentary memristors. This indicates that Ag is crucial for resistive switching and also proves that Br⁻ ions play a trivial role in our devices if any. Control experiments on PEDOT:PSS only and PEDOT:PSS + pTPD devices further reiterate importance of the perovskite NC thin film as an active matrix for reliable and robust Ag filament formation and rupture. Secondary ion mass spectrometry (SIMS) profiling reveals a clear difference in the ¹⁰⁷Ag cross section profile

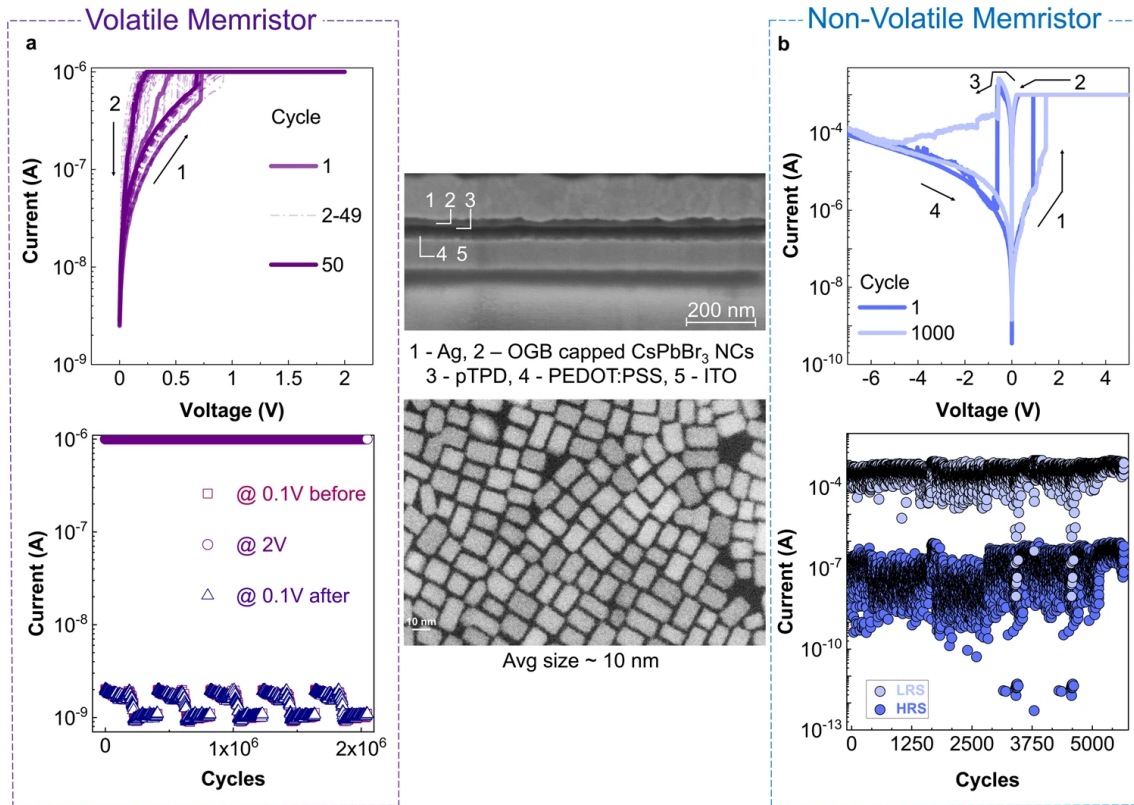


FIGURE 4.3: The device structure comprises ITO (100 nm), PEDOT:PSS (30 nm), polyTPD (20 nm), OGB-capped CsPbBr₃NCs(20 nm) and Ag(150 nm) as shown in the SEM cross-section. Thickness of the individual layers were confirmed by AFM. The TEM image reveals NCs with an average diameter of ~10 nm. (a) Diffusive mode- evolution of the device conductance upon applying DC sweep voltages (0 V → 2 V → 0 V) with an $I_{cc} = 1\mu A$ (top), endurance performance (bottom). (b) Drift mode- evolution of the device conductance upon applying DC sweep voltages (0 V → +5 V → 0 V → -7 V → 0 V) with an $I_{cc} = 1\text{ mA}$ during SET operation (top), endurance performance (bottom).

when comparing an ON and OFF device. An increase of the ¹⁰⁷Ag count is observed at the interface between the halide perovskite and the organic layers for the device in the ON state. Temperature-dependent measurements further confirm the theory of migration of Ag⁺ ions through the perovskite matrix. The conclusions in this study are observed to be independent of the NC layer thickness, NC size and dispersity.

4.4 RESERVOIR COMPUTING WITH PEROVSKITE MEMRISTORS

To demonstrate the advantages of the reconfigurability features of our perovskite memristors, we model a fully-memristive RC framework with dynamically-configured layer of virtual volatile reservoir nodes and a readout ANN layer with non-volatile weights in simulation. In particular, we address three distinct forms of computational requirements using the reconfigurability of the proposed device: an accumulating/decaying short-term memory for the temporal processing in the reservoir; a stable long-term memory for retaining trained weights in the readout layer, and a circuit methodology for accessing analog states from binary devices to enhance the training performance.

4.5 DIFFUSIVE PEROVSKITE MEMRISTORS AS RESERVOIR ELEMENTS

To implement the reservoir layer with the fabricated memristor devices, we utilize the virtual node concept originally proposed by Appeltant et al. [239]. Instead of conventional transforming of the input signal to a high-dimensional reservoir state by processing over many non-linear units, the virtual node concept employs the idea of delayed feedback on a single physical device exhibiting strong short-term effects. Under the influence of a sequential input, the dynamical device state goes through a non-linear transient response, which is recorded with fixed timesteps to create a set of virtual nodes representing the reservoir state. Hence, the transient device non-linearity constitutes temporal processing, and the delay system forms the high dimensional representation in the reservoir.

Elements of a reservoir layer should ideally possess a fading memory (sometimes called short-term memory or echo state property) and non-linear internal dynamics [270]. The fading memory effect plays a key role in extracting features in the temporal domain of the input data stream, while the non-linear internal dynamics enable projection of temporal features to a high-dimensional state with good separability [271]. Response of the OGB-capped CsPbBr₃NC memristors to low-voltage electrical spikes reveal short-term/fading diffusive dynamics with a relaxation time ≥ 5 ms for an input pulse duration = 20 ms and amplitude = 1 V. Non-linear internal dynamics are evident in 4 formats- (i) from the transient evolution of the device conductance during the stimulations; and from the final device conductance as a function of the applied pulse (ii) amplitude, (iii) width and (iv) number (Supplementary Fig. A.26). An additional test of the echo state property reveals that the present device state is reflective of the input temporal features in the recent past (< 23 ms) but not the far past, enabling efficient capture of short-term dependencies in the input data stream (Supplementary Fig. A.27). Stimulation of pulse streams with different temporal features results in distinct temporal dynamics of memristor states.

4.6 DRIFT PEROVSKITE MEMRISTORS AS READOUT ELEMENTS

Storing the weight of the fully-connected readout layer of the ANN requires non-volatile synaptic devices. For representing synaptic efficacy, we use the drift-based perovskite memristor configuration that enables stable access to multiple conductance states. Because synaptic efficacy in ANNs can be either positive or negative, we use two memristor devices G^+ and G^- in a differential architecture to represent a single synapse [272]. Hence, synaptic potentiation is obtained by increasing the conductance of G^+ , and depression by increasing the conductance of G^- with identical pulses. The effective synaptic strength is expressed by the difference between the two conductances ($G^+ - G^-$). Arranged in a crossbar array with the differential configuration, synaptic propagation at the readout layer is realized efficiently, governed by Kirchhoff's Current Law and Ohm's Law at $O(1)$ complexity [273].

Like most filament-based memristors, our devices display non-volatile switching across only two stable states (binary) and suffer from the lack of access to true analog conductance states for synaptic efficacy. This low bit resolution during learning has been empirically shown to cause poor network performance [274, 275]. To have more granular control over the filament formation, we migrate a recently proposed programming approach for oxide memristors to halide perovskites [276]. We achieve multi-level stable conductance states in the device's low resistance regime by modulating the programming I_{cc} . In comparison to the undesirable nonlinear transformations seen in HfO₂ devices, the mapping from I_{cc} to conductance follows a linear relation for the drift-based CsPbBr₃NC devices, hence providing linear mapping to the desired conductance values (see below). This enables controlled weight updates using a single shot without requiring a write-verify scheme.

We use I_{cc} modulation to train the readout layer of the reservoir network (see "Methods") using the statistical measurement data from the devices. For every input pattern received from reservoir nodes, the readout layer produces a classification prediction via a sigmoid activation function. Depending on the classification error, the desired conductance changes of each differential

memristor pair per synapse are calculated. The memristive weights are then updated with the corresponding I_{cc} , resulting in the desired conductance values.

4.7 CLASSIFICATION OF NEURAL FIRING PATTERNS

Next, we present a virtual reservoir neural network [239, 277] simulation with the short-term diffusive configuration of perovskite memristors in the reservoir layer and long-term stable drift configuration in the trainable readout layer (Fig. 4a). The network is tested on the classification of the four commonly observed neural firing patterns in the human brain: Bursting, Adaptation, Tonic, and Irregular [278]. These spike trains (Supplementary Fig. A.28) are applied to a single perovskite memristor in the reservoir layer, whose diffusive dynamics constitute a short-term memory between 5 and 20 ms timescale. We exploit the concept of a virtual reservoir, where each reservoir node is uniformly sampled at finite intervals to emulate the rich non-linear temporal processing in reservoir computing. We use a sampling interval of 35 ms, resulting in a population of 30 virtual reservoir nodes representing the temporal features across 1050 ms long neural firing patterns. The device responses are derived from electrical measurements of 25 different memristive devices (Fig. 4b). Both device-to-device and cycle-to-cycle variability are captured with extensive measurements. Stimulation with "Bursting" spikes results in an accumulative behaviour within each high-frequency group and an exponential decay in the inter-group interval, reflective of the fading memory and non-linear internal dynamics as described above. "Adaptive" patterns trigger weakened accumulative behaviour as a function of the pulse interval, "Irregular" results in random accumulation and decay, while "Tonic" generates states with no observable accumulation. As the last stage of computation, these features are projected to a fully-connected readout layer with 4 sigmoid neurons (see "Methods"). The reservoir network achieves a classification accuracy of 85.1% with the training method of modulating the programming I_{cc} of drift-based perovskite weights in the readout layer (Fig. 4c). Remarkably, with double-precision floating-point weights trained with the Delta rule [195] on readout, the test accuracy is 91.8% confirming the effectiveness of our I_{cc} approach (Supplementary Fig. A.29, A.30, A.31). The training and test accuracy over 5 epochs demonstrates that both networks are not overfitting the training data (Fig. 4.4, Supplementary Table A.1).

4.8 DISCUSSION

We present robust halide perovskite NC-based memristive switching elements that can be reconfigured to exhibit both volatile diffusive and non-volatile drift dynamics. This represents a significant advancement in the experimental realization of memristors. In comparison to pristine volatile and non-volatile memristors, our reconfigurable CsPbBr₃NC memristors can be utilized to implement both neurons and synapses with the same material/device platform and adapt to diverse computational primitives without additional modifications to the device stack at run-time. The closest comparison to our devices are dual functional memristors- those that exhibit both volatile and non-volatile switching behaviours without additional materials or device engineering. While impressive demonstrations of dual functional memristors exist, many devices require an electroforming step to initiate the resistive switching behaviour and most importantly, the endurance and retention performance are often limited to < 500 cycles in both modes and $\leq 10^4$ s respectively. In comparison, we report a record-high endurance of 2 million cycles in the volatile mode, 5655 cycles in the non-volatile mode, and a retention of 10^5 s, highlighting the significance of our approach. This makes these devices ideal for always-on online learning systems. The forming-free operation, and low set-reset voltages would allow low power vector-matrix multiplication operations, while the high retention and endurance ensure precise mapping of synaptic weights during training and inference of artificial neural networks. In contrast to most metal oxide-based diffusive memristors that require high programming currents to initiate filament formation (≥ 1 V or/and $\geq 10\mu$ A), our devices demonstrate forming-free volatile switching at lower voltages and currents (≤ 1 V and $\leq 1\mu$ A). This is possibly due to the lower activation energy for Ag⁺ and Br⁻ migration in halide perovskites compared to oxygen

vacancies in oxide dielectrics, softer lattice of the halide perovskite layer and the large availability of mobile ion species in the halide perovskite matrix. Most importantly, our devices can be switched to the volatile mode even after programming multiple non-volatile states, proving true "reconfigurability" (Supplementary Fig. A.32). Such behaviour is an example of the neuromorphic implementation of synapses in SNNs that demand both volatile and non-volatile switching properties, simultaneously (see Fig. 4.1a). It is important to note that existing implementations of dual functional devices cannot be reconfigured back to the volatile mode once the nonvolatile mode is activated, making our device concept and its use case for neuromorphic computing unique.

In operando thermal camera imaging provides further support to our hypothesis of better management of the electrochemical reactions with the OGB ligands when compared to DDAB, and points to the importance of investigating nanocrystal-ligand chemistry for the development of high-performance robust memristors. While the exact memristive mechanism is still unclear, our results favour NC film implementations over thin films empirically. The insights derived on the apt choice of the capping ligands paves way for further investigations on nanocrystal-ligand chemistry for the development of high-performance robust memristors. The ability to reconfigure the switching mode ondemand allows easy implementation of multiple computational layers with a single technology, alleviating the hardware system design requirements for new neuromorphic computational frameworks. Our work complements and goes beyond previous model-based implementations [240], by comprehensively characterizing diffusive and drift devices for ~ 5000 patterns of different input spike streams, and collecting statistical data on device-to-device and cycle-to-cycle variability, device degradation, temporal conductance drift and real-time nanoscopic changes in memristor conductance. This statistical data is incorporated in the simulations for a very accurate modelling of the device behaviour for this task. To the best of our knowledge, this is the first time this extent of systematic analysis is being done to use the same device for both diffusive and drift behaviour for a real-world benchmark. Given the excellent performance and record endurance of our reconfigurable halide perovskite memristors, this opens way for a completely novel type of memristive substrate, for applications such as time series forecasting and feature classification.

4.9 METHODS

DEVICE FABRICATION Indium tin oxide (ITO, $7\Omega\text{cm}^{-2}$) coated glass substrates were cleaned by sequential sonication in helmanex soap, distilled water, acetone, and isopropanol solution. Substrates were dried and exposed to UV for 15 min. PEDOT:PSS films were deposited by spincoating (4000 rpm for 25 s) the precursors (Clevios, Al 4083) and followed by annealing at 130°C for 20 min. PolyTPD (Poly[N,N'-bis(4-butylphenyl)-N,N'-bisphenylbenzidine]) dissolved in chlorobenzene (4mg/ml) was then spin-coated at 2000rpm, 25 s; followed by annealing at 130°C for 20 min. Solutions of CsPbBr₃NCs capped with DDAB and OGB were next deposited via spin coating (2000 rpm for 25 s). Finally, -150 nm of Ag was thermally evaporated through shadow masks ($100\mu\text{m} \times 100\mu\text{m}$) to complete the device fabrication.

ELECTRICAL MEASUREMENTS For endurance testing in the volatile mode, write and read voltages of +2 V and +0.1 V were used respectively with a pulse width of 5 ms. The following methodology was used: 1. read the current level of the device using +0.1 V, 2. apply +2 V for 5 ms as the write pulse and monitor the device's current level, 3. repeat step 1. For the non-volatile mode, write voltage of +5 V, erase voltage of -7 V and read voltage of +0.1 V were used. The following methodology was used: 1. read the current level of the device using +0.1 V, 2. apply +5 V / -7 V for 5 ms as the write/erase pulse, 3. repeat step 1 and extract the on-off ratio comparing steps 1 and 3. Note: Since our VM loses the stored information upon removing power, the ON state ($I_{\text{power ON}}$) is reported as the current value corresponding to the application of the programming pulse (at 2 V) and the OFF state ($I_{\text{power OFF}}$) is reported as the current value corresponding to the application of the reading pulse (at 0.1 V), in alignment with the reported literature [234]. For endurance measurements in the non-volatile memory (NVM) mode, the

conventional methodology was used, i.e., the ON-OFF ratios were extracted from the current values corresponding to the same reading pulse (0.1 V).

NEURAL SPIKE PATTERN DATASET GENERATION The neural spike pattern dataset consists of samples of four classes: Bursting, Adaptation, Tonic, and Irregular. "Bursting" firing patterns are defined as groups of high-frequency spikes with a constant inter-group interval; "Adapting" corresponds to spikes with gradually increased intervals; "Tonic" denotes low-frequency spikes with a constant interval; and "Irregular" corresponds to spikes that fire irregularly. In total, the dataset consists of 4975 patterns (199 cycles applied to 25 devices) for each of the four types. Each pattern is -1050 ms long, where spikes are emulated with square wave voltage pulses (1 V, 25 ms). For Bursting patterns, each spike train consists of 4 – 5 highfrequency burst groups (4 spikes per burst group) with an interspike interval (ISI) of 5 ms. Between bursts, there exist 75-125 ms intervals. For Adaptation patterns, each spike train starts with high-frequency pulses with an ISI of 5 ms and gradually increases 50% with each new spike (with 5% standard deviation). For Tonic patterns, a regular spiking pattern with an average ISI of 70 ms is used. For each ISI, 5% standard deviation is applied. For irregular patterns, spike trains are divided into 60 ms segments, and a spike is assigned randomly with a 50% probability to the beginning of each segment.

SIMULATION OF NEURAL NETWORKS For classifying neural spike patterns, a fully-connected readout layer with 30 inputs and 4 outputs is used. In addition, there is one bias unit in the input. The 4 neurons at the output are sigmoid neurons. For training, 90% of the neural spike pattern dataset is used over 5 epochs. At the end of each epoch, the network performance is tested with the rest 10% of the dataset. During I_{cc} modulated training, each synapse comprises two conductance values in a differential configuration. The differential current is scaled such that $W = \beta (G^+ - G^-)$, where $\beta = 1 / (G_{max} - G_{min})$, corresponds to maximum and minimum allowed conductance values of memristors. Conductances are initialized randomly with a Normal distribution ($\mu_G = 0.5\text{mS}$ and $\sigma_G = 0.1\text{mS}$). Network prediction is selected deterministically by choosing the output neuron with the maximum activation. After the prediction, the L_1 loss is calculated. Then, weight change that reflects a step in the direction of the ascending loss gradient is calculated with $\Delta W = (\eta x_i \delta_j) / \beta$, where η is the learning rate, x_i is the reservoir node output, δ_j is the calculated loss and $1/\beta$ is the scaling factor between weights and conductances. Target weights are clipped between 0.1mS and 3.5mS. Subsequently, I_{cc} values corresponding to the target conductances are calculated (Supplementary Fig. A.31). Finally, we sample new conductance values from a Normal distribution whose mean and standard deviation is calculated using linear functions of I_{cc} . For the double-precision floating-point-based training, the same readout layer size is used. Network loss is calculated via the Mean Squared Error. Weights are adjusted using the Delta rule with an adaptive learning rate [175]. Both networks are trained with a batch size of 1 and a suitably tuned hyperparameters.

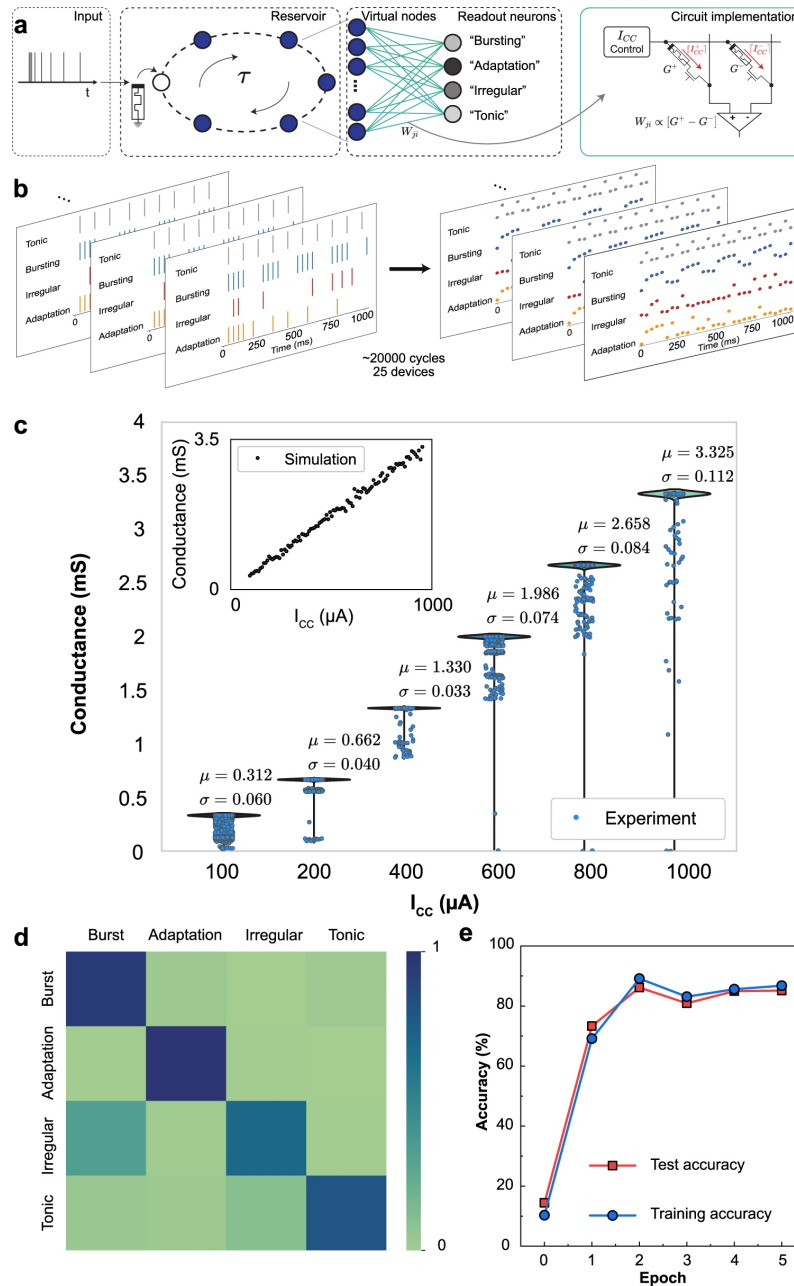


FIGURE 4.4: (a) An ANN is trained to perform classification using the temporal properties of the reservoir, in response to a series of inputs representing neural firing patterns. Using I_{cc} control, OGB-capped CsPbBr₃NC memristors are configured to the diffusion-based volatile mode to serve as virtual nodes in the reservoir; and to the drift-based non-volatile mode to implement synaptic weights in the ANN readout layer. During single inference, a neural firing pattern represented as a short-voltage pulse train is applied to a single diffusive-mode perovskite device. Based on the virtual node concept [239] temporal features of the input signal are intrinsically encoded as an evolving conductance of the device due to their nonlinear short-term memory effects. This evolving device state is sampled with equal intervals of 35 ms in time, denoting 30 virtual nodes that jointly represent the reservoir state. These virtual node states are delayed and fed into the readout layer, whose weights, W_{ji} (size of 30×4), are implemented by the drift-mode non-volatile perovskite memristors, placed in a differential configuration [115]. Classification of neural firing patterns. (b) Experiments. The memristive reservoir elements are stimulated using four common neural firing input patterns - "Bursting", "Adapting", "Tonic" and "Irregular". During the presentation of inputs, the evolution of the device conductance is monitored. Each spike in the input data stream is realized as a voltage pulse of 1 V amplitude and 20 ms duration, while the device states are read with -0.5 V, 5 ms pulses. (c) Distribution of the programmed perovskite memristor non-volatile conductances with I_{cc} modulation. The inset shows the simulated linear $I_{cc} \rightarrow G$ relation. Simulations. (d) Normalized confusion matrix shows the classification results with the I_{cc} controlled training scheme. The RC performs slightly worse in irregular patterns due to lack of temporal correlations among samples. (e) Training (86.75%) and test (85.14%) accuracies of the fully-memristive RC framework.

MOSAIC: AN ANALOG SYSTOLIC ARCHITECTURE FOR IN-MEMORY COMPUTING AND ROUTING

This chapter's content was published in Nature Communications, featured as one of 50 best papers recently published in the field. The original publication is authored by Yigit Demirag, Thomas Dalgaty*, Filippo Moro*, Alessio De Pra, Giacomo Indiveri, Elisa Vianello and Melika Payvand.*

** These authors contributed equally.*

The brain's connectivity is locally dense and globally sparse, forming a small-world graph—a principle prevalent in the evolution of various species, suggesting a universal solution for efficient information routing. However, current artificial neural network circuit architectures do not fully embrace small-world neural network models. Here, we present the neuromorphic Mosaic: a non-von Neumann systolic architecture employing distributed memristors for in-memory computing and in-memory routing, efficiently implementing small-world graph topologies for SNNs. We've designed, fabricated, and experimentally demonstrated the Mosaic's building blocks, using integrated memristors with 130 nm CMOS technology. We show that thanks to enforcing locality in the connectivity, routing efficiency of Mosaic is at least one order of magnitude higher than other SNN hardware platforms. This is while Mosaic achieves a competitive accuracy in a variety of edge benchmarks. Mosaic offers a scalable approach for edge systems based on distributed spike-based computing and in-memory routing.

5.1 INTRODUCTION

Despite millions of years of evolution, the fundamental wiring principle of biological brains has been preserved: dense local and sparse global connectivity through synapses between neurons. This persistence indicates the efficiency of this solution in optimizing both computation and the utilization of the underlying neural substrate [30]. Studies have revealed that this connectivity pattern in neuronal networks increases the signal propagation speed [279], enhances echo-state properties [280] and allows for a more synchronized global network [281]. While densely connected neurons in the network are attributed to performing functions such as integration and feature extraction functions [282], long-range sparse connections may play a significant role in the hierarchical organization of such functions [283]. Such neural connectivity is called small-worldness in graph theory and is widely observed in the cortical connections of the human brain [279, 284, 285] (Fig. 5.1a, b). Small-world connectivity matrices, representing neuronal connections, display a distinctive pattern with a dense diagonal and progressively fewer connections between neurons as their distance from the diagonal increases (see Fig. 5.1c).

Crossbar arrays of non-volatile memory technologies e.g., Floating Gates [287], RRAM [139, 191, 288–291], and PCM [138, 292–294] have been previously proposed as a means for realizing artificial neural networks on hardware (Fig. 5.1d). These computing architectures perform in-memory vector-matrix multiplication, the core operation of artificial neural networks, reducing the data movement, and consequently the power consumption, relative to conventional von Neumann architectures [144, 287, 295–299].

However, existing crossbar array architectures are not inherently efficient for realizing small-world neural networks at all scales. Implementing networks with small-world connectivity in a large crossbar array would result in an under-utilization of the off-diagonal memory elements (i.e., a ratio of non-allocated to allocated connections > 10) (see Fig. 5.1d and Supplementary Note 1). Furthermore, the impact of analog-related hardware non-idealities such as current sneak-paths, parasitic resistance, and capacitance of the metal lines, as well as excessively large read currents and diminishing yield limit the maximum size of crossbar arrays in practice [99–101].

These issues are also common to biological networks. As the resistance attenuates the spread of the action potential, cytoplasmic resistance sets an upper bound to the length of dendrites [30].

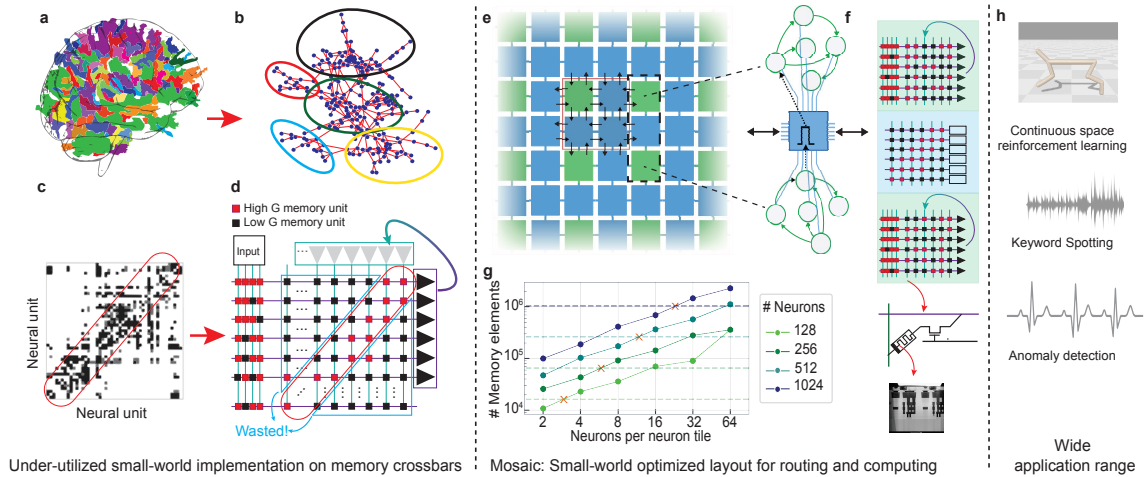


FIGURE 5.1: Small-world graphs in biological network and how to build that into a hardware architecture for edge applications. (a) Depiction of small-world property in the brain, with highly-clustered neighboring regions highlighted with the same color. (b) Network connectivity of the brain is a small-world graph, with highly clustered groups of neurons with sparse connectivity among them. (c) (adapted from Bullmore and Sporns 2009 [286]). The functional connectivity matrix which is derived from anatomical data with rows and columns representing neural units. The diagonal region of the matrix (darkest colors) contains the strongest connectivity which represents the connections between the neighboring regions. The off-diagonal elements are not connected. (d) Hardware implementation of the connectivity matrix of c, with neurons and synapses arranged in a crossbar architecture. The red squares represent the group of memory devices in the diagonal, connecting neighboring neurons. Black squares show the group of memory devices that are never programmed in a small-world network, and are thus highlighted as “wasted”. (e) The Mosaic architecture breaks the large crossbars into small densely-connected crossbars (green Neuron Tiles) and connects them through small routing crossbars (blue Routing Tiles). This gives rise to a distributed two-dimensional mesh, with highly connected clusters of neurons, connected to each other through routers. (f) The state of the resistive memory devices in Neuron Tiles determines how the information is processed, while the state of the routing devices determines how it is propagated in the mesh. The resistive memory devices are integrated into 130 nm technology. (g) Plot showing the required memory (number of memristors) as a function of the number of neurons per tile, for different total numbers of neurons in the network. The horizontal dashed line indicates the number of required memory bits using a fully-connected RRAM crossbar array. The cross (X) illustrates the cross-over point below which the Mosaic approach becomes favorable. (h) The Mosaic can be used for a variety of edge AI applications, benchmarked here on sensory processing and Reinforcement learning tasks.

Hence, the intrinsic physical structure of the nervous systems necessitates the use of local over global connectivity.

Drawing inspiration from the biological solution for the same problem leads to (i) a similar optimal silicon layout, a small-world graph, and (ii) a similar information transfer mechanism through electrical pulses, or spikes. A large crossbar can be divided into an array of smaller, more locally connected crossbars. These correspond to the green squares of Fig. 5.1e. Each green crossbar hosts a cluster of spiking neurons with a high degree of local connectivity. To pass information among these clusters, small routers can be placed between them - the blue tiles in Fig. 5.1e. We call this two-dimensional systolic matrix of distributed crossbars, or tiles, the neuromorphic Mosaic architecture. Each green tile serves as an analog computing core, which sends out information in the form of spikes, while each blue tile serves as a routing core that spreads the spikes throughout the mesh to other green tiles. Thus, the Mosaic takes advantage of distributed and de-centralized computing and routing to enable not only in-memory computing, but also in-memory routing (Fig. 5.1f). Though the Mosaic architecture is independent of the choice of memory technology, here we are taking advantage of the resistive memory, for its non-volatility, small footprint, low access time and power, and fast programming [300].

Neighborhood-based computing with resistive memory has been previously explored through using Cellular Neural Networks [301, 302], Self-organizing Maps (SOM) [303], and the crossnet architecture [304]. Though cellular architectures use local clustering, their lack of global connectivity limits both the speed of information propagation and their configurability. Therefore their application has been mostly limited to low-level image processing [305]. This also applies for SOMs, which exploit neighboring connectivity and are typically trained with unsupervised methods to visualize low-dimensional data [306]. Similarly, the crossnet architecture proposed to use distributed small tilted integrated crossbars on top of the CMOS substrate, to create local connectivity domains for image processing [304]. The tilted crossbars allow the nano-wire feature size to be independent of the CMOS technology node [307]. However, this approach requires extra post-processing lithographic steps in the fabrication process, which has so far limited its realization.

Unlike most previous approaches, the Mosaic supports both dense local connectivity, and globally sparse long-range connections, by introducing re-configurable routing crossbars between the computing tiles. This allows to flexibly program specific small-world network configurations and to compile them onto the Mosaic for solving the desired task. Moreover, the Mosaic is fully compatible with standard integrated RRAM/CMOS processes available at the foundries, without the need for extra post-processing steps. Specifically, we have designed the Mosaic for small-world SNNs, where the communication between the tiles is through electrical pulses, or spikes. In the realm of SNN hardware, the Mosaic goes beyond the AER [103, 308, 309], the standard spike-based communication scheme, by removing the need to store each neuron's connectivity information in either bulky local or centralized memory units which draw static power and can consume a large chip area (Supplementary Note 2).

In this Article, we first present the Mosaic architecture. We report electrical circuit measurements from computational and Routing Tiles that we designed and fabricated in 130 nm CMOS technology co-integrated with Hafnium dioxide-based RRAM devices. Then, calibrated on these measurements, and using a novel method for training small-world neural networks that exploits the intrinsic layout of the Mosaic, we run system-level simulations applied to a variety of edge computing tasks (Fig. 5.1h). Finally, we compare our approach to other neuromorphic hardware platforms which highlights the significant reduction in spike-routing energy, between one and four orders of magnitude.

5.2 MOSAIC HARDWARE COMPUTING AND ROUTING MEASUREMENTS

In the Mosaic (Fig. 5.1e), each of the tiles consists of a small memristor crossbar that can receive and transmit spikes to and from their neighboring tiles to the North (N), South (S), East (E) and West (W) directions (Supplementary Note 4). The memristive crossbar array in the green Neuron Tiles stores the synaptic weights of several LIF neurons. These neurons are implemented using

analog circuits and are located at the termination of each row, emitting voltage spikes at their outputs [29]. The spikes from the Neuron Tile are copied in four directions of N, S, E and W. These spikes are communicated between Neuron Tiles through a mesh of blue Routing Tiles, whose crossbar array stores the connectivity pattern between Neuron Tiles. The Routing Tiles at different directions decides whether or not the received spike should be further communicated. Together, the two tiles give rise to a continuous mosaic of neuromorphic computation and memory for realizing small-world SNNs.

Small-world topology can be obtained by randomly programming memristors in a computer model of the Mosaic (see Methods and Supplementary Note 3). The resulting graph exhibits an intriguing set of connection patterns that reflect those found in many of the small-world graphical motifs observed in animal nervous systems. For example, central ‘hub-like’ neurons with connections to numerous nodes, reciprocal connections between pairs of nodes reminiscent of winner-take-all mechanisms, and some heavily connected local neural clusters [285]. If desired, these graph properties could be adapted on the fly by re-programming the RRAM states in the two tile types. For example, a set of desired small-world graph properties can be achieved by randomly programming the RRAM devices into their HCS with a certain probability (Supplementary Note 3). Random programming can for example be achieved elegantly by simply modulating RRAM programming voltages [125].

For Mosaic-based small-world graphs, we estimate the required number of memory devices (synaptic weight and routing weight) as a function of the total number of neurons in a network, through a mathematical derivation (see Methods). Fig. 5.1g plots the memory footprint as a function of the number of neurons in each tile for different network sizes. Horizontal dashed lines show the number of memory elements using one large crossbar for each network size, as has previously been used for RNN implementations [310]. The cross-over points, at which the Mosaic memory footprint becomes favorable, are denoted with a cross. While for smaller network sizes (i.e. 128 neurons) no memory reduction is observed compared to a single large array, the memory saving becomes increasingly important as the network is scaled. For example, given a network of 1024 neurons and 4 neurons per Neuron Tile, the Mosaic requires almost one order of magnitude fewer memory devices than a single crossbar to implement an equivalent network model.

NEURON TILE CIRCUITS: SMALL-WORLDS Each Neuron Tile in the Mosaic (Fig. 5.2a) is composed of multiple rows, a circuit that models a LIF neuron and its synapses. The details of one neuron row is shown in Fig. 5.2b. It has N parallel one-transistor-one-resistor (1T1R) RRAM structures at its input. The synaptic weights of each neuron are stored in the conductance level of the RRAM devices in one row. On the arrival of any of the input events $V_{in< i >}$, the amplifier pins node V_x to V_{top} , and thus a read voltage equivalent to $V_{top} - V_{bot}$ is applied across G_i , giving rise to current i_{in} at M_1 , and in turn to i_{buff} . This current pulse is mirrored through I_w to the “synaptic dynamics” circuit, Differential Pair Integrator (DPI) [311], which low pass filters it through charging the capacitor M_9 in the presence of the pulse, and discharging it through current I_{tau} in its absence. The charge/discharge of M_9 generates an exponentially decaying current, I_{syn} , which is injected into the neuron’s membrane potential node, V_{mem} , and charges capacitor M_{13} . The capacitor leaks through M_{11} , whose rate is controlled by V_{lk} at its gate. As soon as the voltage developed on V_{mem} passes the threshold of the following inverter stage, it generates a pulse, at V_{out} . The refractory period time constant depends on the capacitor M_{16} and the bias on V_{rp} . (For a more detailed explanation of the circuit, please see Supplementary Note 5).

We have fabricated and measured the circuits of the Neuron Tile in a 130 nm CMOS technology integrated with RRAM devices [119]. The measurements were done on the wafer level, using a probe station shown in Fig. 5.2c. In the fabricated circuit, we statistically characterized the RRAMs through iterative programming [312] and controlling the programming current, resulting in nine stable conductance states, G , shown in Fig. 5.2d. After programming each device, we apply a pulse on $V_{in} < 0 >$ and measure the voltage on V_{syn} , which is the voltage developed on the M_9 capacitor. We repeat the experiment for four different conductance levels of $4 \mu S$, $48 \mu S$, $64 \mu S$ and $147 \mu S$. The resulting V_{syn} traces are plotted in Fig. 5.2e. V_{syn} starts from the initial value close to the power supply, 1.2 V. The amount of discharge depends on the I_w current which is a linear function of the conductance value of the RRAM, G . The higher the G , the higher the

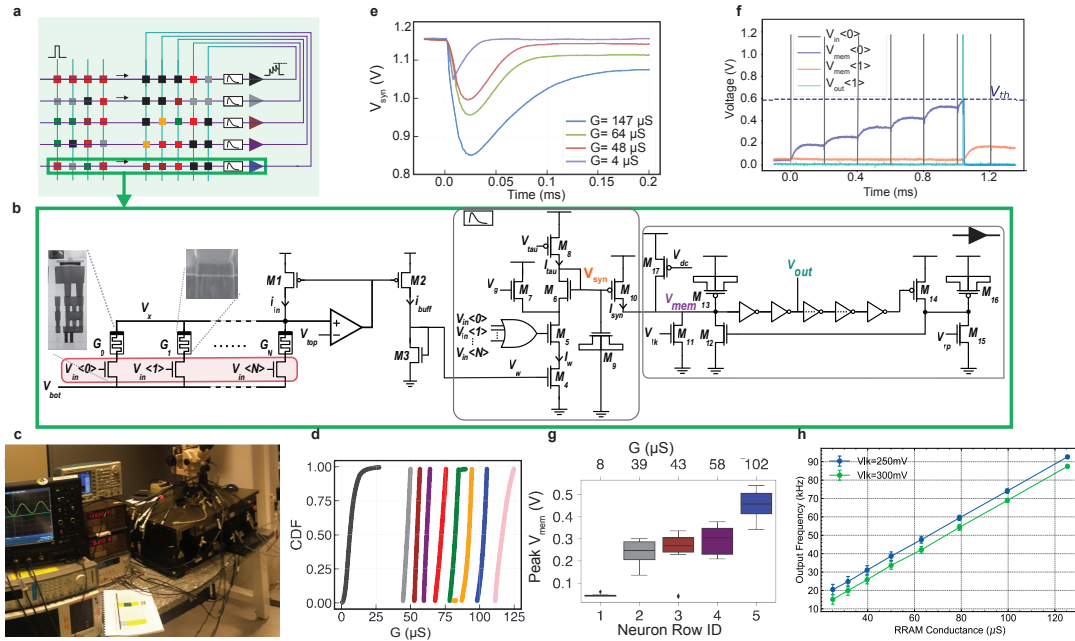


FIGURE 5.2: **Experimental results from the neuron column circuit.** (a) Neuron Tile, a crossbar with feed-forward and recurrent inputs displaying network parameters represented by colored squares. (b) Schematic of a single row of the fabricated crossbars, where RRAMs represent neuron weights. Insets show scanning and transmission electron microscopy images of the 1T1R stack with a hafnium-dioxide layer sandwiched between memristor electrodes. Upon input events $V_{in< i >}$, $V_{top} - V_{bot}$ is applied across G_i , yielding i_{in} and subsequently i_{buff} , which feeds into the synaptic dynamic block, producing exponentially decaying current i_{syn} with a time constant set by MOS capacitor M_9 and bias current I_{tau} . Integration of i_{syn} into neuron membrane potential V_{mem} triggers an output pulse (V_{out}) upon exceeding the inverter threshold. Refractory period regulation is achieved through MOS cap M_{16} and V_{rp} bias. (c) Wafer-level measurement setup utilizes an Arduino for logic circuitry management to program RRAMs and a B1500 Device Parameter Analyzer to read device conductance. (d) Cumulative distributions of RRAM conductance (G) resulting from iterative programming in a 4096-device RRAM array with varied SET programming currents. (e) V_{syn} initially at 1.2V decreases as capacitor M_9 discharges upon pulse arrival at time 0. Discharge magnitude depends on I_w set by G . Four conductance values' V_{syn} curves are recorded. (f) Input pulse train (gray pulses) at $V_{in< 0 >}$ increases zeroth neuron's V_{mem} (purple trace) until it fires (light blue trace) after six pulses, causing feedback influence on neuron 1's V_{mem} . (g) Statistical measurements on peak membrane potential in response to a pulse across a 5-neuron array over 10 cycles. (h) Neuron output frequency linearly correlates with G , with error bars reflecting variability across 4096 devices.

I_w , and higher the decrease in V_{syn} , resulting in higher I_{syn} which is integrated by the neuron membrane V_{mem} . The peak value of the membrane potential in response to a pulse is measured across one array of 5 neurons, each with a different conductance level (Fig. 5.2g). Each pulse increases the membrane potential according to the corresponding conductance level, and once it hits a threshold, it generates an output spike (Fig. 5.2f). The peak value of the neuron's membrane potential and thus its firing rate is proportional to the conductance G , as shown in Fig. 5.2h. The error bars on the plot show the variability of the devices in the 4 kb array. It is worth noting that this implementation does not take into account the negative weight, as the focus of the design has been on the concept. Negative weights could be implemented using a differential signaling approach, by using two RRAMs per synapse [115].

ROUTING TILE CIRCUITS: CONNECTING SMALL-WORLDS A Routing Tile circuit is shown in Fig. 5.3a. It acts as a flexible means of configuring how spikes emitted from Neuron Tiles propagate locally between small-worlds. Thus, the routed message entails a spike, which is either

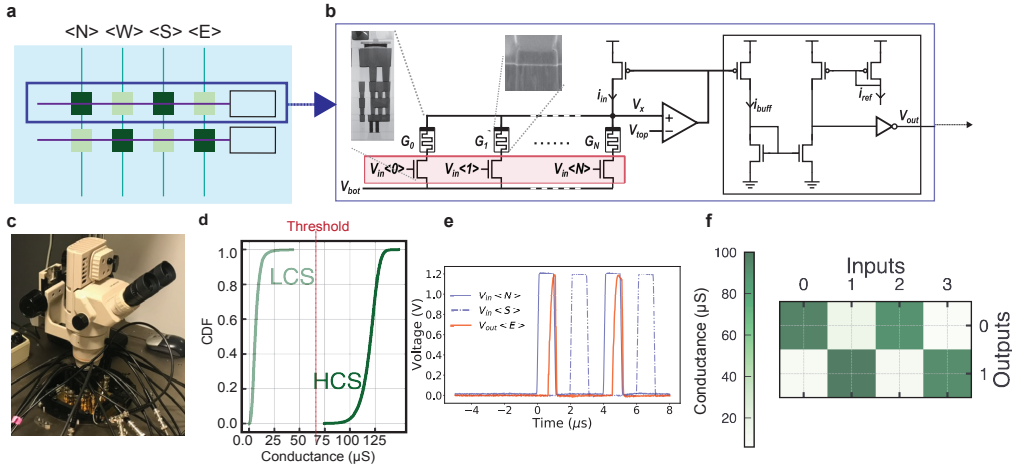


FIGURE 5.3: **Experimental measurements of the fabricated Routing Tile circuits.** (a) The Routing Tile, a crossbar whose memory state steers the input spikes from different directions towards the destination. (b) Detailed schematic of one row of the fabricated routing circuits. On the arrival of a spike to any of the input ports of the Routing Tile, $V_{in} < i >$, a current proportional to G_i flows in i_{in} , similar to the Neuron Tile. A current comparator compares this current against a reference current, I_{ref} , which is a bias current generated on chip through providing a DC voltage from the I/O pads to the gate of an on-chip transistor. If $i_{in} > i_{ref}$, the spike will get regenerated, thus “pass”, or is “blocked” otherwise. (c) Wafer-level measurements of the test circuits through the probe station test setup. (d) Measurements from 4 kb array shows the Cumulative Distribution Function (CDF) of the RRAM in its High Conductive State (HCS) and Low Conductive State (LCS). The line between the distributions that separates the two is considered as the “Threshold” conductance, which the decision boundary for passing or blocking the spikes. Based on this Threshold value, the I_{ref} bias in panel (b) is determined. (e) Experimental results from the Routing Tile, with continuous and dashed blue traces showing the waveforms applied to the <N> and <S> inputs, while the orange trace shows the response of the output towards the <E> port. The <E> output port follows the <N> input, resulting from the device programmed into the HCS, while the input from the <S> port gets blocked as the corresponding RRAM device is in its LCS. (f) A binary checker-board pattern is programmed into the routing array, to show a ratio of 10 between the High Resistive and Low Resistive state, which sets a perfect boundary for a binary decision required for the Routing Tile.

blocked by the router, if the corresponding RRAM is in its HRS, or is passed otherwise. The functional principles of the Routing Tile circuits are similar to the Neuron Tiles. The principal difference is the replacement of the synapse and neuron circuit models with a simple current comparator circuit (highlighted with a black box in Fig. 5.3b). The measurements were done on the wafer level, using a probe station shown in Fig. 5.3c. On the arrival of a spike on an input port of the Routing Tile, $V_{in} < i >$, $0 < i < N$, a current proportional to G_i flows to the device, giving rise to read current i_{buff} . A current comparator compares i_{buff} against i_{ref} , which is a bias generated on chip by providing a voltage from the I/O pad to the gate of a transistor (not shown in the Fig.). The I_{ref} value is decided based on the “Threshold” conductance boundary in Fig. 5.3d. The Routing Tile regenerates a spike if the resulting i_{buff} is higher than i_{ref} , and blocks it otherwise, since the output remains at zero. Therefore, the state of the device serves to either pass or block input spikes arriving from different input ports (N, S, W, E), sending them to its output ports (Supplementary Note 4). Since the routing array acts as a binary pass or no-pass, the decision boundary is on whether the devices is in its HCS or LCS, as shown in Fig. 5.3d [313]. Using a fabricated Routing Tile circuit, we demonstrate its functionality experimentally in Fig. 5.3e. Continuous and dashed blue traces show the waveforms applied to the <N> and <S> inputs of the tile respectively, while the orange trace shows the response of the output towards the E port. The E output port follows the N input resulting from the corresponding RRAM programmed into its HCS, while the input from the S port gets blocked as the corresponding RRAM device is in its LCS, and thus the output remains at zero. This output pulse propagates onward to the next tile.

Note that in Fig. 5.3d the output spike does not appear as rectangular due to the large capacitive load of the probe station (see Methods). To allow for greater reconfigurability, more channels per direction can be used in the Routing Tiles (see Supplementary Note 6).

5.3 ANALOG HARDWARE-AWARE SIMULATIONS

Application to real-time sensory-motor processing through hardware-aware simulations

The Mosaic is a programmable hardware well suited for the application of pre-trained small-world RSNN in energy and memory-constrained applications at the edge. Through hardware-aware simulations, we assess the suitability of the Mosaic on a series of representative sensory processing tasks, including anomaly detection in heartbeat (application in wearable devices), keyword spotting (application in voice command), and motor system control (application in robotics) tasks (Fig. 5.4 a,b,c respectively). We apply these tasks to three network cases, (i) a non-constrained RSNN with full-bit precision weights (32 bit Floating Point (FP32)) (Fig. 5.4 d), (ii) Mosaic constrained connectivity with FP32 weights (Fig. 5.4 e), and (iii) Mosaic constrained connectivity with noisy and quantized RRAM weights (Fig. 5.4 f). Therefore, case (iii) is fully hardware-aware, including the architecture choices (e.g., number of neurons per Neuron Tile), connectivity constraints, noise and quantization of weights.

For training case *i*, we use BPTT [314] with surrogate gradient approximations of the derivative of a LIF neuron activation function on a vanilla RSNN [165] (see Methods). For training case (ii), we introduce a Mosaic-regularized cost function during the training, which leads to a learned weight matrix with small-world connectivity that is mappable onto the Mosaic (see Methods). For case (iii), we quantize the weights using a mixed hardware-software experimental methodology whereby memory elements in a Mosaic software model are assigned conductance values programmed into a corresponding memristor in a fabricated array. Programmed conductances are obtained through a closed-loop programming strategy [312, 315–317].

For all the networks and tasks, the input is fed as a spike train and the output class is identified as the neuron with the highest firing rate. The RSNN of case (i) includes a standard input layer, recurrent layer, and output layer. In the Mosaic cases (ii) and (iii), the inputs are directly fed into the Mosaic Neuron Tiles from the top left, are processed in the small-world RSNN, and the resulting output is taken directly from the opposing side of the Mosaic, by assigning some of the Neuron Tiles in the Mosaic as output neurons. As the inputs and outputs are part of the Mosaic fabric, this scheme avoids the need for explicit input and output readout layers, relative to the RSNN, that may greatly simplify a practical implementation.

EKG ANOMALY DETECTION We first benchmark our approach on a binary classification task in detecting anomalies in the Electrocardiogram (ECG) recordings of the MIT-BIH Arrhythmia Database [318]. In order for the data to be compatible with the RSNN, we first encode the continuous ECG time-series into trains of spikes using a delta-modulation technique, which describes the relative changes in signal magnitude [319, 320] (see Methods). An example heartbeat and its spike encoding are plotted in Fig. 5.4a.

The accuracy over the test set for five iterations of training, transfer, and test for cases (i) (red), (ii) (green) and (iii) (blue) is plotted in Fig. 5.4g using a boxplot. Although the Mosaic constrains the connectivity to follow a small-world pattern, the median accuracy of case (ii) only drops by 3% compared to the non-constrained RSNN of case (i). Introducing the quantization and noise of the RRAM devices in case (iii), drops the median accuracy further by another 2%, resulting in a median accuracy of 92.4%. As often reported, the variation in the accuracy of case *iii* also increases due to the cycle-to-cycle variability of RRAM devices [317].

KEYWORD SPOTTING (KWS) We then benchmarked our approach on a 20-class speech task using the Spiking Heidelberg Digits (SHD) [206] dataset. SHD includes the spoken digits between zero and nine in English and German uttered by 12 speakers. In this dataset, the speech signals have been encoded into spikes using a biologically-inspired cochlea model which effectively

computes a spectrogram with Mel-spaced filter banks, and convert them into instantaneous firing rates [206].

The accuracy over the test set for five iterations of training, transfer, and test for cases (i) (red), (ii) (green) and (iii) (blue) is plotted in Fig. 5.4h using a boxplot. The dashed red box is taken directly from the SHD paper [206]. The Mosaic connectivity constraints have only an effect of about 2.5% drop in accuracy, and a further drop of 1% when introducing RRAM quantization and noise constraints. Furthermore, we experimented with various numbers of Neuron Tiles and the number of neurons within each Neuron Tile (Supplementary Note 8, Fig. S10), as well as sparsity constraints (Supplementary Note 8, Fig. S11) as hyperparameters. We found that optimal performance can be achieved when an adequate amount of neural resources are allocated for the task.

MOTOR CONTROL BY REINFORCEMENT LEARNING Finally, we also benchmark the Mosaic in a motor system control RL task, i.e., the Half-cheetah [321]. RL has applications ranging from active sensing via camera control [322] to dexterous robot locomotion [323].

To train the network weights, we employ the evolutionary strategies (ES) from Salimans et al. [113] in reinforcement learning settings [324–326]. ES enables stochastic perturbation of the network parameters, evaluation of the population fitness on the task and updating the parameters using stochastic gradient estimate, in a scalable way for RL.

Fig. 5.4i shows the maximum gained reward for five runs in cases i, ii, and iii, which indicates that the network learns an effective policy for forward running. Unlike tasks a and b, the network connectivity constraints and parameter quantization have relatively little impact.

Encouragingly, across three highly distinct tasks, performance was only slightly impacted when passing from an unconstrained neural network topology to a noisy small-world neural network. In particular, for the half-cheetah RL task, this had no impact.

5.4 BENCHMARKING ROUTING ENERGY IN NEUROMORPHIC PLATFORMS

In-memory computing greatly reduces the energy consumption inherent to data movement in Von Neumann architectures. Although crossbars bring memory and computing together, when neural networks are scaled up, neuromorphic hardware will require an array of distributed crossbars (or cores) when faced with physical constraints, such as IR drop and capacitive charging [101]. Small-world networks may naturally permit the minimization of communication between these crossbars, but a certain energy and latency cost associated with the data movement will remain, since the compilation of the small-world network on a general-purpose routing architecture is not ideal. Hardware that is specifically designed for small-world networks will ideally minimize these energy and latency costs (Fig. 5.1 g). In order to understand how the spike routing efficiency of the Mosaic compares to other SNN hardware platforms, optimized for other metrics such as maximizing connectivity, we compare the energy and latency of (i) routing one spike within a core (0-hop), (ii) routing one spike to the neighboring core (1-hop) and (iii) the total routing power consumption required for tasks A and B, i.e., heartbeat anomaly detection and spoken digit classification respectively (Fig. 5.4a,b).

The results are presented in Table 5.1. We report the energy and latency figures, both in the original technology where the systems are designed, and scaled values to the 130 nm technology, where Mosaic circuits are designed, using general scaling laws [327]. The routing power estimates for Tasks A and B are obtained by evaluating the 0- and 1-hop routing energy and the number of spikes required to solve the tasks, neglecting any other circuit overheads. In particular, the optimization of the sparsity of connections between neurons implemented to train Mosaic assures that 95% of the spikes are routed with 0-hops operations, while about 4% of the spikes are routed via 1-hop operations. The remaining spikes require k-hops to reach the destination Neuron Tile. The Routing energy consumption for Tasks A and B is estimated accounting for the total spike count and the routing hop partition.

The scaled energy figures show that although the Mosaic’s design has not been optimized for energy efficiency, the 0- and 1-hop routing energy is reduced relative to other approaches,

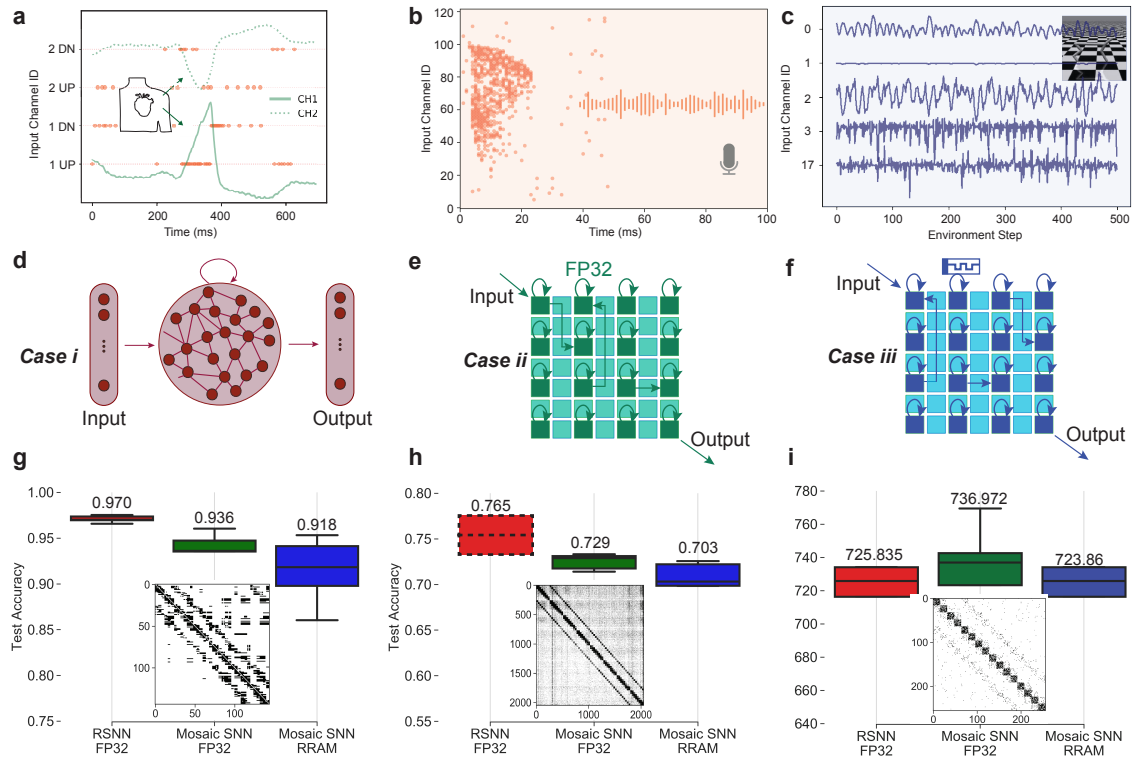


FIGURE 5.4: **Benchmarking the Mosaic against three edge tasks, heartbeat (ECG) arrhythmia detection, keyword spotting (KWS), and motor control by reinforcement learning (RL).** (a,b,c) A depiction of the three tasks, along with the corresponding input presented to the Mosaic. (a) ECG task, where each of the two-channel waveforms is encoded into up (UP) and down (DN) spiking channels, representing the signal derivative direction. (b) KWS task with the spikes representing the density of information in different input (frequency) channels. (c) half-cheetah RL task with input channels representing state space, consisting of positional values of different body parts of the cheetah, followed by the velocities of those individual parts. (d, e, f) Depiction of the three network cases applied to each task. (d) Case (*i*) involves a non-constrained Recurrent Spiking Neural Network (RSNN) with full-bit precision weights (FP32), encompassing an input layer, a recurrent layer, and an output layer. (e) Case (*ii*) represents Mosaic-constrained connectivity with FP32 weights, omitting explicit input and output layers. Input directly enters the Mosaic, and output is extracted directly from it. Circular arrows denote local recurrent connections, while straight arrows signify sparse global connections between cores. (f) Case (*iii*) is similar to case (*ii*), but with noisy and quantized RRAM weights. (g, h, i) A comparison of task accuracy among the three cases: case (*i*) (red, leftmost box), case (*ii*) (green, middle box), and case (*iii*) (blue, right box). Boxplots display accuracy/maximum reward across five iterations, with boxes spanning upper and lower quartiles while whiskers extend to maximum and minimum values. Median accuracy is represented by a solid horizontal line, and the corresponding values are indicated on top of each box. The dashed red box for the KWS task with FP32 RSNN network is included from Cramer et al., 2020 [206] with 1024 neurons for comparison (with mean value indicated). This comparison reveals that the decline in accuracy due to Mosaic connectivity and further due to RRAM weights is negligible across all tasks. The inset figures depict the resulting Mosaic connectivity after training, which follows a small-world graphical structure.

even if we compare with digital approaches in more advanced technology nodes. This efficiency can be attributed to the Mosaic's in-memory routing approach resulting in low-energy routing memory access which is distributed in space. This reduces (i) the size of each router, and thus energy, compared to larger centralized routers employed in some platforms, and (ii) it avoids the use of CAMs, which consumes the majority of routing energy in some other spike-based routing mechanisms (Supplementary Note 2).

Neuromorphic platforms have each been designed to optimize different objectives [328], and the reason behind the energy efficiency of Mosaic in communication lies behind its explicit optimization for this very metric, thanks to its small-world connectivity layout. Despite this, as was shown in Fig. 5.4, the Mosaic does not suffer from a considerable drop in accuracy, at least for problem sizes of the sensory processing applications on the edge. This implies that for these problems, large connectivity between the cores is not required, which can be exploited for reducing the energy.

The Mosaic’s latency figure per router is comparable to the average latency of other platforms. Often, and in particular, for neural networks with sparse firing activity, this is a negligible factor. In applications requiring sensory processing of real-world slow-changing signals, the time constants dictating how quickly the model state evolves will be determined by the size of the V_{lk} in Fig. 5.2, typically on the order of tens or hundreds of milliseconds. Although, the routing latency grows linearly with the number of hops in the networks, as shown in the final connectivity matrices of Fig. 5.4g,h,i, the number of non-local connections decays down exponentially. Therefore, the latency of routing is always much less than the the time scale of the real-world signals on the edge, which is our target application.

The two final rows of Table 5.1 indicates the power consumption of the neuromorphic platforms in tasks A and B respectively. All the platforms are assumed to use a core (i.e., neuron tile) size of 32 neurons, and to have an N-hop energy cost equal to N times the 1-hop value. The potential of the Mosaic is clearly demonstrated, whereby a power consumption of only a few hundreds of pico Watts is required, relative to a few nano/microwatts in the other neuromorphic platforms.

5.5 DISCUSSION

We have identified small-world graphs as a favorable topology for efficient routing, have proposed a hardware architecture that efficiently implements it, designed and fabricated memristor-based building blocks for the architecture in 130 nm technology, and report measurements and comparison to other approaches. We empirically quantified the impact of both the small-world neural network topology and low memristor precision on three diverse and challenging tasks representative of edge-AI settings. We also introduced an adapted machine learning strategy that enforces small-worldness and accounted for the low-precision of noisy RRAM devices. The results achieved across these tasks were comparable to those achieved by floating point precision models with unconstrained network connectivity.

Although the connectivity of the Mosaic is sparse, it still requires more number of routing nodes than computing nodes. However, the Routing Tiles are more compact than the neuron tiles, as they only perform binary classification. This means that the read-out circuitry does not require a large Signal to Noise Ratio (SNR), compared to the neuron tiles. This loosened requirement reduces the overhead of the Routing Tiles readout in terms of both area and power (Supplementary Note 9).

In this work, we have treated Mosaic as a standard RSNN, and trained it with BPTT using the surrogate gradient approximation, and simply added the loss terms that punish the network’s dense connectivity to shape sparse graphs. Therefore, the potential computational advantages of small-world architectures do not necessarily emerge, and the performance of the network is mainly related to its number of parameters. In fact, we found that Mosaic requires more neurons, but about the same number of parameters, for the same accuracy as that of an RSNN on the same task. This confirms that taking advantage of small-world connectivity requires a novel training procedure, which we hope to develop in the future. Moreover, in this paper, we have benchmarked the Mosaic on sensory processing tasks and have proposed to take advantage of the small-worldness for energy savings thanks to the locality of information processing. However, from a computational perspective, these tasks do not necessarily take advantage of the small-worldness. In future works, one can foresee tasks that can exploit the small-world connectivity from a computational standpoint.

Mosaic favors local processing of input data, in contrast with conventional deep learning algorithms such as Convolutional and Recurrent Neural Networks. However, novel approaches in

Neuromorphic Chip	TrueNorth [329]	SpiNNaker [330]	Neurogrid [331]	Dynap-SE [103]	Loihi [89]	Mosaic
Technology	28 nm (0.775 V)	130 nm (1.2 V)	180 nm (3 V)	180 nm (1.8 V)	14 nm (0.75 V)	130 nm (1.2 V)
Routing	on-chip	on-chip	on/off-chip	on-chip	on-chip	on-chip
o-hop* energy	26 pJ	30.3 nJ	1 nJ	30 pJ	23.6 pJ	400 fJ [◦]
sct.**. 130 nm	62.4 pJ	30.3 nJ	160 pJ	13.4 pJ	60.416 pJ	400 fJ
1-hop [◊] energy	2.3 pJ	1.11 nJ	14 nJ	17 pJ (@1.3 V)	3.5 pJ	1.6 pJ [◊]
sct. 130 nm	5.52 pJ	1.11 nJ	8.35 nJ	17 pJ	10.24 pJ	1.6 pJ [◊]
1-hop latency	6.25 ns	200 ps	20 ns	40 ns	6.5 ns	25 ns
sct. 130 nm	29 ns	200 ps	14.4 ns	28.88 ns	60.35 ns	25 ns
Optimized for Small-Worldness	No	No	No	Yes	No	Yes
Routing Power for task A	8.47 nW	9.85 μ W	563.31 nW	10.02 nW	7.71 nW	809 pW [◊]
Routing Power for task B	272.82 nW	317.08 μ W	18.14 μ W	322.7 nW	248.41 nW	5.06 nW [◊]

[◊] Assuming an average resistance value of 10 k Ω , and a read pulse 10 ns width.

* The same as energy per Synaptic Operation (SOP), numbers are taken from Basu, et al, 2022 [332]

** sct. = Scaled to

[◊] = Numbers are taken from Moradi, et al, 2018 [103]

TABLE 5.1: Comparison of spike-routing performance across neuromorphic platforms

deep learning, e.g., Vision Transformers with Local Attention [333] and MLP-mixers [334], treat input data in a similar way as the Mosaic, subdividing the input dimensions, and processing the resulting patches locally. This is also similar to how most biological system processes information in a local fashion, such as the visual system of fruit flies [335].

In the broader context, graph-based computing is currently receiving attention as a promising means of leveraging the capabilities of SNNs [336–338]. The Mosaic is thus a timely dedicated hardware architecture optimized for a specific type of graph that is abundant in nature and in the real-world and that promises to find application at the extreme-edge.

5.6 METHODS

Design, fabrication of Mosaic circuits

5.6.0.1 *Neuron and routing column circuits*

Both neuron and routing column share the common front-end circuit which reads the conductances of the RRAM devices. The RRAM bottom electrode has a constant DC voltage V_{bot} applied to it and the common top electrode is pinned to the voltage V_x by a rail-to-rail operational amplifier (OPAMP) circuit. The OPAMP output is connected in negative feedback to its non-inverting input (due to the 180 degrees phase-shift between the gate and drain of transistor M_1 in Fig. 5.2) and has the constant DC bias voltage V_{top} applied to its inverting input. As a result, the output of the OPAMP will modulate the gate voltage of transistor M_1 such that the current it sources onto the node V_x will maintain its voltage as close as possible to the DC bias V_{top} . Whenever an input pulse $V_{in} < n >$ arrives, a current i_{in} equal to $(V_x - V_{bot})G_n$ will flow out of the bottom electrode. The negative feedback of the OPAMP will then act to ensure that $V_x = V_{top}$, by sourcing an equal current from transistor M_1 . By connecting the OPAMP output to the gate of transistor M_2 , a current equal to i_{in} , will therefore also be buffered, as i_{buff} , into the branch composed of transistors M_2 and M_3 in series. In the Routing Tile, this current is compared against a reference current, and if higher, a pulse is generated and transferred onwards. The current comparator circuit is composed of two current mirrors and an inverter (Fig. 5.3b). In the neuron column, this current is injected into a CMOS differential-pair integrator synapse circuit model [188] which generates an exponentially decaying waveform from the onset of the pulse with an amplitude proportional to the injected current. Finally, this exponential current is injected onto the membrane capacitor of a CMOS leaky-integrate and fire neuron circuit model [339] where it integrates as a voltage (see Fig. 5.2b). Upon exceeding a voltage threshold (the switching voltage of an inverter) a pulse is emitted at the output of the circuit. This pulse in turn feeds back and shunts the capacitor to ground such that it is discharged. Further circuits were required in order to program the device conductance states. Notably, multiplexers were integrated on each end of the column in order to be able to apply voltages to the top and bottom electrodes of the RRAM devices.

A critical parameter in both Neuron and Routing Tiles is the spike's pulse width. Minimizing the width of spikes assures maximal energy efficiency, but that comes at a cost. If the duration of the voltage pulse is too low, the readout current from the 1T1R will be imprecise, and parasitic effects due to the metal lines in the array might even impede the correct propagation of either the voltage pulse or the readout current. For this reason, we thoroughly investigated the minimal pulse-width that allows spikes and readout currents to be reliably propagated, at a probability of 99.7% (3σ). Extensive Monte Carlo simulation resulted in a spike pulse width of around 100 ns. Based on these SPICE simulations, we also estimated the energy consumption of Mosaic for the different tasks presented in Figure 5.4.

Fabrication/integration

The circuits described in the Results section have been taped-out in 130 nm technology at CEA-Leti, in a 200 mm production line. The Front End of the Line, below metal layer 4, has been realized by ST-Microelectronics, while from the fifth metal layer upwards, including the deposition of the composites for RRAM devices, the process has been completed by CEA-Leti. RRAM devices are

composed of a 5 nm thick HfO_2 layer sandwiched by two 5 nm thick TiN electrodes, forming a $TiN/HfO_2/Ti/TiN$ stack. Each device is accessed by a transistor giving rise to the $1T1R$ unit cell. The size of the access transistor is 650 nm wide. $1T1R$ cells are integrated with CMOS-based circuits by stacking the RRAM cells on the higher metal layers. In the cases of the neuron and Routing Tiles, $1T1R$ cells are organized in a small - either 2×2 or 2×4 - matrix in which the bottom electrodes are shared between devices in the same column and the gates shared with devices in the same row. Multiplexers operated by simple logic circuits enable to select either a single device or a row of devices for programming or reading operations. The circuits integrated into the wafer, were accessed by a probe card which connected to the pads of the dimension of $[50 \times 90] \mu m^2$.

RRAM characteristics

Resistive switching in the devices used in our paper are based on the formation and rupture of a filament as a result of the presence of an electric field that is applied across the device. The change in the geometry of the filament results in different resistive state in the device. A SET/RESET operation is performed by applying a positive/negative pulse across the device which forms/disrupts a conductive filament in the memory cell, thus decreasing/increasing its resistance. When the filament is formed, the cell is in the HCS, otherwise the cell is in the LCS. For a SET operation, the bottom of the $1T1R$ structure is conventionally left at ground level, and a positive voltage is applied to the $1T1R$ top electrode. The reverse is applied in the RESET operation. Typical values for the SET operation are V_{gate} in $[0.9 - 1.3] V$, while the V_{top} peak voltage is normally at 2.0 V. For the RESET operation, the gate voltage is instead in the $[2.75, 3.25] V$ range, while the bottom electrode is reaching a peak at 3.0 V. The reading operation is performed by limiting the V_{top} voltage to 0.3 V, a value that avoids read disturbances, while opening the gate voltage at 4.5 V.

Mosaic circuit measurement setups

The tests involved analyzing and recording the dynamical behavior of analog CMOS circuits as well as programming and reading RRAM devices. Both phases required dedicated instrumentation, all simultaneously connected to the probe card. For programming and reading the RRAM devices, Source Measure Units (SMU)s from a Keithley 4200 SCS machine were used. To maximize stability and precision of the programming operation, SET and RESET are performed in a quasi-static manner. This means that a slow rising and falling voltage input is applied to either the Top (SET) or Bottom (RESET) electrode, while the gate is kept at a fixed value. To the $V_{top}(t)$, $V_{bot}(t)$ voltages, we applied a triangular pulse with rising and falling times of 1 sec and picked a value for V_{gate} . For a SET operation, the bottom of the $1T1R$ structure is conventionally left at ground level, while in the RESET case the V_{top} is equal to 0 V and a positive voltage is applied to V_{bot} . Typical values for the SET operation are V_{gate} in $[0.9 - 1.3] V$, while the V_{top} peak voltage is normally at 2.0 V. Such values allow to modulate the RRAM resistance in an interval of $[5 - 30] k\Omega$ corresponding to the HCS of the device. For the RESET operation, the gate voltage is instead in the $[2.75, 3.25] V$ range, while the bottom electrode is reaching a peak at 3.0 V.

The LCS is less controllable than the HCS due to the inherent stochasticity related to the rupture of the conductive filament, thus the HRS level is spread out in a wider $[80 - 1000] k\Omega$ interval. The reading operation is performed by limiting the V_{top} voltage to 0.3 V, a value that avoids read disturbances, while opening the gate voltage at 4.5 V.

Inputs and outputs are analog dynamical signals. In the case of the input, we have alternated two HP 8110 pulse generators with a Tektronix AFG3011 waveform generator. As a general rule, input pulses had a pulse width of $1 \mu s$ and rise/fall time of 50 ns. This type of pulse is assumed as the stereotypical spiking event of a Spiking Neural Network. Concerning the outputs, a 1 GHz Teledyne LeCroy oscilloscope was utilized to record the output signals.

Mosaic layout-aware training via regularizing the loss function

We introduce a new regularization function, L_M , that emphasizes the realization cost of short and long-range connections in the Mosaic layout. Assuming the Neuron Tiles are placed in a square layout, L_M calculates a matrix $H \in \mathbb{R}^{j \times i}$, expressing the minimum number of Routing Tiles used to connect a source neuron N_j to target neuron N_i , based on their Neuron Tile positions on Mosaic. Following this, a static mask $S \in \mathbb{R}^{j \times i}$ is created to exponentially penalize the long-range connections such that $S = e^{\beta H} - 1$, where β is a positive number that controls the degree of penalization for connection distance. Finally, we calculate the $L_M = \sum S \odot W^2$, for the recurrent weight matrix $W \in \mathbb{R}^{j \times i}$. Note that the weights corresponding to intra-Neuron Tile connections (where $H = 0$) are not penalized, allowing the neurons within a Neuron Tile to be densely connected. During the training, task-related cross-entropy loss term (total reward in case of RL) increases the network performance, while L_M term reduces the strength of the neural network weights creating long-range connections in Mosaic layout. Starting from the 10th epoch, we deterministically prune connections (replacing the value of corresponding weight matrix elements to 0) when their L_1 -norm is smaller than a fixed threshold value of 0.005. This pruning procedure privileges local connections (i.e., those within a Neuron Tile or to a nearby Neuron Tile) and naturally gives rise to a small-world neural network topology. Our experiments found that gradient norm clipping during the training and reducing the learning rate by a factor of ten after 135th epoch in classification tasks help stabilize the optimization against the detrimental effects of pruning.

RRAM-aware noise-resilient training

The strategy of choice for endowing Mosaic with the ability to solve real-world tasks is offline training. This procedure consists of producing an abstraction of the Mosaic architecture on a server computer, formalized as a Spiking Neural Network that is trained to solve a particular task. When the parameters of Mosaic are optimized, in a digital floating-point-32-bits (FP32) representation, they are to be transferred to the physical Mosaic chip. However, the parameters in Mosaic are constituted by RRAM devices, which are not as precise as the FP32 counterparts. Furthermore, RRAMs suffer from other types of non-idealities such as programming stochasticity, temporal conductance relaxation, and read noise [312, 315–317].

To mitigate these detrimental effects at the weight transfer stage, we adapted the noise-resilient training method for RRAM devices [18, 340]. Similar to quantization-aware training, at every forward pass, the original network weights are altered via additive noise (quantized) using a straight-through estimator. We used a Gaussian noise with zero mean and standard deviation equal to 5% of the maximum conductance to emulate transfer non-idealities. The profile of this additive noise is based on our RRAM characterization of an array of 4096 RRAM devices [312], which are programmed with a program-and-verify scheme (up to 10 iterations) to various conductance levels then measured after 60 seconds for modeling the resulting distribution.

ECG task description

The Mosaic hardware-aware training procedure is tested on a electrocardiogram arrhythmia detection task. The ECG dataset was downloaded from the MIT-BIH arrhythmia repository [318]. The database is composed of continuous 30-minute recordings measured from multiple subjects. The QRS complex of each heartbeat has been annotated as either healthy or exhibiting one of many possible heart arrhythmias by a team of cardiologists. We selected one patient exhibiting approximately half healthy and half arrhythmic heartbeats. Each heartbeat was isolated from the others in a 700 ms time-series centered on the labelled QRS complex. Each of the two 700 ms channel signals were then converted to spikes using a delta modulation scheme [341]. This consists of recording the initial value of the time-series and, going forward in time, recording the time-stamp when this signal changes by a pre-determined positive or negative amount. The value of the signal at this time-stamp is then recorded and used in the next comparison forward

in time. This process is then repeated. For each of the two channels this results in four respective event streams - denoting upwards and downwards changes in the signals. During the simulation of the neural network, these four event streams corresponded to the four input neurons to the spiking recurrent neural network implemented by the Mosaic.

Data points were presented to the model in mini-batches of 16. Two populations of neurons in two Neuron Tiles were used to denote whether the presented ECG signals corresponded to a healthy or an arrhythmic heartbeat. The softmax of the total number of spikes generated by the neurons in each population was used to obtain a classification probability. The negative log-likelihood was then minimized using the categorical cross-entropy with the labels of the signals.

Keyword Spotting task description

For keyword spotting task, we used SHD dataset (20 classes, 8156 training, 2264 test samples). Each input example drawn from the dataset is sampled three times along the channel dimension without overlap to obtain three augmentations of the same data with 256 channels each. The advantage of this method is that it allows feeding the input stream to fewer Neuron Tiles by reducing the input dimension and also triples the sizes of both training and testing datasets.

We set the simulation time step to 1 ms in our simulations. The recurrent neural network architecture consists of 2048 LIF neurons with 45 ms membrane time constant. The neurons are distributed into 8x8 Neuron Tiles with 32 neurons each. The input spikes are fed only into the neurons of the Mosaic layout’s first row (8 tiles). The network prediction is determined after presenting each speech data for 100 ms by counting the total number of spikes from 20 neurons (total number of classes) in 2 output Neuron Tiles located in the bottom-right of the Mosaic layout. The neurons inside input and output Neuron Tiles are not recurrently connected. The network is trained using BPTT on the loss $L = L_{CE} + \lambda L_M$, where L_{CE} is the cross-entropy loss between input logits and target and L_M is the Mosaic-layout aware regularization term. We use batch size of 512 and suitably tuned hyperparameters.

Reinforcement Learning task description

In the RL experiments, we test the versatility of a Mosaic-optimized RSNN on a continuous action space motor-control task, half-cheetah, implemented using the BRAX physics engine for rigid body simulations [342]. At every timestep t , environment provides an input observation vector $o^t \in \mathbb{R}^{25}$ and a scalar reward value r^t . The goal of the agent is to maximize the expected sum of total rewards $R = \sum_{t=0}^{1000} r^t$ over an episode of 1000 environment interactions by selecting action $a^t \in \mathbb{R}^7$ calculated by the output of the policy network. The policy network of our agent consists of 256 recurrently connected LIF neurons, with a membrane decay time constant of 30 ms. The neuron placement is equally distributed into 16 Neuron Tiles to form a 7x7 Mosaic layout. We note that for simulation purposes, selecting a small network of 16 Neuron Tiles with 16 neurons each, while not optimal in terms of memory footprint (Eq. 5.2), was preferred to fit the large ES population within the constraints of single GPU memory capacities. At each time step, the observation vector o^t is accumulated into the membrane voltages of the first 25 neurons of two upper left input tiles. Furthermore, action vector a^t is calculated by reading the membrane voltages of the last seven neurons in the bottom right corner after passing \tanh non-linearity.

We considered Evolutionary Strategies (ES) as an optimization method to adjust the RSNN weights such that after the training, the agent can successfully solve the environment with a policy network with only locally dense and globally sparse connectivity. We found ES particularly promising approach for hardware-aware training as (i) it is blind to non-differentiable hardware constraints e.g., spiking function, quantized weights, connectivity patterns, and (ii) highly parallelizable since ES does not require spiking variable to be stored for thousand time steps compared to BPTT that explicitly calculates the gradient. In ES, the fitness function of an offspring is defined as the combination of total reward over an episode, R and realization cost of short and long-range connections L_M (same as KWS task), such that $F = R - \lambda L_M$. We used the population

size of 4096 (with antithetic sampling to reduce variance) and mutation noise standard deviation of 0.05. At the end of each generation, the network weights with L_0 -norm smaller than a fixed threshold are deterministically pruned. The agent is trained for 1000 generations.

Calculation of memory footprint

We calculate the Mosaic architecture's Memory Footprint (MF) in comparison to a large crossbar array, in building small-world graphical models.

To evaluate the MF for one large crossbar array, the total number of devices required to implement any possible connections between neurons can be counted - allowing for any RSNN to be mapped onto the system. Setting N to be the number of neurons in the system, the total possible number of connections in the graph is $MF_{ref} = N^2$.

For the Mosaic architecture, the number of RRAM cells (i.e., the MF) is equal to the number of devices in all the Neuron Tiles and Routing Tiles: $MF_{mosaic} = MF_{NeuronTiles} + MF_{RoutingTiles}$.

Considering each Neuron Tile with k neurons, each Neuron Tile contributes to $5k^2$ devices (where the factor of 5 accounts for the four possible directions each tile can connect to, plus the recurrent connections within the tile). Evenly dividing the N total number of neurons in each Neuron Tile gives rise to $T = \text{ceil}(N/k)$ required Neuron Tiles. This brings the total number of devices attributed to the Neuron Tile to $T \cdot 5k^2$.

The number of Routing Tiles that connects all the Neuron Tiles depends on the geometry of the Mosaic systolic array. Here, we assume Neuron Tiles assembled in a square, each with a Routing Tile on each side. We consider R to be the number of Routing Tiles with $(4k)^2$ devices in each. This brings the total number of devices related to Routing Tiles up to $MF_{RoutingTiles} = R \cdot (4k)^2$.

The problem can then be re-written as a function of the geometry. Considering Fig.5.1g, let i be an integer and $(2i + 1)^2$ the total number of tiles. The number of Neuron Tiles can be written as $T = (i + 1)^2$, as we consider the case where Neuron Tiles form the outer ring of tiles. As a consequence, the number of Routing Tiles is $R = (2i + 1)^2 - (i + 1)^2$. Substituting such values in the previous evaluations of $MF_{NeuronTiles} + MF_{RoutingTiles}$ and remembering that $k < N \cdot T$, we can impose that $MF_{Mosaic} = MF_{NeuronTiles} + MF_{RoutingTiles} < MF_{MF_{ref}}$.

This results in the following expression:

$$MF_{Mosaic} = MF_{NeuronTiles} + MF_{RoutingTiles} < MF_{reference} \quad (5.1)$$

$$(i + 1)^2 (5k^2) + [(2i + 1)^2 - (i + 1)^2] (4k)^2 < (k(i + 1)^2)^2 \quad (5.2)$$

This expression can then be evaluated for i , given a network size, giving rise to the relationships as plotted in Fig.5.1g in the main text.

CONCLUSIONS

In this thesis, I explored implementing neural computation on mixed-signal hardware with in-memory computing capabilities. Neural computation (i.e., inference, learning and routing) is fundamentally memory-centric, and von Neumann architecture's separation of memory and computation is a major contributor to modern neural networks' overall energy consumption and latency. Based on this observation, we investigated offloading critical neural computations directly onto the raw analog dynamics of resistive memory technologies.

This thesis begins by addressing the challenge of online training of feedforward spiking neural networks implemented using intrinsically 1-bit RRAM devices. In Chapter 2, we presented a novel memristor programming technique to precisely control the filament formation in RRAMs devices, increasing their effective bit resolution for more stable training dynamics and improved performance. The versatility of this technique was further demonstrated by applying it to novel perovskite memristors in Chapter 4, achieving an even more linear device response.

In Chapter 3, we tackled the temporal credit assignment problem in RSNNs on an analog substrate. We developed a simulation framework based on a comprehensive statistical model of the PCM crossbar array, capturing major non-linearities of memristors. This framework enabled the simulation of device responses to various weight programming techniques designed to mitigate these non-idealities. Using this framework, we trained a RSNN with the e-prop local learning rule, demonstrating that gradient accumulation is crucial for accurately reflecting weight updates on memristive devices - a finding later validated on a real neuromorphic chip. While our solution, which relies on a digital coprocessor, incurs an energy cost, it motivates the development of future devices with intrinsic accumulation capabilities, potentially through conductance or charge storage. Additionally, we introduced PCM-trace, a scalable implementation of synaptic eligibility traces for local learning using the volatile regime of PCM devices.

In Chapter 4, we presented a discovery of a novel memristor capable of switching between volatile and non-volatile modes. This reconfigurable memristor, based on halide perovskite nanocrystals, offers a significant advancement in emerging memory technologies, enabling the implementation of both static and dynamic neural parameters with the same material and fabrication technique.

Finally, in Chapter 5, we introduced Mosaic, a memristive systolic architecture for in-memory computing and routing. Mosaic efficiently implements small-world graph connectivity, demonstrating superior energy efficiency in spike routing compared to other hardware platforms. Additionally, we introduced a hardware-layout aware training method that takes the physical layout of the chip into account while optimizing the neural network weights.

Discussion and Outlook

I conclude by highlighting significant limitations of neural computation on analog substrates, which serve as a foundation for future research.

1. **Discovering efficient material and peripheral circuits** Although our experiments demonstrate the potential of learning on analog substrates using mature RRAM and PCM technologies, significant challenges remain in achieving efficiency of digital accelerators. *Limited bit resolution* inherent to these devices necessitates energy-intensive gradient accumulation on a co-processor, hindering overall efficiency. As the analog device sizes shrink, this problem is expected to become more pronounced. While improving bit precision can enhance accuracy, it alone won't guarantee efficient analog learning. Additionally, the *high WRITE operation energy* of memristors needs to be lowered to match the low programming energies of SRAM. Finally, it's worth noting that *scaling* trends are primarily driven by peripheral circuitry, rather than the memory cells, necessitating area optimization on the periphery to achieve cost-effective fabrication. Future research should prioritize addressing these challenges, relatively in this order to achieve learning performances competitive with digital accelerators.
2. **Local learning in unconventional networks** The co-design approach is driving neural architectures to be increasingly tailored to hardware for efficiency. For example quantization is adapted to reduce memory footprint, State Space Models (SSMs) leverage recurrency and improve arithmetic intensity (FLOPs/byte) in digital and spiking neurons convert analog membrane voltage to binary spikes and eliminate the need for ADC in analog. It seems reasonable to expect more such primitives to emerge potentially leveraging sparsity or stochasticity. This raises the question of how to design local learning rules for unconventional future architectures. Can a single learning rule provide an end-to-end solution, or can credit assignment be modularized for subgraphs? Recent work suggests that exploring such directions may yield valuable insights and unexpected performance tradeoffs [69, 71, 72, 343, 344].
3. **Mismatch between silicon and brain** Biological plausibility and silicon efficiency represent distinct optimization goals. While silicon dynamics outpace neuronal dynamics in raw speed ¹, it falls short in matching the brain's power efficiency and parallelism. I argue that while mimicking the brain's intricacies may be scientifically interesting, it is not necessarily an ideal blueprint for either silicon efficiency or intelligence. Instead, focusing on silicon efficiency allows us to leverage the unique strengths of this substrate. This will naturally lead to design principles that are common, such as minimizing wiring and localizing computation, however, we are not bound by the specific artifacts of biological evolution. So it remains an open question which criteria from neuroscience should inform hardware design improvements.
4. **Remembering the Jevons Paradox** While hardware-algorithm co-design aims to enhance the power efficiency of on-device intelligence, the Jevons Paradox suggests that this may inadvertently increase overall AI energy consumption due to increased demand [345]. This is a phenomenon occurred in the past, where increasing efficiency of coal engines led to more coal consumption. This raises important questions for future investigation about potential societal and governmental regulations to mitigate the environmental impact, or more exotic technological deployment strategies that keep carbon footprint of AI on the Earth minimal.

¹ Electron mobility in transistors is at least 10^7 time faster than ion transport rate in neuron channels.

At the time of writing, learning on mixed-signal hardware with memristive weights hasn't reached the efficiency of digital accelerators. It seems probable that in the future the scene will evolve as the material design and fabrication technology quickly mature. Nevertheless, it will remain an exciting playground where intelligence meets the raw, unfiltered physics of computation.

APPENDIX

We present here some additional results to complement the main results discussed in the previous sections.

APPENDIX 1: ONLINE TRAINING OF SPIKING RECURRENT NEURAL NETWORKS WITH PHASE-CHANGE MEMORY SYNAPSES

SUPPLEMENTARY NOTE 1 We implemented the PCM crossbar array simulation framework in PyTorch [107], which can be used for both the inference and the training of ANNs or SNNs. Built on top of the statistical model introduced by Nandakumar et al. [81], our crossbar model supports asynchronous SET, RESET and READ operations over entire crossbar structures and simultaneously keep tracks of the temporal evolution of device conductances.

A single crossbar array consists of $P \times Q$ nodes (each node representing a synapse), where single node has $2N$ memristors arranged using the differential architecture (N potentiation, N depression devices). Each memristor state is represented by four variables, t_p for storing the last time the device is written (which is used to calculate the effect of the drift), $count$ for counting how many times it has written (to be used later in the arbiter of N-memristor architectures), P_{mem} for its programming history (required by the PCM model) and G for representing the conductance of the the device at T_0 seconds later after the last programming time. The initial conductances of PCM devices in the crossbar array are assumed to be iteratively programmed to HRS, sampled from a Normal distribution $\mathcal{N}(\mu = 0.1, \sigma = 0.01)$ μS .

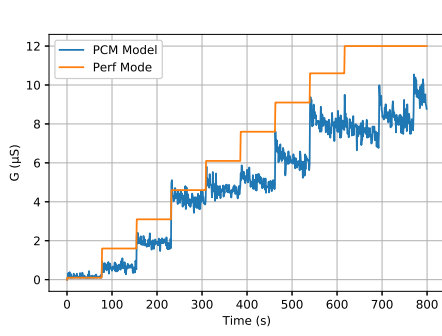
The PCM crossbar simulation framework supports three major functions: READ, SET and RESET. The READ function takes the pulse time of the applied READ pulse, t , and calculates the effect of drift based on the last programming time t_p . Then, it adds the conductance-dependent READ noise and returns the conductance values of whole array. The SET function takes the timing information of the applied SET pulse, together with a mask of shape $(2 \times N \times P \times Q)$ and calculates the effect of the application of a single SET pulse on the PCM devices that are selected with the mask. Finally, the RESET function initializes all the state variables of devices selected with a mask and initializes the conductances using a Normal distribution $\mathcal{N}(\mu = 0.1, \sigma = 0.01)$ μS .

SUPPLEMENTARY NOTE 2 READ and WRITE operations to simulated PCM devices in the crossbar model are stochastic and subject to the temporal conductance drift. Additionally, PCM devices offer a very limited bit precision. Therefore, to ease the network training procedure, especially the hyperparameter tuning, we developed the *perf-mode*. When crossbar model is operated in *perf-mode*, all stochasticity sources and the conductance drift are disabled. READ operations directly access the device conductance without $1/f$ noise and drift, whereas SET operations increase the device conductance as

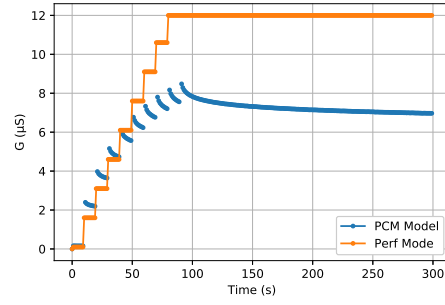
$$G_N = G_{N-1} + \frac{G_{MAX}}{2^{CB_{RES}}}, \quad (\text{A.1})$$

where, G_{MAX} is the maximum PCM conductance set to $12 \mu\text{S}$ (conductivity boundaries are determined based on the device measurements from [81]), and CB_{RES} is the desired bit-resolution of a single PCM device. In a nutshell, the *perf-mode* turns PCMs into an ideal memory cells corresponding to a digital memory with a limited bit precision.

SUPPLEMENTARY NOTE 3 Here, we demonstrate the impact of using multiple memristor devices per synapse (arranged in differential configuration) on the precision of targeted programming updates. Specifically, we modeled synapses with $N = 1, 4, 8$ PCM devices and programmed them from initial conditions of integer conductance values $G_{source} \in \{-10, 10\}$ μS to integer



(a) Comparison of the full PCM model and its perf-mode equivalent after 8 consecutive SET pulses.



(b) Comparison of the full PCM model and its perf-mode equivalent after 8 consecutive SET pulses, averaged over 300 measurements showing the effect of drift.

FIGURE A.1: The PCM crossbar model supports both the full PCM model from [81] and its corresponding simplified version as an ideal digital memory in perf-mode.

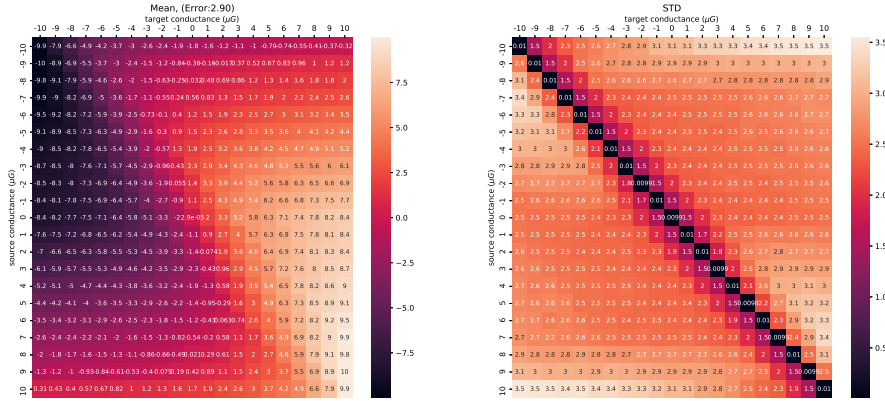


FIGURE A.2: Multi-memristor configuration with 1 PCM (one depression and one potentiation) per synapse

conductance values $G_{target} \in \{-10, 10\} \mu S$ using the multi-memristor update scheme described in Section 3.1.3.2. The effective conductance of a synapse is calculated by $G_{syn} = \sum_{i=0}^N G_i^+ - \sum_{i=0}^N G_i^-$, however we normalized the conductance across 1-PCM, 4-PCM and 8-PCM architectures for an easier comparison, such that $G_{syn} = \frac{1}{N}(\sum_{i=0}^N G_i^+ - \sum_{i=0}^N G_i^-)$.

Our empirical results verifies the claim of Boybat et al. [109] that the standard deviation and the update resolution of the write process decreases by \sqrt{N} .

SUPPLEMENTARY NOTE 4 In the differential architectures, consecutive SET pulses applied to positive and negative memristors may cause the saturation of the synaptic conductance and block further updates. The saturation effect is more apparent when a single synapse gets 10+ updates in one direction (potentiation or depression) during the training. For example, this effect is clearly visible in SupplFig. A.2, Fig. A.3 and Fig. A.4, when the source conductance and target conductances differ by more than 8-10 μS .

We implemented a weight update scheme denoted as the update-ready criterion, which aims to prevent conductance saturation while applying single large updates. Before doing the update, we read both positive and negative pair conductances, and check if the target update is possible. If not, we reset both devices, calculate the new target and apply the number of pulses accordingly. For example, given $G^+ = 8\mu S$ and $G^- = 4\mu S$ and the targeted update $+6\mu S$, the algorithm decides to reset both devices because G^+ can't be increased up to $14\mu S$. After both devices are

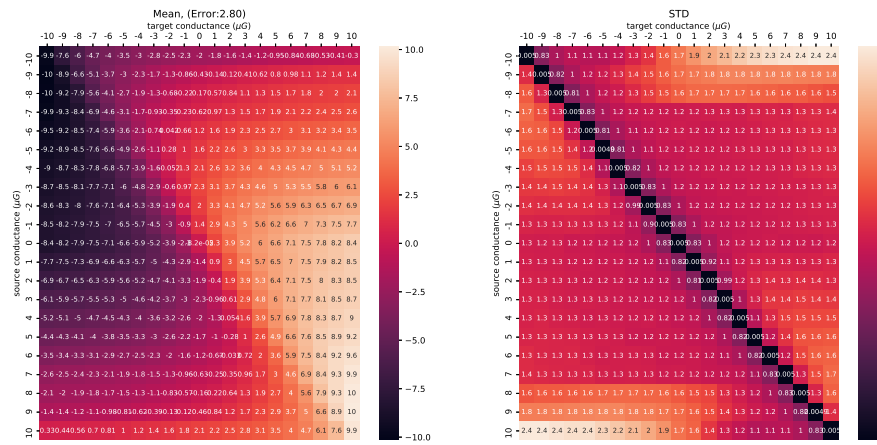


FIGURE A.3: Multi-memristor configuration with 8 PCM (four depression and four potentiation) per synapse

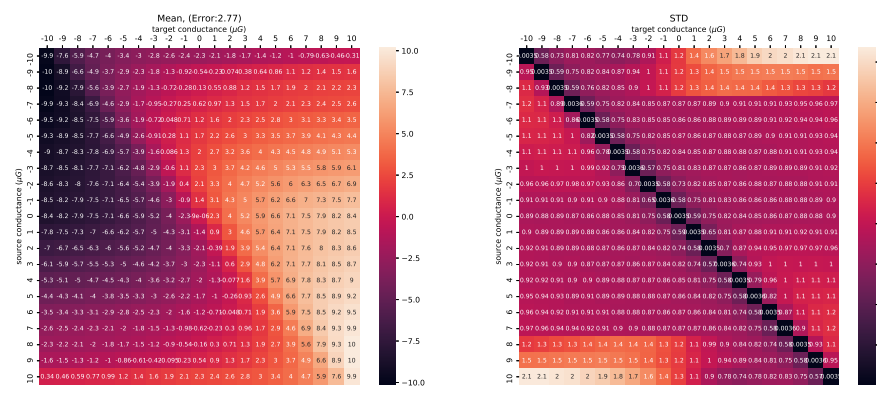


FIGURE A.4: Multi-memristor configuration with 16 PCM (eight depression and eight potentiation) per synapse

reset, G^+ can be programmed to $10\mu S$). Although our PCM crossbar array simulation framework supports it, this weight transfer criterion is not used in our simulations because it requires reading the device states during the update.

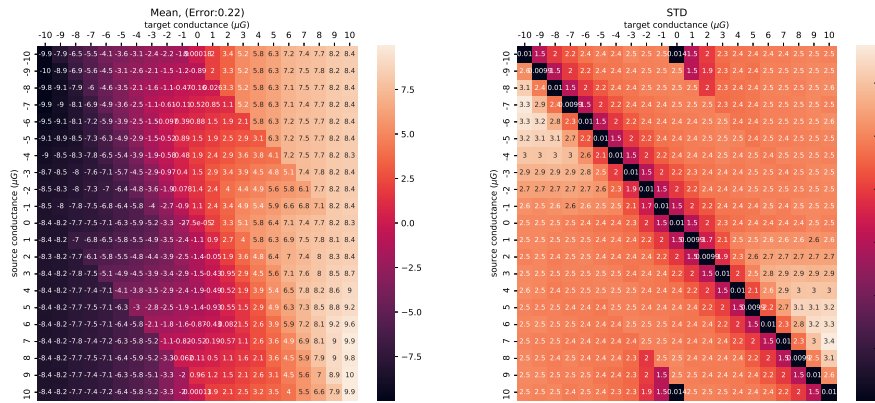


FIGURE A.5: Update-ready criterion tested with $N = 1$ memristor per synapse.

SUPPLEMENTARY NOTE 5 We have defined the task success criteria as MSE Loss < 0.1 based on visual inspection. Below in Fig A.6, some network performances are shown.

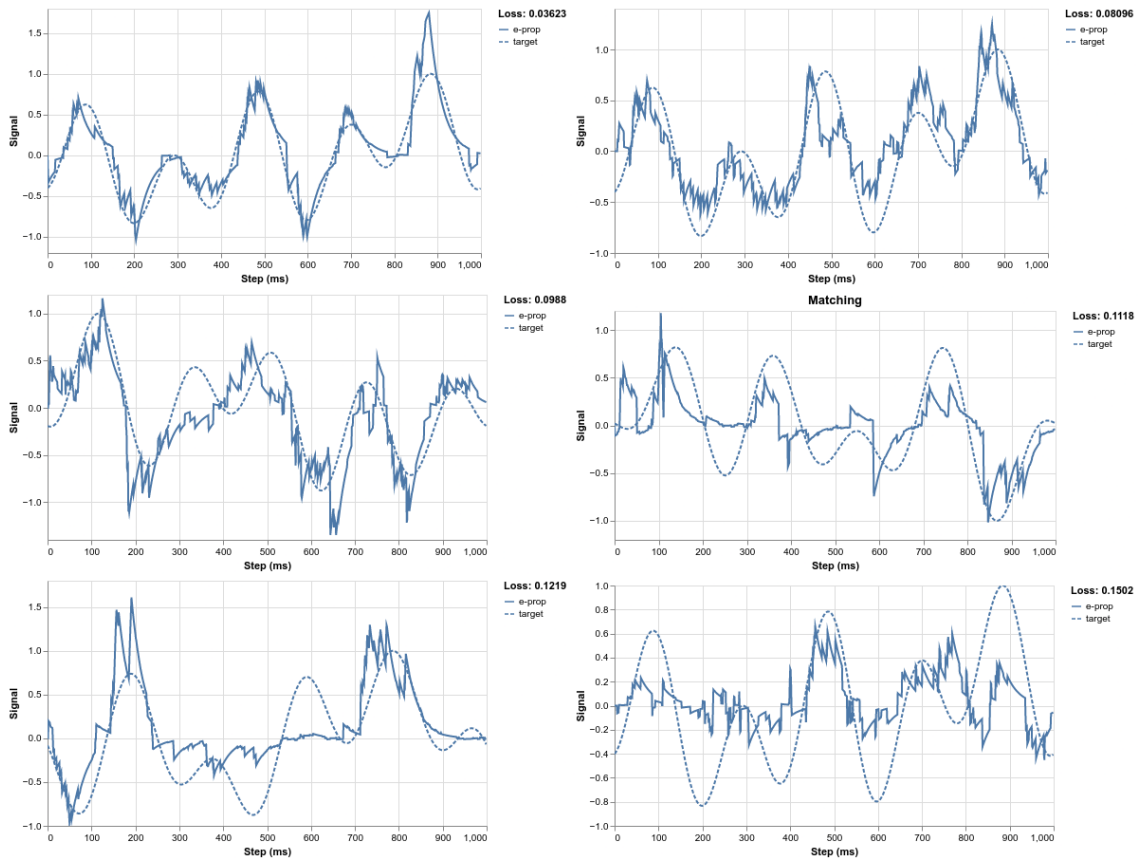


FIGURE A.6: Comparison of network performances with six different loss values.

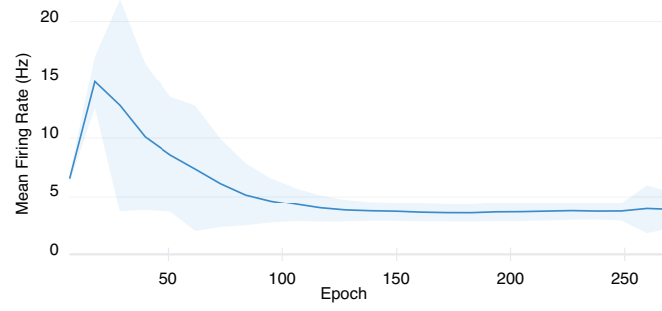


FIGURE A.7: Mean firing rate of 50 networks with PCM synapses trained using the mixed-precision method.

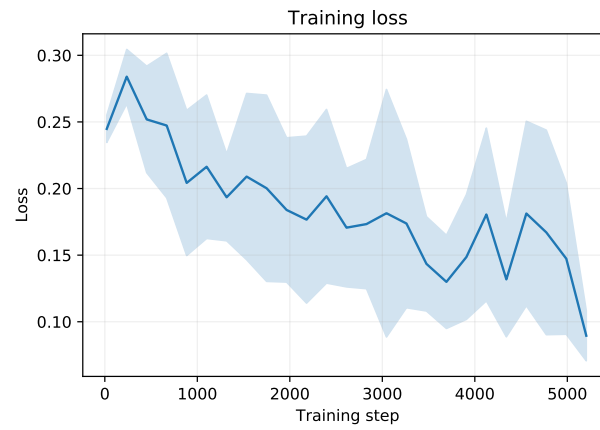


FIGURE A.8: MSE loss of 50 networks trained with PCM synapses using the mixed-precision method.

SUPPLEMENTARY NOTE 6

APPENDIX 2: MOSAIC: IN-MEMORY COMPUTING AND ROUTING FOR SMALL-WORLD SPIKE-BASED NEUROMORPHIC SYSTEMS

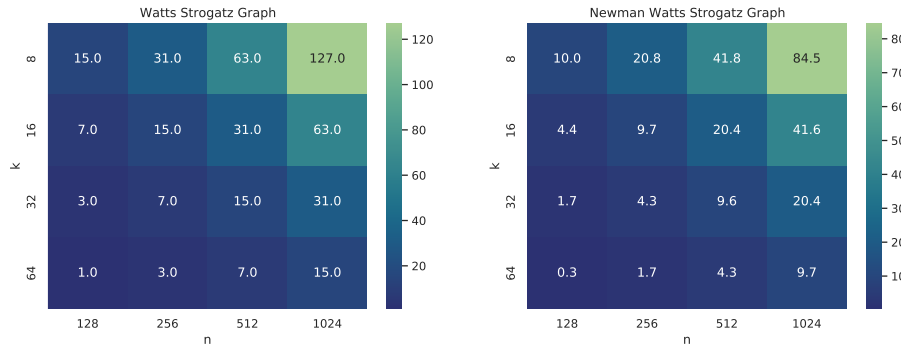


FIGURE A.9: The heatmaps show the ratio of zero elements to non-zero elements in the connectivity matrix for two examples of recurrently connected small-world graph generators. As n (number of nodes, e.g., neurons, in the graph) increases and k (number of neighbour nodes for each node in a ring topology) decreases, the more connections in the connectivity matrix will be zero, indicating the increased proportion of non-used memory elements in a $n \times n$ crossbar array.

SUPPLEMENTARY NOTE 1 Figure A.9 quantifies the under-utilization of conventional crossbar arrays while storing example small-world connectivity patterns generated by two standard random graph generation models: Watts-Strogatz small-world graphs [279] and Newman-Watts-Strogatz small-world graphs [346]. The first type of graphs is characterized by a high degree of local clustering with short vertex-vertex distances, observed in neural networks and self-organizing systems, whereas the latter type mostly captures the properties of lattices associated with statistical physics.

SUPPLEMENTARY NOTE 2 To communicate the events between the computing nodes in neuromorphic chips, AER communication scheme has been developed and used [308]. In AER, whenever a spiking neuron in a chip (or module) generates a spike, its “address” (or any given ID) is written on a high-speed digital bus and sent to the receiving neuron(s) in one (or more) receiver module(s). In general, AER processing modules require at least one AER input port and one AER output port. As neuromorphic systems scale up in size, complexity, and functionality, researchers have been developing more complex and smarter AER “variations” to maintain the efficiency, reconfigurability, and reliability of the ever-growing target systems they want to build. The scheme that is used to transport events can be source or destination based, where the source or destination address is embedded in the sent event “packet”. In the source-based scheme, each receiving neuron has a local CAM that stores the address of all the neurons that are connected to it. In the destination-based approach, each event hops between the nodes where its address gets compared to the node’s address until it matches and thus gets delivered. Source-driven routing provides the designer with more freedom to balance event traffic and design routes, but the hardware complexity increases the delays. Destination-based creates pre-determined routes along the network and the designer can only change the output ports [347]. In summary, in source-based routing, the system requires a CAM memory per neuron, which results in an increase in the area and memory access read times. In destination-based routing, the configurability in the network structure is reduced. Comparatively, in the Mosaic, the routers are memory crossbars that are distributed between the computing cores and steer the spiking information in the mesh. Thus, neither local CAMs, nor a centralized memory is required for routing.

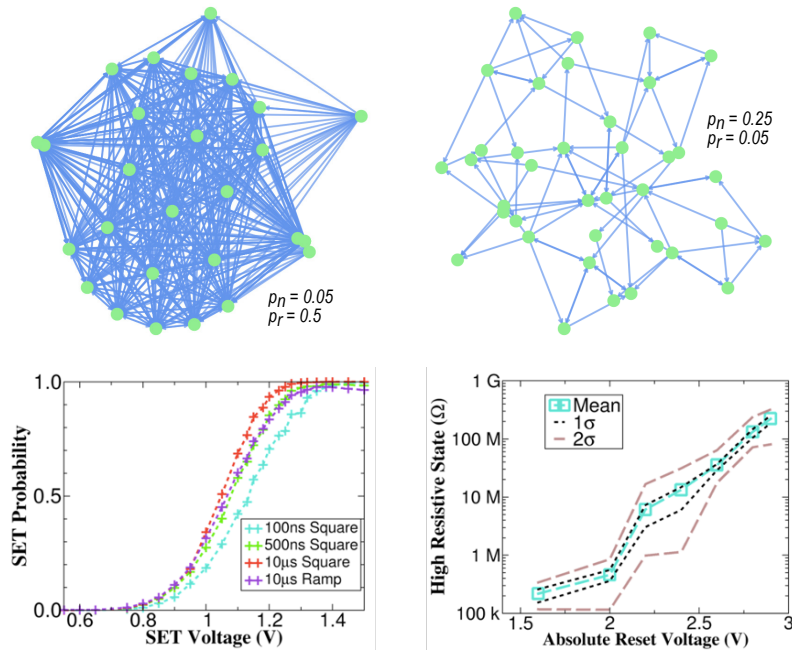


FIGURE A.10: (top) Different random graphs generated using Mosaic model, changing the probability of devices being in their High Conductive state in the neuron tile (p_n) and routing tile (p_r). (bottom) The probability of device switching is a function of the voltage applied to it while being programmed.

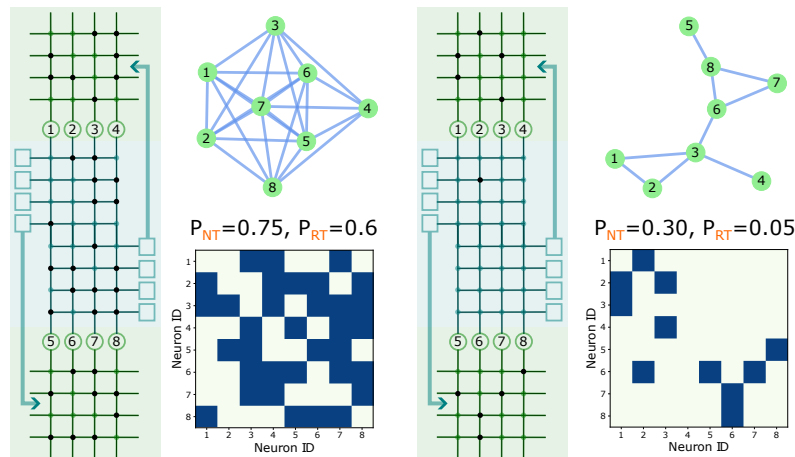


FIGURE A.11: Mosaic connectivity example, formed by setting the probability of connection within Neuron Tile (p_{NT}) and Routing Tiles (p_{RT}). (left) Densely connected Mosaic composed of 2 Neuron Tiles and 1 Routing Tile. The graph related to its connectivity is shown as well adjacency matrix. (right) Sparsely connected Mosaic. The graph is programmed to favor the intra-Neuron Tile connectivity and allow for two clusters to emerge, penalizing connections between the two clusters.

SUPPLEMENTARY NOTE 3 Routing tiles define the connectivity of spiking neural networks implemented on Mosaic. When the number of memristive devices in the routing tiles which are in their high-conductance state (HCS) is not sparse, Mosaic resembles a densely connected neural network (Fig. A.10, top left). When most of the memristor in the routing tiles are in the low-conductance state, Mosaic is sparsely connected (Fig. A.10, top right). Furthermore, one can further sparsify Mosaic networks by setting memristors in the neuron tiles to the LCS. To do so, we can change the probability of memristors being in their HCS in the neuron tiles, p_n , and in the

routing tiles, p_r . The switching of the RRAMs presents the property of probabilistic switching as a function of the voltage applied during the programming operation as is shown in Fig. A.10, bottom.

Fig. A.11 shows the construction of two graph topologies, made of 2 Neuron Tiles and one Routing Tile, to clarify the formation of the graphical structure in the Mosaic. By controlling the probability of connections within the Neuron and Routing Tiles, we can produce a densely connected graph (left) with $p_{NT} = 0.75$, $p_{RT} = 0.6$, and a sparse graph (right) with $p_{NT} = 0.30$, $p_{RT} = 0.05$.

The corresponding connectivity matrix is also shown in the figure, which is directly represented as a hardware architecture in the 3 tiles of the Mosaic, as shown in the figure.

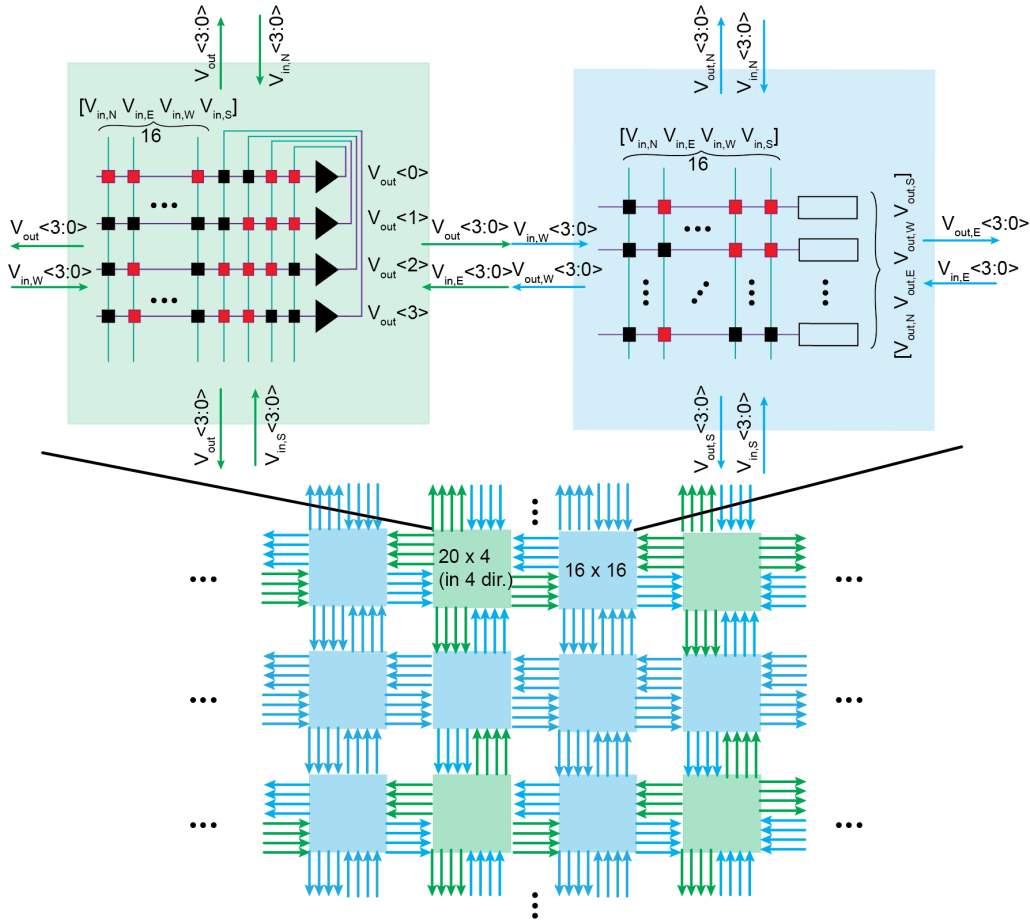


FIGURE A.12: (Neuron tiles (green) transfer information in the form of spikes to each other through routing tiles (blue). Details of the Mosaic architecture is shown with the size of the neuron and routing tiles. The neuron tiles receive feed-forward input from four directions of North (N), East (E), West (W), and South (S), and local recurrent input from the neurons in the tile. The neurons integrate the information and once spike, send their output to 4 directions. Having 4 neurons in a tile, gives rise to 16 outputs (4 outputs copied in 4 directions), and 20 inputs (4 inputs from 4 directions (16), plus 4 recurrent inputs). The routing tiles receive 16 inputs (4 inputs from 4 directions) and send out 16 outputs (4 outputs in 4 directions). In the crossbars, the red squares and black squares represent devices in their high conductive and low conductive state, respectively. The connection between the neuron tile and the routing tile is directly through a wire. For instance, $V_{out} \langle 3:0 \rangle$ is the same as the $V_{in,W}$, and $V_{in,E} \langle 3:0 \rangle$ is the same as $V_{out,W}$.

SUPPLEMENTARY NOTE 4 Figure A.12 shows the details of the Mosaic architecture, with a zoomed in neuron and routing tile pair. The diagram in the top shows how one cluster of neuron/one router sends and receives information to and from the routing/neuron tile. This

highlights the strength of this architecture which makes the connectivity easy through simple wiring to the neighbour, without suffering from long wires, as the maximum length of a wire is the size of the wire from one row/column, plus the size of the connecting column/row.

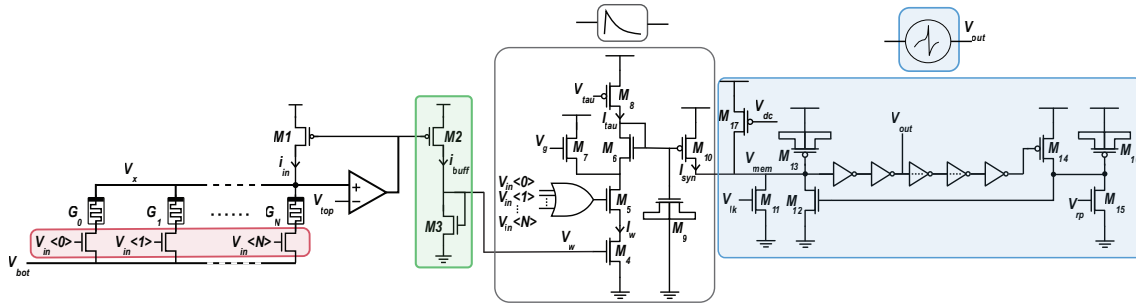


FIGURE A.13: Schematic of the neuron tile including the CMOS synapse and neuron circuits fabricated for use in this paper. RRAMs are used as the weights of the neurons. On the arrival of any of the input events $V_{in<i>}$, the amplifier pins node V_x to V_{top} and thus a read voltage equivalent to $V_{top} - V_{bot}$ is applied across G_i , giving rise to current i_{in} at M_1 . This current is mirrored to M_2 giving rise to i_{buff} which is in turn again mirrored through the $M_3 - M_4$ transistor pair. The “synaptic dynamics” circuit is the Differential Pair Integrator (DPI) [311]. On the arrival of any of the input events, $V_i, 0 < i < n$, I_w , equivalent to i_{buff} , flows in transistor M_5 . Depending on the value on V_g , a portion of I_w flows out of the MOS capacitor M_6 and discharges it. This current is proportional to $G_i, 0 < i < n$. As soon as the event is gone, MOS capacitor M_6 charges back through the M_8 path with current I_{tau} , which determines the rate of charging, and thus the time constant of the synaptic dynamics. The output current of the DPI synapse, I_{syn} , is injected into the neuron’s membrane potential node, V_{mem} , and charges MOS capacitor M_{13} . There is also an alternative path with a DC current input through M_{17} which can charge neuron’s membrane potential. Membrane potential charging has a time constant determined by V_{lk} at the gate of M_{11} . As soon as the voltage developed on V_{mem} passes the threshold of the following inverter stage, it generates a pulse. The width of the pulse, depends on the delay of the feedback path from V_{out} to the gate of M_{12} . This delay is determined by the inverter delays, and the refractory time constant. The inverter symbols with the horizontal dashed lines correspond to a starved inverter circuits with longer delays. The refractory period time constant depends on the MOS cap M_{16} and the bias on V_{rp} .

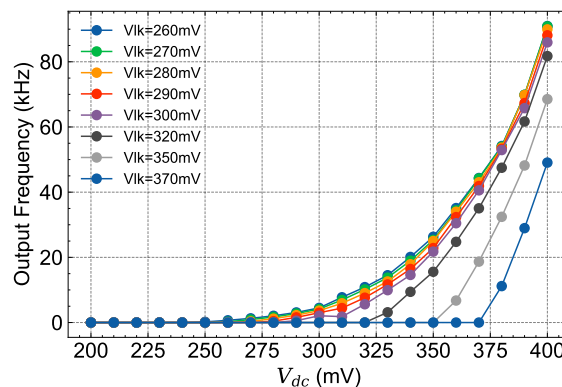


FIGURE A.14: Measurements from fabricated neuron’s output frequency as a function of the input DC voltage. The DC voltage is applied at the gate of transistor M_{17} shown in Fig. A.13 as V_{dc} . Therefore, as the gate voltage of M_{17} changes linearly, the current of M_{17} and thus the output frequency of the neuron changes non-linearly. Each curve is measured with a different neuron’s time constant, determined by a different voltage, V_{lk} , on the gate of transistor M_{11} in Fig. A.13. As the leak voltage increases, the neuron’s time constant decreases, giving rise to a lower output frequency.

SUPPLEMENTARY NOTE 5 Details of the implementation of the neuron row, the circuit that leverages the information of the conductance of a memristor to weight the effect of a spike to a neuron is shown in Figure A.13. The circuit features multiple inputs connected to a row of memristive devices (left) and a Front-End circuit buffering the current read from the devices to a differential-pair-integrator synapse. The synapse is then connected to a leaky-integrated-and-fire (LIF) neuron which eventually emits a spike. Figure A.14 delves deeper in the behavior of the LIF neuron analyzing its output spiking frequency against an input DC voltage and its linear behavior respect to the RRAM conductance in a neuron row circuit.

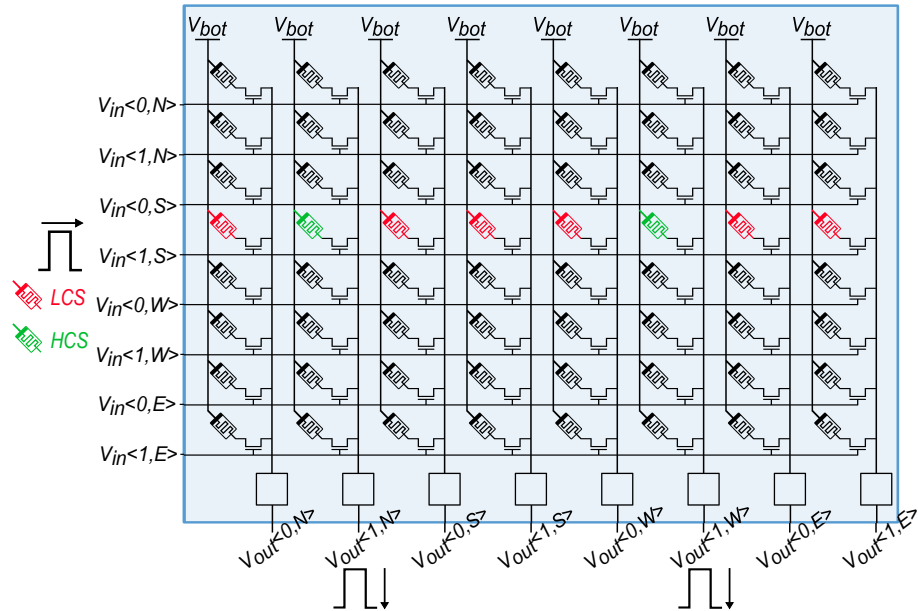


FIGURE A.15: Schematic of a routing tile circuit offering two paths per direction. The routing tile receives eight inputs, comprising two pulse channels per direction, labelled as $\langle 0 \rangle$ or $\langle 1 \rangle$, from the neighbouring tiles to the North (N), South (S), East (E) and West (W), and provides complimentary outputs. An example is shown of an input pulse arriving to the common gate of the fourth row of memory. Devices are coloured green or red to denote whether they are in the HCS or LCS. It is shown that, due to this input pulse, output pulses are produced by the routing columns containing the (green) devices programmed in the HCS.

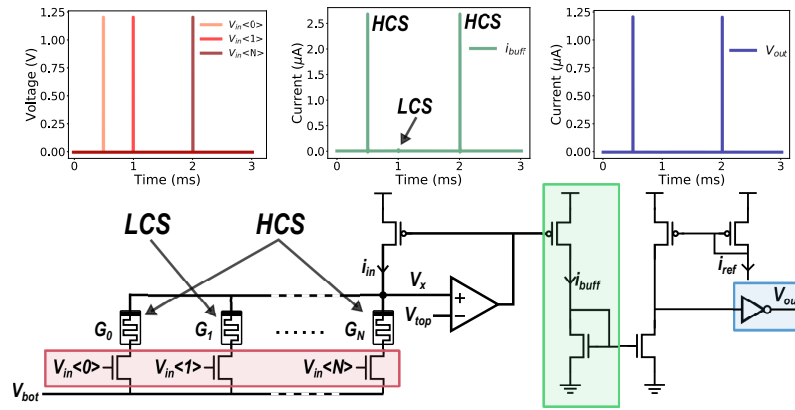


FIGURE A.16: The routing column circuit with example waveforms. Input (red, left) voltage pulses, V_{in} , draw a current i_{in} proportional to the conductance state, G_n , of the read $1T1R$ structures. Two devices are labelled with HCS, indicating that they have been programmed with a conductance corresponding to the high conductance state, and one is labelled LCS in reference to the low conductance state. This resulting currents are buffered (green, centre), i_{buff} , into a current comparator circuit where it is compared with a reference current i_{ref} . When the buffered current exceeds the reference current a voltage pulse is generated at the column output (blue, right).

SUPPLEMENTARY NOTE 6 Details on the implementation of the Routing Tiles. Figure A.15 shows a full-size schematics of a routing tile with 2 neurons allocated per direction. Figure A.16 expands on the details of the implementation of the routing column, the circuit that uses the state of a memristor to decide whether to block or pass (route) a spike through the Mosaic architecture.

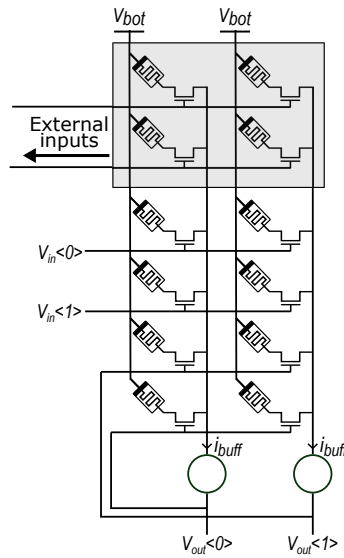


FIGURE A.17: An example of how a neuron tile can be interfaced to external event-based inputs (i.e., those generated by an event-based sensor). With respect to the neuron tile circuit presented in the paper (permitting connections to adjacent tiles as well as recurrent connections within the tile), this figure shows two additional rows of devices stacked on top of the array. As an arbitrary example, here two additional signals can be integrated in the neuron circuits.

SUPPLEMENTARY NOTE 7

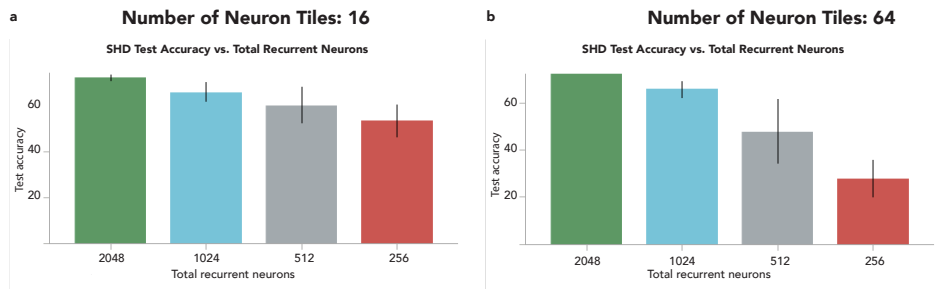


FIGURE A.18: SHD keyword spotting dataset test accuracies for Mosaic architectures with different total number of neurons in the network for a) 4x4 Neuron Tile layout (a total of 16 number of Neuron tiles) and b) 8x8 Neuron Tile layout. The number of neurons per tile is equal to the total number of recurrent neurons divided by the number of neuron tiles. Median and standard deviation are calculated using 3 experiments with varying sparsity constraints.

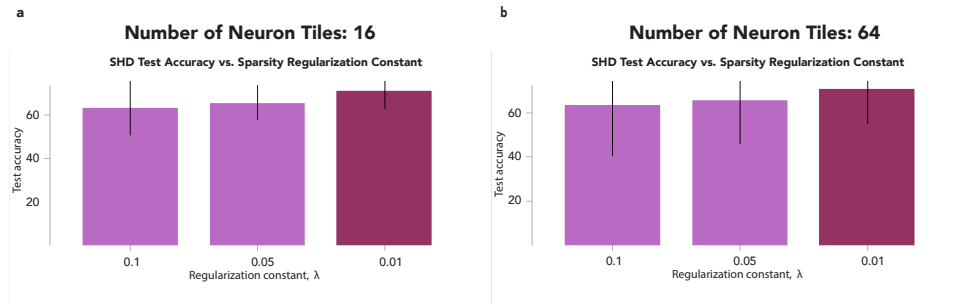


FIGURE A.19: SHD keyword spotting dataset test accuracies for Mosaic architectures trained with different sparsity regularization values. As explained in the Methods section of the main text, the regularization is added to the loss function to exponentially penalize the long-range connections. The plot shows the accuracy for strong (default, $\lambda = 0.1$), medium ($\lambda = 0.05$) and weaker ($\lambda = 0.01$) sparsity regularization on a) 4×4 neuron tile layout and b) 8×8 neuron tile layout. Median and standard deviation are calculated using 4 experiments with varying number of neurons per neuron tile.

SUPPLEMENTARY NOTE 8

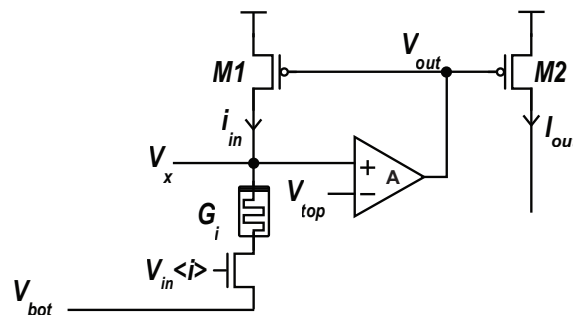


FIGURE A.20: Analysis of the read-out circuitry. The amplifier with gain A , pins voltage V_x to the voltage V_{top} . On the arrival of the pulse on $V_{in} < i >$, a current equal to $i_{in} = (V_{top} - V_{bot})G_i$ flows into the memristor i , which is then mirrored out i_{out} .

SUPPLEMENTARY NOTE 9 Figure A.20 details the implementation of the read-out circuit used in the Mosaic architecture. Though not optimized for area, we have used this implementation for both the neuron and routing tiles.

The dominant power consumption of the circuit depends on the required bandwidth (BW) of the feedback loop. This BW depends on the maximum conductance of the RRAM, G_{max} . For $G_{i,max}$, once an input arrives to $V_{in} < i >$, the current i_{in} has to settle to $(V_{top} - V_{bot})G_{i,max}$ within a settling time, t_s , a proportion of the pulse width. This timing sets the speed at which the loop should work, and thus its BW. If the loop does not close in this time, the amplifier will slew, and the voltage V_x drops. In both neuron and routing tiles, this condition should be met for V_x to stay pinned at V_{top} while RRAM is being read. However, the neuron and routing tiles have different BW requirements.

In the **neuron tile**, the read-out circuitry has to resolve between at least 8 levels of current for the 8 levels that each RRAM device can take. Therefore, the Least Significant Bit (LSB) of the i_{in} current for the neuron tile is $i_{in,LSB,N} = \frac{V_{ref}(G_{max} - G_{min})}{N}$. Based on the Fig. 5.2d, this value for the neuron tile is $\frac{100mV(120\mu S - 40\mu S)}{8} = 1\mu A$. Note that since the 8 levels to be resolved are in the Low Resistive State of the RRAM, the G_{max} and G_{min} are the minimum and maximum of the range in the LRS, which correspond to $40\mu S$ and $120\mu S$.

In the **routing tile**, the read-out circuitry has to resolve between two levels which will either let the spike regenerate and thus propagate, or will get blocked. Therefore, the LSB of the i_{in} current in the routing tile is $i_{in,LSB,R} = \frac{V_{ref}(G_{max} - G_{min})}{N}$. Based on the Fig. 5.2d, this value for the neuron

tile is $\frac{100mV(40\mu S-10\mu S)}{2} = 15\mu A$. Note that since the 2 levels to be resolved are the LRS and HRS of the RRAM, the G_{max} and G_{min} correspond to $10\mu S$ and $40\mu S$.

To be able to distinguish between any two levels in both cases, we will consider a maximum error of $\frac{i_{in,LSB}}{2}$. Therefore, the maximum tolerable error in the the neuron tile is $0.5\mu A$ and in the routing tile is $7.5\mu A$.

This means that if the feedback loop does not close in t_s of the pulse width, V_x drop is a lot more tolerable in the routing tile than it is in the neuron tile. This suggests that the bandwidth requirements in the case of neuron tile is $7.5/0.5 = 15$ times more than that of the routing tile. The BW requirements directly translate to the biasing of the amplifier and thus its power consumption. Therefore, the static power consumption of the neuron tile is 15 times that of the routing tile. The current requirements also translate to area, since larger currents require wider transistors.

APPENDIX 3: RECONFIGURABLE HALIDE PEROVSKITE NANOCRYSTAL MEMRISTORS FOR NEUROMORPHIC COMPUTING

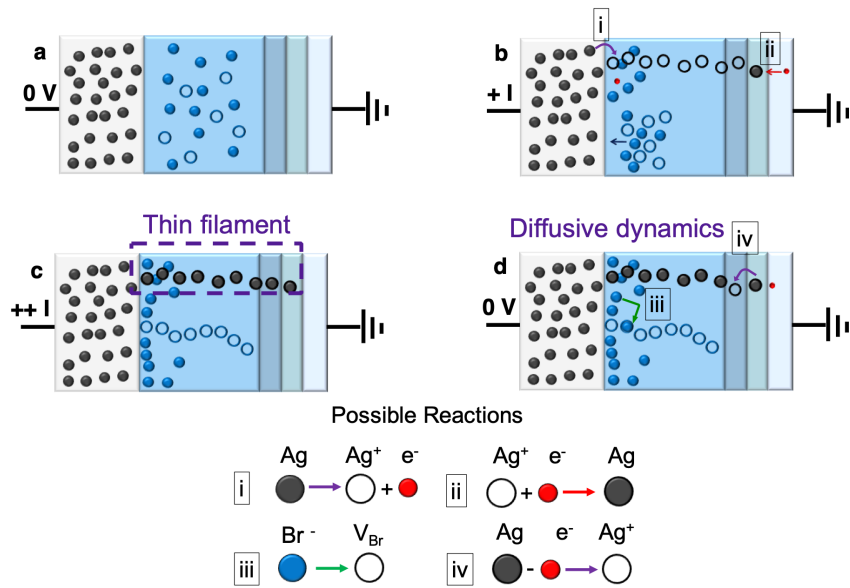


FIGURE A.21: Proposed volatile diffusive switching mechanism. (a-d) illustrate the various stages of filament formation and rupture. i-iv indicate the possible reactions happening within the device.

SUPPLEMENTARY NOTE 1 Diffusive behaviour: The volatile threshold switching behaviour can be attributed to the redistribution of Ag^+ and Br^- ions under an applied electric field, and their back-diffusion upon removing power. The soft lattice of the halide perovskite matrix has been observed to enable Ag^+ migration with an activation energy $\sim 0.15eV^2$. Interestingly, migration of halide ions and their vacancies within the perovskite matrix also occur at similar energies $\sim 0.10 - 0.25eV$ [253, 348, 349], making it difficult to pinpoint a singular operation mechanism. We hypothesize that during the SET process, Ag atoms are ionized to Ag^+ and forms a percolation path through the device structure. Electrons from the grounded electrode oxidize Ag^+ to form weak Ag filaments. Parallely, Br^- ions get attracted towards the positively charged electrode and a weak filament composed of vacancies (V_{Br}) is formed. Both these factors increase the device conductance from a high resistance state (HRS) to a temporary low resistance state (LRS). Upon removing the electric field, the low activation energy of the ions causes them to diffuse back spontaneously, breaking the percolation path and leading to volatile memory characteristics a.k.a. short-term plasticity. The low compliance current (I_{cc}) of $1\mu A$ ensures that the electrochemical reactions are well regulated, and the percolation pathways formed are weak enough to allow these diffusive dynamics.

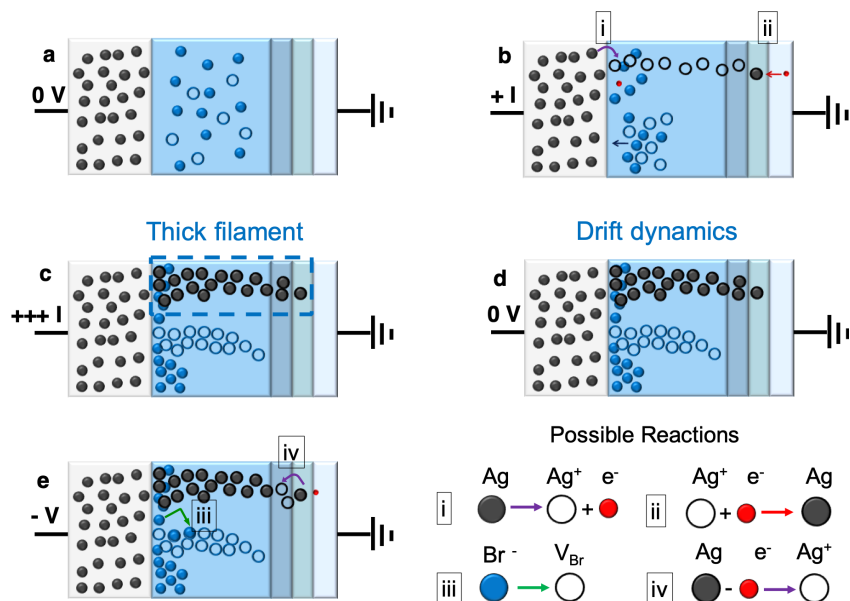


FIGURE A.22: Proposed non-volatile drift switching mechanism. (a-e) illustrate the various stages of filament formation and rupture. i-iv indicate the possible reactions happening within the device.

SUPPLEMENTARY NOTE 2 Drift behaviour: Upon increasing the I_{cc} to 1 mA (3 orders of magnitude higher than that used for volatile threshold switching), permanent and thicker conductive filamentary pathways are possibly formed within the device as illustrated in Fig. A.22. This increases the device conductance from a high resistance state (HRS) to a permanent and much lower low resistance state (LRS). Electrochemical reactions are triggered to a higher extent and hence, the switching dynamics is now dominated by the drift kinetics of the mobile ion species Ag^+ and Br^- , rather than diffusion. Hence upon removing the electric field, the conductive filaments remain largely unaffected, and the devices retain their LRS and portray long-term plasticity. Application of voltage sweeps, or pulses of opposite polarity causes rupture of these filaments, and the devices are reset to their HRS. For DDAB-capped $CsPbBr_3$ NCs, the devices transition to a non-erasable non-volatile state within ~ 50 cycles, indicating formation of very thick filaments (Fig. A.23) On the other hand, the OGB-capped $CsPbBr_3$ NCs display a record-high nonvolatile endurance of 5655 cycles and retention of 10^5 seconds (Fig. A.24), pointing to better regulation of the filament formation and rupture kinetics.

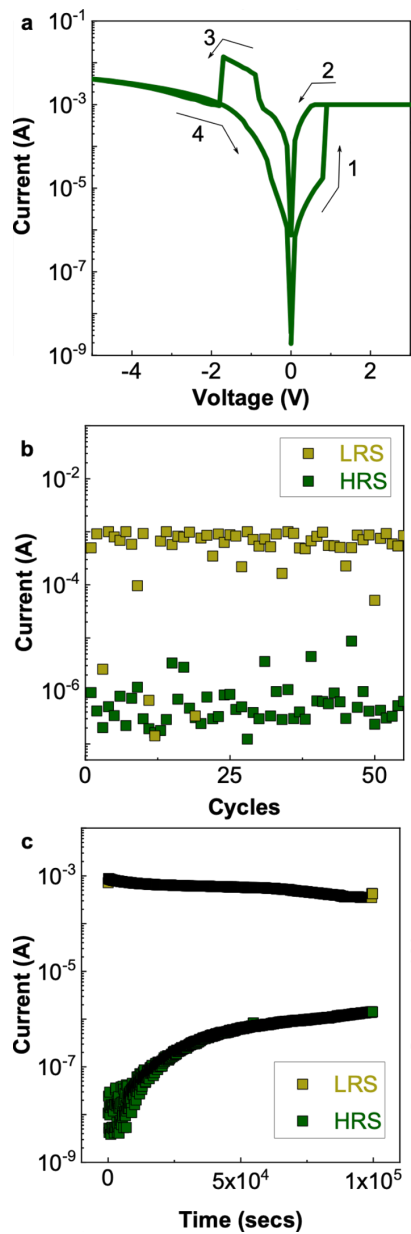


FIGURE A.23: Non-volatile drift switching of DDAB-capped CsPbBr₃ NC memristors. (a) Representative IV characteristics. (b) Endurance. (c) Retention.

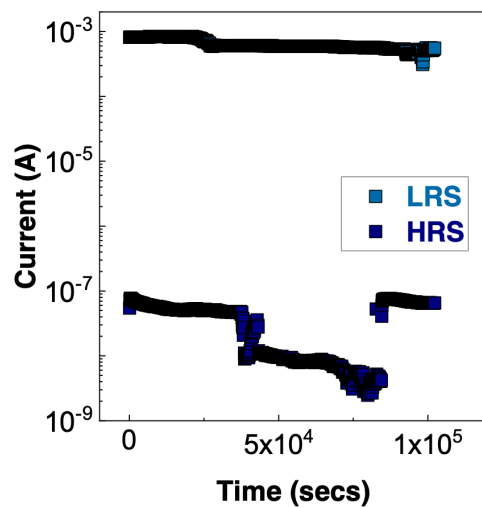


FIGURE A.24: Non-volatile drift switching of OGB-capped CsPbBr₃ NC memristors. Figure shows the retention performance.

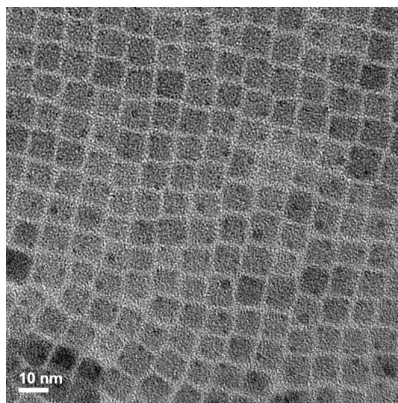


FIGURE A.25: Transmission electron microscope (TEM) images of DDAB-capped CsPbBr₃ NCs.

SUPPLEMENTARY NOTE 3

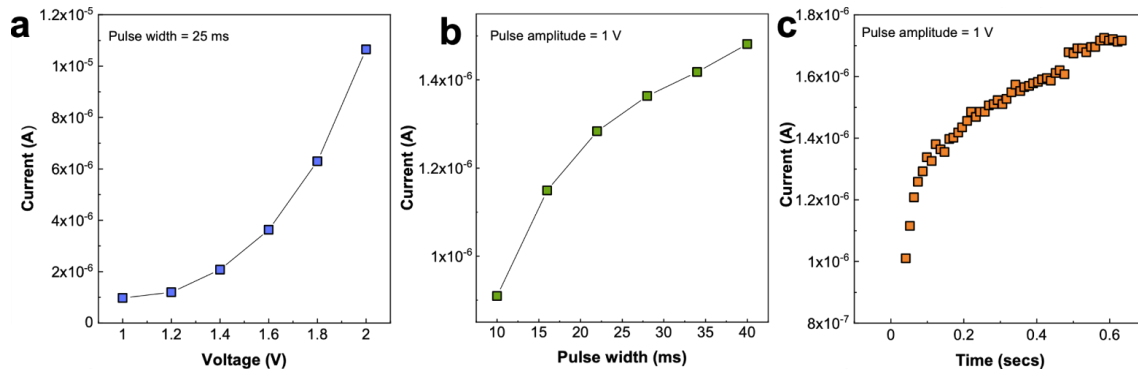


FIGURE A.26: Non-linear variation of the device conductance as a function of the stimulation pulse (a) amplitude, (b) width and (c) number. For (a), the pulse width and number is kept constant at 25 ms and 1 respectively. For (b), the pulse amplitude and number is kept constant at 1 V and 1 respectively. For (c), the pulse amplitude and width is kept constant at 1 V and 25 ms respectively.

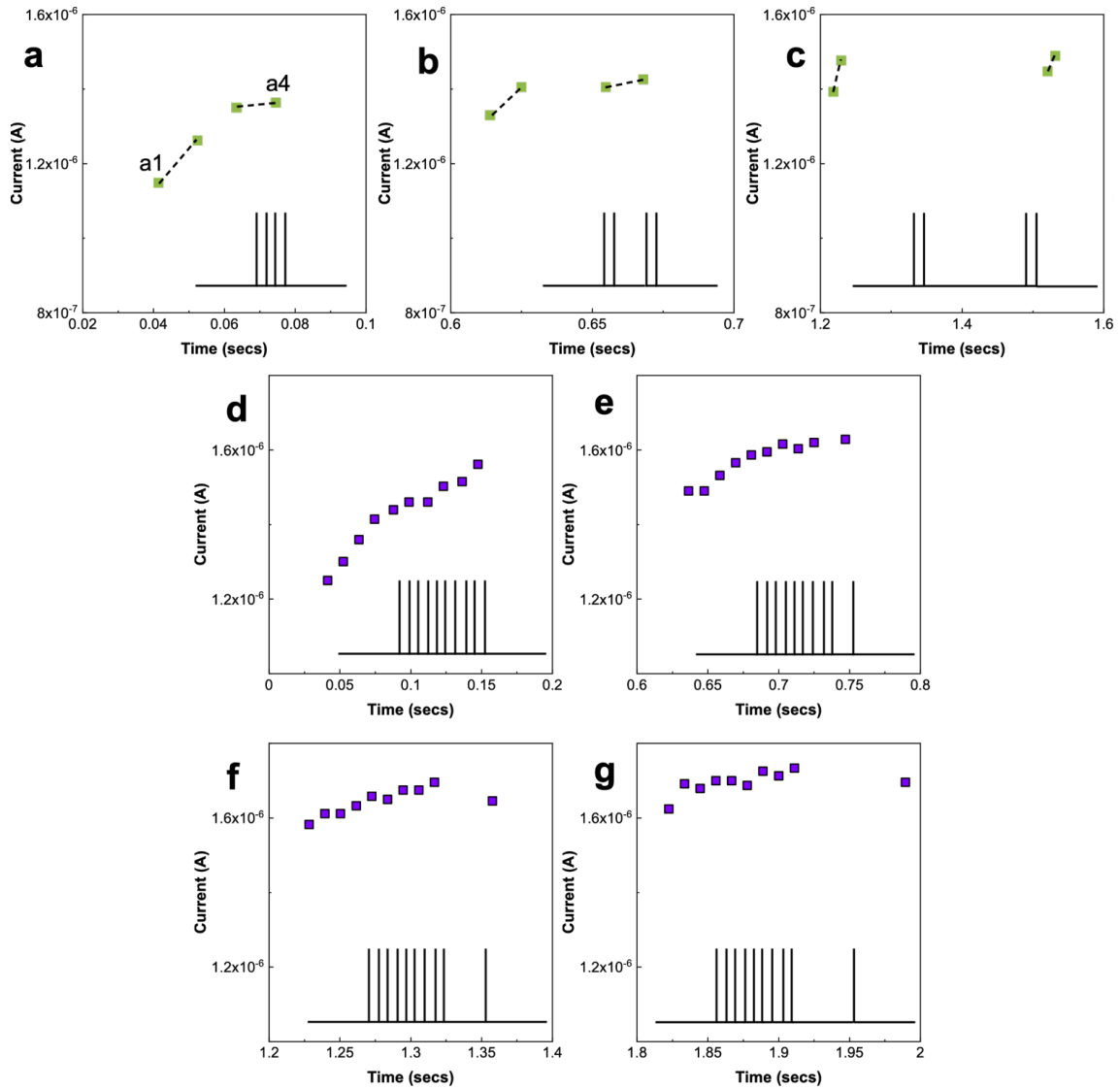


FIGURE A.27: Echo state Properties. Variation in the device conductance of the volatile diffusive perovskite memristor as a function of the inter-group pulse interval. The interval between the two sequences increases from (a) 10 ms, (b) 30 ms to (c) 300 ms. (d-g) Current responses when subjected to 10 identical stimulation pulses (1 V, 5 ms) with different pulse interval conditions for the final pulse. The interval varies from (d) 10 ms, (e) 23 ms, (f) 41 ms, to (g) 80 ms.

SUPPLEMENTARY NOTE 4 The echo state property of a reservoir refers to the impact that previous inputs have on the current reservoir state, and how that influence fades out with time. To test this, four short pulses of 1 V, 5 ms are applied to the device in a paired-pulse format and the device states are recorded. A non-linear accumulative behaviour is observed as a function of the paired-pulse interval. In Fig A.27a, a short paired-pulse interval of 10 ms results in an echo index (defined as $\left(\frac{a4}{a1}\right) * 100$) of 118%. Longer intervals (30 ms and 300 ms in Fig. A.27b,c) result in smaller echo indices (107.5% and 107.2% respectively), reflective of the short-term memory in the perovskite memristors. To further test the echo state property, three pulse trains consisting of 10 identical stimulation pulses (1 V, 5 ms) are applied to the device and the device states are recorded. In all cases, a non-linear accumulative behaviour is observed. As shown in Fig. A.27d-g, short intervals (≤ 23 ms) for the last stimulation pulse result in further accumulation while long intervals result in depression of the device state. This indicates that the present device state remembers the input temporal features in the recent past but not the far past, allowing the diffusive perovskite memristors to act as efficient reservoir elements.

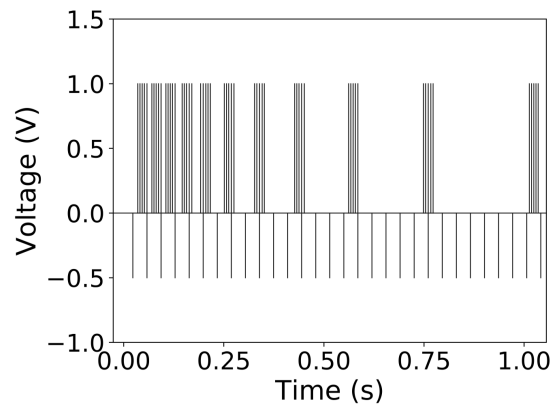


FIGURE A.28: Input waveforms. A representative "Write" (amplitude = 1 V, pulse width = 20 ms) and "Read" (amplitude = -0.5 V, pulse width = 5 ms) spike train applied to the volatile perovskite memristors in the reservoir layer.

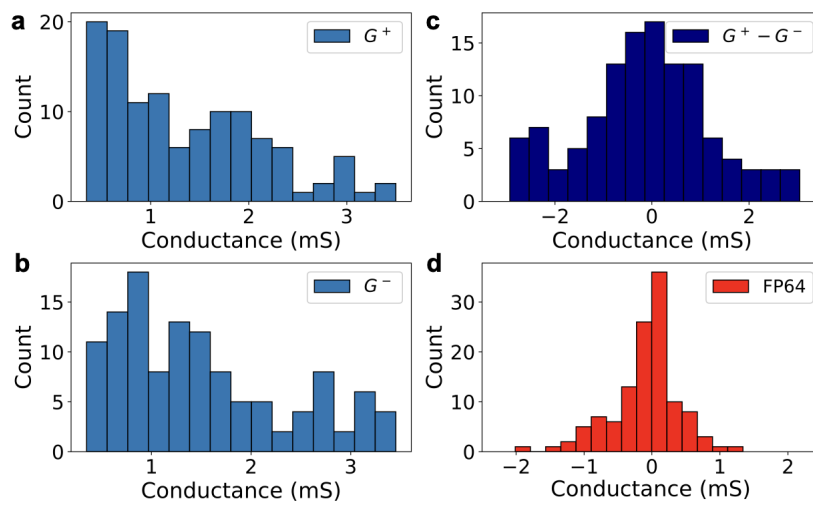


FIGURE A.29: Weight distribution. The synaptic weight distribution after training. (a-b) Conductance distribution of both positive and negative differential perovskite memristors. (c) The effective (unscaled) conductance distribution. (d) Weight distribution of the readout layer with floating-point-double precision weights. The effective memristive weights and FP64 weights follow a similar distribution.

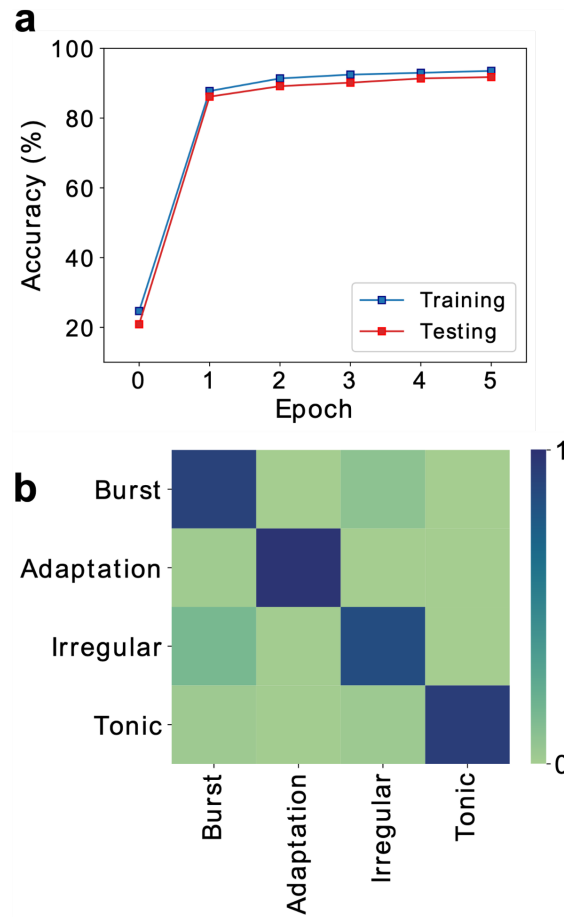
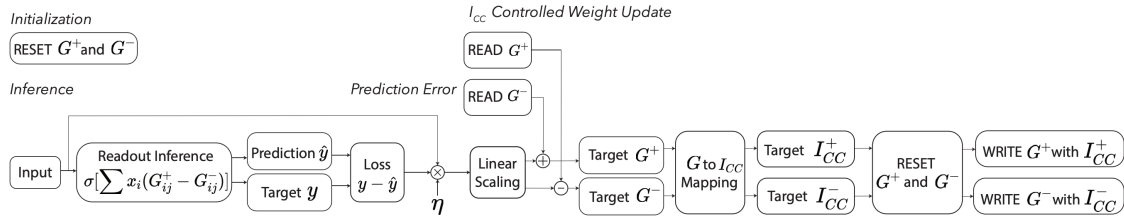


FIGURE A.30: Training RC with FP64 readout weights using backpropagation. The training metrics of ANN is shown. (a) Training and testing accuracy over 5 epochs demonstrates that the network solves the classification task with high accuracy without overfitting. (b) Confidence matrix calculated at the end of training. The correct response probability is shown in the right color scale. It is evident that network performs slightly worse in discriminating irregular patterns.

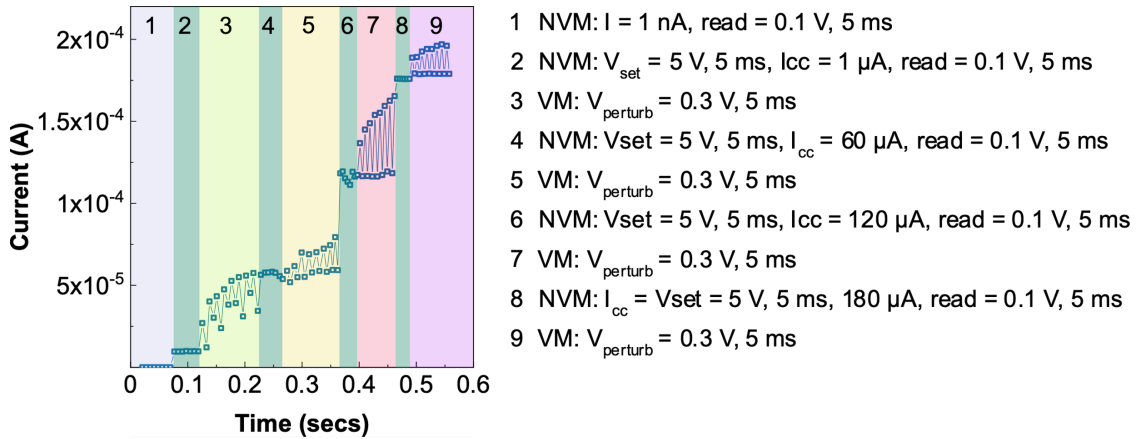
		Accuracy (%)					
		Epoch 0	Epoch 1	Epoch 2	Epoch 3	Epoch 4	Epoch 5
FP64 with Backpropagation	Training	24.68	87.76	91.38	92.47	92.99	93.54
	Testing	20.88	86.14	89.16	90.16	91.37	91.77
Perovskite with I_{cc} Control	Training	10.32	69.11	89.12	83.09	85.59	86.75
	Testing	14.46	73.29	86.14	80.92	84.94	85.14

TABLE A.1: Comparing training and test accuracies of both approaches. The neural spiking pattern classification performance table comparing the two approaches. The readout layer with drift-based halide-perovskite memristor weights trained with online (I_{cc}) control achieves comparable result with FP64 weights trained with backpropagation.

FIGURE A.31: I_{cc} modulated training for drift-based perovskite configuration.

SUPPLEMENTARY NOTE 5 During the inference procedure, reservoir output vector of length 30 is fed into the readout layer. Memristors in the readout layer are placed in the differential architecture, in which the difference of conductance values of two differential memristors (G^+ and G^-) determines the effective synaptic strength. Scaled with $\beta = 1 / (G_{\max} - G_{\min})$, where $G_{\max} = 0.35\text{mS}$ and $G_{\min} = 0.1\text{mS}$, the weight matrix (30×4) is calculated as $W = \beta [G^+ - G^-]$. And the network prediction is determined by choosing output neuron index with the maximum activation level.

For the training procedure, the network loss is calculated as the difference between output layer prediction and the one-hot encoded target vector indicating one of the four firing patterns. At this point, one can calculate targeted weights using the backpropagation algorithm. However, to support fully online-learning, we tested I_{cc} controlled weight update scheme where following stages in the pipeline can be easily implemented with the mixed-signal circuits in an event-driven manner. The I_{cc} controlled weight update is implemented as follows. First, the required weight change is calculated with $W_{\text{target}} = \eta x_i \delta_j$, where η is suitably low learning rate, x_i is the reservoir layer output and δ_j is the calculated error. In order to calculate the target conductance values for both positive and negative memristors, we first linearly scale the weight change to conductance change (by multiplying with $1/\beta$). Secondly, we read both the positive and negative conductance values. By using a push-pull mechanism, we calculate the target conductance values. The push-pull mechanism ensures a higher dynamic range in the differential configuration. Third, the target conductances are linearly mapped to the target I_{cc} values ($I_{cc, \text{target}} = (G_{\text{target}} + 1.249 \times 10^{-5}) / 3.338$) for positive and negative memristors. The weights are updated with the application of RESET and SET pulses with the targeted I_{cc} . Using the linear relation between $I_{cc} \rightarrow G$ control, we calculated mean ($\mu_G = 3.338I_{cc} - 1.294 \times 10^{-5}$) and standard deviation ($\sigma_G = 7.040I_{cc} + 3.0585$ and sample from the corresponding Normal distribution.)

FIGURE A.32: "Reconfigurability" on-the-fly of OGB-capped CsPbBr_3 NC memristors. The device is switched between its non-volatile and volatile mode on demand.

SUPPLEMENTARY NOTE 6 To demonstrate "reconfigurability" on-the-fly, our devices are switched between volatile and non-volatile modes with precise compliance current (I_{cc}) con-

trol and selection of activation voltages. Fig. A.32 shows that our devices can act as a volatile memory even after setting it to multiple non-volatile states. This proves true "reconfigurability" of our devices, hitherto undemonstrated. Such behaviour is an example of the neuromorphic implementation of synapses in Spiking Neural Networks (SNNs) that demand both volatile and non-volatile switching properties, simultaneously.

BIBLIOGRAPHY

1. McCulloch, W. S. & Pitts, W. A logical calculus of the ideas immanent in nervous activity. *Bulletin of Mathematical Biophysics* **5**, 115 (4 1943).
2. Turing, A. M. I.—computing machinery and intelligence. *Mind* **LIX**, 433 (236 1950).
3. P., H. & von Neumann, J. The computer and the brain. *Mathematical Tables and Other Aids to Computation* **13**, 226 (67 1959).
4. Tagkopoulos, I., Liu, Y.-C. & Tavazoie, S. Predictive behavior within microbial genetic networks. *Science* **320**, 1313 (5881 2008).
5. Chiang, W.-L., Zheng, L., Sheng, Y., Angelopoulos, A. N., Li, T., Li, D., Zhang, H., Zhu, B., Jordan, M., Gonzalez, J. E. & Stoica, I. Chatbot Arena: An open platform for evaluating LLMs by human preference. *arXiv [cs.AI]* (2024).
6. Marr, D. *Vision: A computational investigation into the human representation and processing of visual information* 429 pp. (MIT Press, London, England, 2010).
7. Richards, B. A., Lillicrap, T. P., Beaudoin, P., Bengio, Y., Bogacz, R., Christensen, A., Clopath, C., Costa, R. P., Berker, A. d., Ganguli, S., Gillon, C. J., Hafner, D., Kepecs, A., Kriegeskorte, N., Latham, P., Lindsay, G. W., Miller, K. D., Naud, R., Pack, C. C., Poirazi, P., Roelfsema, P., Sacramento, J., Saxe, A., Scellier, B., Schapiro, A. C., Senn, W., Wayne, G., Yamins, D., Zenke, F., Zylberberg, J., Therien, D. & Kording, K. P. A deep learning framework for neuroscience. *Nature Neuroscience* **22**, 1761 (2019).
8. Braitenberg, V. & Schüz, A. in *Cortex: Statistics and Geometry of Neuronal Connectivity* 51 (Springer Berlin Heidelberg, Berlin, Heidelberg, 1998).
9. OpenAI *et al.* GPT-4 Technical Report. *arXiv [cs.CL]* (2023).
10. Henighan, T., Kaplan, J., Katz, M., Chen, M., Hesse, C., Jackson, J., Jun, H., Brown, T. B., Dhariwal, P., Gray, S., Hallacy, C., Mann, B., Radford, A., Ramesh, A., Ryder, N., Ziegler, D. M., Schulman, J., Amodei, D. & McCandlish, S. Scaling laws for autoregressive generative modeling. *arXiv [cs.LG]* (2020).
11. Horowitz, M. 1.1 *Computing's Energy Problem (and what we can do about it)* in *2014 IEEE International Solid-State Circuits Conference Digest of Technical Papers (ISSCC) 2014 IEEE International Solid-State Circuits Conference Digest of Technical Papers (ISSCC)* (2014), 10.
12. Boroumand, A., Ghose, S., Akin, B., Narayanaswami, R., Oliveira, G. F., Ma, X., Shiu, E. & Mutlu, O. Google neural network models for edge devices: Analyzing and mitigating machine learning inference bottlenecks in 2021 30th International Conference on Parallel Architectures and Compilation Techniques (PACT) 2021 30th International Conference on Parallel Architectures and Compilation Techniques (PACT)Atlanta, GA, USA (IEEE, 2021), 159.
13. Chua, L. Memristor-The missing circuit element. *IEEE Trans. Circuit Theory* **18**, 507 (5 1971).
14. Le Gallo, M., Sebastian, A., Mathis, R., Manica, M., Giefers, H., Tuma, T., Bekas, C., Curioni, A. & Eleftheriou, E. Mixed-precision in-memory computing. *Nat. Electron.* **1**, 246 (4 2018).
15. Bartol, T. M., Bromer, C., Kinney, J., Chirillo, M. A., Bourne, J. N., Harris, K. M. & Sejnowski, T. J. Nanoconnectomic upper bound on the variability of synaptic plasticity. *Elife* **4**, e10778 (2015).
16. Burr, G. W., Shelby, R. M., Sebastian, A., Kim, S., Kim, S., Sidler, S., Virwani, K., Ishii, M., Narayanan, P., Fumarola, A., Sanches, L. L., Boybat, I., Le Gallo, M., Moon, K., Woo, J., Hwang, H. & Leblebici, Y. Neuromorphic computing using non-volatile memory. *Adv. Phys. X.* **2**, 89 (1 2017).
17. Demirag, Y. *Multiphysics modeling of Ge₂Sb₂Te₅ based synaptic devices for brain inspired computing* MA thesis (Ihsan Dogramaci Bilkent University, Ankara, Turkey, 2018).

18. Wan, W., Kubendran, R., Schaefer, C., Eryilmaz, S. B., Zhang, W., Wu, D., Deiss, S., Raina, P., Qian, H., Gao, B., *et al.* A compute-in-memory chip based on resistive random-access memory. *Nature* **608**, 504 (2022).
19. Chanthbouala, A., Garcia, V., Cherifi, R. O., Bouzehouane, K., Fusil, S., Moya, X., Xavier, S., Yamada, H., Deranlot, C., Mathur, N. D., Bibes, M., Barthélémy, A. & Grollier, J. A ferroelectric memristor. *Nat. Mater.* **11**, 860 (10 2012).
20. Lu, S. & Sengupta, A. Exploring the connection between binary and Spiking Neural Networks. *Front. Neurosci.* **14**, 535 (2020).
21. John, R. A., Acharya, J., Zhu, C., Surendran, A., Bose, S. K., Chaturvedi, A., Tiwari, N., Gao, Y., He, Y., Zhang, K. K., Xu, M., Leong, W. L., Liu, Z., Basu, A. & Mathews, N. Optogenetics inspired transition metal dichalcogenide neuristors for in-memory deep recurrent neural networks. *Nat. Commun.* **11**, 3211 (1 2020).
22. Sidler, S., Boybat, I., Shelby, R. M., Narayanan, P., Jang, J., Fumarola, A., Moon, K., Leblebici, Y., Hwang, H. & Burr, G. W. *Large-scale neural networks implemented with Non-Volatile Memory as the synaptic weight element: Impact of conductance response in 2016 46th European Solid-State Device Research Conference (ESSDERC) ESSDERC 2016 - 46th European Solid-State Device Research Conference* Lausanne, Switzerland (IEEE, 2016), 440.
23. Khaddam-Aljameh, R., Stanisavljevic, M., Mas, J. F., Karunaratne, G., Brändli, M., Liu, F., Singh, A., Müller, S. M., Egger, U., Petropoulos, A., Antonakopoulos, T., Brew, K., Choi, S., Ok, I., Lie, F. L., Saulnier, N., Chan, V., Ahsan, I., Narayanan, V., Nandakumar, S. R., Le Gallo, M., Francese, P. A., Sebastian, A. & Eleftheriou, E. HERMES-Core-A 1.59-TOPS/mm² PCM on 14-nm CMOS In-Memory Compute Core Using 300-ps/LSB Linearized CCO-Based ADCs. *IEEE J. Solid-State Circuits*, 1 (2022).
24. Berdan, R., Vasilaki, E., Khiat, A., Indiveri, G., Serb, A. & Prodromakis, T. Emulating short-term synaptic dynamics with memristive devices. *Sci. Rep.* **6**, 18639 (1 2016).
25. Ohno, T., Hasegawa, T., Tsuruoka, T., Terabe, K., Gimzewski, J. K. & Aono, M. Short-term plasticity and long-term potentiation mimicked in single inorganic synapses. *Nat. Mater.* **10**, 591 (8 2011).
26. Zhang, X., Wang, W., Liu, Q., Zhao, X., Wei, J., Cao, R., Yao, Z., Zhu, X., Zhang, F., Lv, H., Long, S. & Liu, M. An artificial neuron based on a threshold switching memristor. *IEEE Electron Device Lett.* **39**, 308 (2 2018).
27. Huang, H.-M., Yang, R., Tan, Z.-H., He, H.-K., Zhou, W., Xiong, J. & Guo, X. Quasi-Hodgkin-Huxley neurons with leaky integrate-and-fire functions physically realized with memristive devices. *Adv. Mater.* **31**, e1803849 (3 2019).
28. Dalgaty, T., Moro, F., Demirag, Y., De Pra, A., Indiveri, G., Vianello, E. & Payvand, M. Mosaic: in-memory computing and routing for small-world spike-based neuromorphic systems. *Nat. Commun.* **15**, 1 (1 2024).
29. Indiveri, G., Linares-Barranco, B., Hamilton, T., van Schaik, A., Etienne-Cummings, R., Delbruck, T., Liu, S.-C., Dudek, P., Häfliger, P., Renaud, S., Schemmel, J., Cauwenberghs, G., Arthur, J., Hynna, K., Folorosele, F., Saighi, S., Serrano-Gotarredona, T., Wijekoon, J., Wang, Y. & Boahen, K. Neuromorphic silicon neuron circuits. *Frontiers in Neuroscience* **5**, 1 (2011).
30. Sterling, P. in *Principles of Neural Design* 155 (The MIT Press, 2015).
31. Liu, S.-C., Van Schaik, A., Minch, B. A. & Delbruck, T. *Event-based 64-channel binaural silicon cochlea with Q enhancement mechanisms in 2010 IEEE International Symposium on Circuits and Systems (ISCAS)* (2010), 2027.
32. Rueckauer, B. & Delbruck, T. Evaluation of event-based algorithms for optical flow with ground-truth from inertial measurement sensor. *Front. Neurosci.* **10**, 176 (2016).
33. Mahowald, M. *VLSI analogs of neuronal visual processing: a synthesis of form and function* (1992).
34. Boahen, K. Dendrocentric learning for synthetic intelligence. *Nature* **612**, 43 (7938 2022).

35. Kubke, M. F., Massoglia, D. P. & Carr, C. E. Developmental changes underlying the formation of the specialized time coding circuits in barn owls (*Tyto alba*). *J. Neurosci.* **22**, 7671 (17 2002).
36. O'Keefe, J. & Recce, M. L. Phase relationship between hippocampal place units and the EEG theta rhythm. *Hippocampus* **3**, 317 (3 1993).
37. MacKay, D. M. & McCulloch, W. S. The limiting information capacity of a neuronal link. *Bulletin of Mathematical Biophysics* **14**, 127 (2 1952).
38. Aceituno, P. V., de Haan, S., Loidl, R. & Grewe, B. F. Hierarchical target learning in the mammalian neocortex: A pyramidal neuron perspective. *bioRxiv* (2024).
39. Payeur, A., Guerguiev, J., Zenke, F., Richards, B. A. & Naud, R. Burst-dependent synaptic plasticity can coordinate learning in hierarchical circuits. *bioRxiv* (2020).
40. Gerstner, W., Kempter, R., van Hemmen, J. L. & Wagner, H. A neuronal learning rule for sub-millisecond temporal coding. *Nature* **383**, 76 (6595 1996).
41. Demirag, Y. & Indiveri, G. *Network of biologically plausible neuron models can solve motor tasks through heterogeneity in Computational and Systems Neuroscience (COSYNE)* (Lisbon, Portugal, 2024).
42. Hardtdegen, A., La Torre, C., Cuppers, F., Menzel, S., Waser, R. & Hoffmann-Eifert, S. Improved switching stability and the effect of an internal series resistor in HfO₂/TiO₂ bilayer ReRAM cells. *IEEE Trans. Electron Devices* **65**, 3229 (8 2018).
43. Nandakumar, S. R., Boybat, I., Han, J.-P., Ambrogio, S., Adusumilli, P., Bruce, R. L., Bright-Sky, M., Rasch, M., Le Gallo, M. & Sebastian, A. *Precision of synaptic weights programmed in phase-change memory devices for deep learning inference in 2020 IEEE International Electron Devices Meeting (IEDM) 2020 IEEE International Electron Devices Meeting (IEDM)* San Francisco, CA, USA (IEEE, 2020), 29.4.1.
44. Gong, N., Idé, T., Kim, S., Boybat, I., Sebastian, A., Narayanan, V. & Ando, T. Signal and noise extraction from analog memory elements for neuromorphic computing. *Nat. Commun.* **9**, 2102 (1 2018).
45. Gallo, M. L., Kaes, M., Sebastian, A. & Krebs, D. Subthreshold electrical transport in amorphous phase-change materials. *New Journal of Physics* **17**, 093035 (2015).
46. Burr, G., Shelby, R., Nolfo, C., Jang, J., Shenoy, R., Narayanan, P., Virwani, K., Giacometti, E., Kurdi, B. & Hwang, H. Experimental Demonstration and Tolerancing of a Large-Scale Neural Network (165,000 Synapses), using Phase-Change Memory as the Synaptic Weight Element. *2014 IEEE International Electron Devices Meeting*, 1 (2014).
47. Stathopoulos, S., Khiat, A., Trapatseli, M., Cortese, S., Serb, A., Valov, I. & Prodromakis, T. Multibit memory operation of metal-oxide bi-layer memristors. *Scientific reports* **7**, 17532 (2017).
48. Prezioso, M., Merrih-Bayat, F., Hoskins, B., Adam, G. C., Likharev, K. K. & Strukov, D. B. Training and operation of an integrated neuromorphic network based on metal-oxide memristors. *Nature* **521**, 61 (2015).
49. Bayat, F. M., Prezioso, M., Chakrabarti, B., Nili, H., Kataeva, I. & Strukov, D. Implementation of multilayer perceptron network with highly uniform passive memristive crossbar circuits. *Nature communications* **9**, 2331 (2018).
50. Li, C., Hu, M., Li, Y., Jiang, H., Ge, N., Montgomery, E., Zhang, J., Song, W., Dávila, N., Graves, C. E., *et al.* Analogue signal and image processing with large memristor crossbars. *Nature Electronics* **1**, 52 (2018).
51. Boybat, I., Le Gallo, M., Nandakumar, S., Moraitis, T., Parnell, T., Tuma, T., Rajendran, B., Leblebici, Y., Sebastian, A. & Eleftheriou, E. Neuromorphic computing with multi-memristive synapses. *Nature communications* **9**, 2514 (2018).

52. Agarwal, S., Jacobs Gedrim, R. B., Hsia, A. H., Hughart, D. R., Fuller, E. J., Alec Talin, A., James, C. D., Plimpton, S. J. & Marinella, M. J. *Achieving ideal accuracies in analog neuromorphic computing using periodic carry in 2017 Symposium on VLSI Technology (IEEE, 2017)*, T174.
53. Suri, M., Bichler, O., Querlioz, D., Palma, G., Vianello, E., Vuillaume, D., Gamrat, C. & DeSalvo, B. *CBRAM devices as binary synapses for low-power stochastic neuromorphic systems: auditory (cochlea) and visual (retina) cognitive processing applications in 2012 International Electron Devices Meeting (2012)*, 10.
54. Payvand, M., Muller, L. K. & Indiveri, G. *Event-based circuits for controlling stochastic learning with memristive devices in neuromorphic architectures in 2018 IEEE International Symposium on Circuits and Systems (ISCAS) (2018)*, 1.
55. Ambrogio, S., Narayanan, P., Tsai, H., Shelby, R. M., Boybat, I., di Nolfo, C., Sidler, S., Giordano, M., Bodini, M., Farinha, N. C., *et al.* Equivalent-accuracy accelerated neural-network training using analogue memory. *Nature* **558**, 60 (2018).
56. Lillicrap, T. P. & Santoro, A. Backpropagation through time and the brain. *Curr. Opin. Neurobiol. Machine Learning, Big Data, and Neuroscience* **55**, 82 (2019).
57. Attneave, F. & Hebb, D. O. The organization of behavior; A neuropsychological theory. *Am. J. Psychol.* **63**, 633 (4 1950).
58. Sjöström, P. J., Turrigiano, G. G. & Nelson, S. B. Rate, timing, and cooperativity jointly determine cortical synaptic plasticity. *Neuron* **32**, 1149 (6 2001).
59. Feldman, D. E. The spike-timing dependence of plasticity. *Neuron* **75**, 556 (4 2012).
60. Oja, E. A simplified neuron model as a principal component analyzer. *J. Math. Biol.* **15**, 267 (3 1982).
61. Frenkel, C., Lefebvre, M., Legat, J.-D. & Bol, D. A 0.086-mm² 12.7-pJ/SOP 64k-Synapse 256-Neuron Online-Learning Digital Spiking Neuromorphic Processor in 28-nm CMOS. *IEEE Trans. Biomed. Circuits Syst.* **13**, 145 (1 2019).
62. Frenkel, C., Legat, J.-D. & Bol, D. MorphIC: A 65-nm 738k-synapse/mm² quad-core binary-weight digital neuromorphic processor with stochastic spike-driven online learning. *arXiv [cs.NE]* (2019).
63. Mayr, C., Partzsch, J., Noack, M., Hänzsche, S., Scholze, S., Höppner, S., Ellguth, G. & Schüffny, R. A biological-realtime neuromorphic system in 28 nm CMOS using low-leakage switched capacitor circuits. *IEEE Trans. Biomed. Circuits Syst.* **10**, 243 (1 2016).
64. Brader, J. M., Senn, W. & Fusi, S. Learning real-world stimuli in a neural network with spike-driven synaptic dynamics. *Neural computation* **19**, 2881 (2007).
65. Marblestone, A. H., Wayne, G. & Kording, K. P. Toward an integration of deep learning and neuroscience. *Front. Comput. Neurosci.* **10**, 94 (2016).
66. Laskin, M., Metz, L., Nabarro, S., Saroufim, M., Noune, B., Luschi, C., Sohl-Dickstein, J. & Abbeel, P. Parallel training of deep networks with local updates. *arXiv [cs.LG]* (2020).
67. Kaiser, J., Mostafa, H. & Neftci, E. Synaptic plasticity dynamics for Deep Continuous Local Learning (DECOLLE). *Front. Neurosci.* **14**, 424 (2020).
68. Rumelhart, D. E., Hinton, G. E. & Williams, R. J. Learning representations by back-propagating errors. *Nature* **323**, 533 (6088 1986).
69. Lillicrap, T. P., Cownden, D., Tweed, D. B. & Akerman, C. J. Random synaptic feedback weights support error backpropagation for deep learning. *Nat. Commun.* **7**, 13276 (1 2016).
70. Pozzi, I., Bohté, S. & Roelfsema, P. A biologically plausible learning rule for deep learning in the brain. *arXiv [cs.NE]* (2018).
71. Lee, D.-H., Zhang, S., Fischer, A. & Bengio, Y. Difference Target Propagation. *arXiv [cs.LG]* (2014).
72. Millidge, B., Tschantz, A. & Buckley, C. L. Predictive Coding Approximates Backprop along Arbitrary Computation Graphs. *arXiv* (2020).

73. Baydin, A. G., Pearlmutter, B. A., Syme, D., Wood, F. & Torr, P. Gradients without Back-propagation. *arXiv [cs.LG]* (2022).
74. Liu, Y. H., Ghosh, A., Richards, B. A., Shea-Brown, E. & Lajoie, G. Beyond accuracy: generalization properties of bio-plausible temporal credit assignment rules. *arXiv [cs.NE]* (2022).
75. Bellec, G., Scherr, F., Subramoney, A., Hajek, E., Salaj, D., Legenstein, R. & Maass, W. A solution to the learning dilemma for recurrent networks of spiking neurons. *Nature Communications* **11**, 1 (2020).
76. Nagel, M., Fournarakis, M., Amjad, R. A., Bondarenko, Y., van Baalen, M. & Blankevoort, T. A white paper on neural network quantization. *arXiv [cs.LG]* (2021).
77. Frenkel, C. & Indiveri, G. ReckOn: A 28nm sub-mm² task-agnostic spiking recurrent neural network processor enabling on-chip learning over second-long timescales. *arXiv [cs.NE]* (2022).
78. Lee, J., Kim, D. & Ham, B. Network quantization with element-wise gradient scaling. *arXiv [cs.CV]* (2021).
79. Fournarakis, M. & Nagel, M. In-Hindsight Quantization Range Estimation for Quantized Training. *2021 IEEE/CVF Conference on Computer Vision and Pattern Recognition Workshops (CVPRW)*, 3057 (2021).
80. Bernstein, J., Zhao, J., Meister, M., Liu, M.-Y., Anandkumar, A. & Yue, Y. Learning compositional functions via multiplicative weight updates. *arXiv [cs.NE]* (2020).
81. Nandakumar, S., Le Gallo, M., Boybat, I., Rajendran, B., Sebastian, A. & Eleftheriou, E. A phase-change memory model for neuromorphic computing. *Journal of Applied Physics* **124**, 152135 (2018).
82. Bellec, G., Salaj, D., Subramoney, A., Legenstein, R. & Maass, W. Long short-term memory and learning-to-learn in networks of spiking neurons in *Advances in Neural Information Processing Systems* (2018), 787.
83. Zenke, F. & Neftci, E. O. Brain-Inspired Learning on Neuromorphic Substrates. *Proceedings of the IEEE*, 1 (2021).
84. Bohnstingl, T., Woźniak, S., Maass, W., Pantazi, A. & Eleftheriou, E. Online Spatio-Temporal Learning in Deep Neural Networks. *arXiv* (2020).
85. Zenke, F. & Ganguli, S. Superspike: Supervised learning in multilayer spiking neural networks. *Neural computation* **30**, 1514 (2018).
86. Perez-Nieves, N. & Goodman, D. F. M. Sparse Spiking Gradient Descent. *arXiv* (2021).
87. Singh, S. P. & Sutton, R. S. Reinforcement Learning with Replacing Eligibility Traces. *Mach. Learn.* **22**, 123 (1/2/3 1996).
88. Hull, C. L. Principles of Behavior. *The Journal of Nervous and Mental Disease* **101**, 396 (4 1945).
89. Davies, M., Srinivasa, N., Lin, T.-H., Chinya, G., Cao, Y., Choday, S. H., Dimou, G., Joshi, P., Imam, N., Jain, S., Liao, Y., Lin, C.-K., Lines, A., Liu, R., Mathaikutty, D., McCoy, S., Paul, A., Tse, J., Venkataramanan, G., Weng, Y.-H., Wild, A., Yang, Y. & Wang, H. Loihi: A neuromorphic manycore processor with on-chip learning. *IEEE Micro* **38**, 82 (2018).
90. Grübl, A., Billaudelle, S., Cramer, B., Karasenko, V. & Schemmel, J. Verification and Design Methods for the BrainScaleS Neuromorphic Hardware System. *arXiv preprint arXiv:2003.11455* (2020).
91. Furber, S., Galluppi, F., Temple, S. & Plana, L. The SpiNNaker Project. *Proceedings of the IEEE* **102**, 652 (2014).
92. Backus, J. Can programming be liberated from the von Neumann style?: a functional style and its algebra of programs. *Communications of the ACM* **21**, 613 (1978).
93. Indiveri, G. & Liu, S.-C. Memory and information processing in neuromorphic systems. *Proceedings of the IEEE* **103**, 1379 (2015).

94. Rubino, A., Livanelioglu, C., Qiao, N., Payvand, M. & Indiveri, G. Ultra-low-power FDSOI neural circuits for extreme-edge neuromorphic intelligence. *IEEE Trans. Circuits Syst. I Regul. Pap.* **68**, 45 (1 2021).
95. Fuller, E. J., Keene, S. T., Melianas, A., Wang, Z., Agarwal, S., Li, Y., Tuchman, Y., James, C. D., Marinella, M. J., Yang, J. J., Salleo, A. & Talin, A. A. Parallel programming of an ionic floating-gate memory array for scalable neuromorphic computing. *Science* **364**, 570 (6440 2019).
96. Huang, Y.-J., Chao, S.-C., Lien, D., Wen, C., He, J.-H. & Lee, S.-C. Dual-functional memory and threshold resistive switching based on the push-pull mechanism of oxygen ions. *Sci. Rep.* **6**, 23945 (1 2016).
97. Abbas, H., Abbas, Y., Hassan, G., Sokolov, A. S., Jeon, Y.-R., Ku, B., Kang, C. J. & Choi, C. The coexistence of threshold and memory switching characteristics of ALD HfO₂ memristor synaptic arrays for energy-efficient neuromorphic computing. *Nanoscale* **12**, 14120 (26 2020).
98. Kaplan, J., McCandlish, S., Henighan, T., Brown, T. B., Chess, B., Child, R., Gray, S., Radford, A., Wu, J. & Amodei, D. Scaling laws for neural language models. *arXiv [cs.LG]* (2020).
99. Prezioso, M., Merrih-Bayat, F., Hoskins, B., Adam, G., Likharev, K. K. & Strukov, D. B. Training and operation of an integrated neuromorphic network based on metal-oxide memristors. *Nature* **521**, 61 (2015).
100. Yao, P., Wu, H., Gao, B., Tang, J., Zhang, Q., Zhang, W., Yang, J. J. & Qian, H. Fully hardware-implemented memristor convolutional neural network. *Nature* **577**, 641 (2020).
101. Chen, J., Yang, S., Wu, H., Indiveri, G. & Payvand, M. Scaling Limits of Memristor-Based Routers for Asynchronous Neuromorphic Systems. *arXiv preprint arXiv:2307.08116* (2023).
102. Vianello, E. & Payvand, M. Scaling neuromorphic systems with 3D technologies. *Nat. Electron.* **7**, 419 (6 2024).
103. Moradi, S., Qiao, N., Stefanini, F. & Indiveri, G. A Scalable Multicore Architecture With Heterogeneous Memory Structures for Dynamic Neuromorphic Asynchronous Processors (DYNAPs). *Biomedical Circuits and Systems, IEEE Transactions on* **12**, 106 (2018).
104. Sutton, R. S. *The Bitter Lesson* (2024).
105. Ielmini, D. Resistive switching memories based on metal oxides: mechanisms, reliability and scaling. *Semiconductor Science and Technology* **31**, 063002 (2016).
106. Widrow, B. & Winter, R. Neural nets for adaptive filtering and adaptive pattern recognition. *Computer* **21**, 25 (1988).
107. Paszke, A., Gross, S., Massa, F., Lerer, A., Bradbury, J., Chanan, G., Killeen, T., Lin, Z., Gimelshein, N., Antiga, L., Desmaison, A., Kopf, A., Yang, E., DeVito, Z., Raison, M., Tejani, A., Chilamkurthy, S., Steiner, B., Fang, L., Bai, J. & Chintala, S. in *Advances in Neural Information Processing Systems* 32 (eds Wallach, H., Larochelle, H., Beygelzimer, A., d'Alché-Buc, F., Fox, E. & Garnett, R.) 8024 (Curran Associates, Inc., 2019).
108. Bernstein, J., Wang, Y.-X., Azizzadenesheli, K. & Anandkumar, A. signSGD: Compressed Optimisation for Non-Convex Problems. *arXiv [cs.LG]* (2018).
109. Boybat, I., Gallo, M. L., Moraitis, T., Parnell, T., Tuma, T., Rajendran, B., Leblebici, Y., Sebastian, A. & Eleftheriou, E. Neuromorphic computing with multi-memristive synapses. *Nature Communications* **9**, 2514 (2018).
110. Nandakumar, S. R., Gallo, M. L., Piveteau, C., Joshi, V., Mariani, G., Boybat, I., Karunaratne, G., Khaddam-Aljameh, R., Egger, U., Petropoulos, A., Antonakopoulos, T., Rajendran, B., Sebastian, A. & Eleftheriou, E. Mixed-Precision Deep Learning Based on Computational Memory. *Frontiers in Neuroscience* **14**, 406 (2020).
111. Hubara, I., Courbariaux, M., Soudry, D., El-Yaniv, R. & Bengio, Y. Quantized Neural Networks: Training Neural Networks with Low Precision Weights and Activations. *arXiv* (2016).

112. Le Gallo, M., Krebs, D., Zipoli, F., Salinga, M. & Sebastian, A. Collective Structural Relaxation in Phase-Change Memory Devices. *Advanced Electronic Materials* **4**, 1700627 (2018).
113. Salimans, T., Ho, J., Chen, X., Sidor, S. & Sutskever, I. Evolution Strategies as a Scalable Alternative to Reinforcement Learning. *arXiv* (2017).
114. Indiveri, G., Linares-Barranco, B., Legenstein, R., Deligeorgis, G. & Prodromakis, T. Integration of nanoscale memristor synapses in neuromorphic computing architectures. *Nanotechnology* **24**, 384010 (2013).
115. Payvand, M., Nair, M. V., Müller, L. K. & Indiveri, G. A neuromorphic systems approach to in-memory computing with non-ideal memristive devices: From mitigation to exploitation. *Faraday Discussions* **213**, 487 (2019).
116. Deiss, S., Douglas, R. & Whatley, A. in *Pulsed Neural Networks* (eds Maass, W. & Bishop, C.) 157 (MIT Press, 1998).
117. Alibart, F., Gao, L., Hoskins, B. D. & Strukov, D. B. High precision tuning of state for memristive devices by adaptable variation-tolerant algorithm. *Nanotechnology* **23**, 075201 (2012).
118. Nandakumar, S., Le Gallo, M., Boybat, I., Rajendran, B., Sebastian, A. & Eleftheriou, E. *Mixed-precision architecture based on computational memory for training deep neural networks in 2018 IEEE International Symposium on Circuits and Systems (ISCAS)* (2018), 1.
119. Grossi, A., Nowak, E., Zambelli, C., Pellissier, C., Bernasconi, S., Cibrario, G., Hajjam, K. E., Crochemore, R., Nodin, J. F., Olivo, P. & Perniola, L. *Fundamental variability limits of filament-based RRAM in 2016 IEEE International Electron Devices Meeting (IEDM)* (2016), 4.7.1.
120. Payvand, M. & Indiveri, G. *Spike-Based Plasticity Circuits for Always-on On-Line Learning in Neuromorphic Systems in 2019 IEEE International Symposium on Circuits and Systems (ISCAS)* (IEEE, Sapporo, Japan, 2019), 1.
121. Delbruck, T. 'Bump' circuits for computing similarity and dissimilarity of analog voltages in *Neural Networks, 1991., IJCNN-91-Seattle International Joint Conference on* **1** (1991), 475.
122. Payvand, M., Fouda, M., Kurdahi, F., Eltawil, A. & Neftci, E. O. Error-triggered Three-Factor Learning Dynamics for Crossbar Arrays. *arXiv preprint arXiv:1910.06152* (2019).
123. Goodman, D. Brian: a simulator for spiking neural networks in Python. *Frontiers in Neuroinformatics* **2** (2008).
124. Lecun, Y., Bottou, L., Bengio, Y. & Haffner, P. Gradient-based learning applied to document recognition. *Proceedings of the IEEE* **86**, 2278 (1998).
125. Dalgaty, T., Payvand, M., Moro, F., Ly, D. R., Pebay-Peyroula, F., Casas, J., Indiveri, G. & Vianello, E. Hybrid neuromorphic circuits exploiting non-conventional properties of RRAM for massively parallel local plasticity mechanisms. *APL Materials* **7**, 081125 (2019).
126. Demirag, Y., Frenkel, C., Payvand, M. & Indiveri, G. *Online training of spiking recurrent neural networks with Phase-Change Memory synapses* 2021.
127. Demirag, Y., Moro, F., Dalgaty, T., Navarro, G., Frenkel, C., Indiveri, G., Vianello, E. & Payvand, M. *PCM-trace: Scalable synaptic eligibility traces with resistivity drift of phase-change materials in 2021 IEEE International Symposium on Circuits and Systems (ISCAS)* 2021 IEEE International Symposium on Circuits and Systems (ISCAS)Daegu, Korea. **00** (IEEE, 2021), 1.
128. Bohnstingl, T., Surina, A., Fabre, M., Demirag, Y., Frenkel, C., Payvand, M., Indiveri, G. & Pantazi, A. *Biologically-inspired training of spiking recurrent neural networks with neuromorphic hardware in 2022 IEEE 4th International Conference on Artificial Intelligence Circuits and Systems (AICAS)* 2022 IEEE 4th International Conference on Artificial Intelligence Circuits and Systems (AICAS)Incheon, Korea, Republic of. **00** (IEEE, 2022), 218.
129. Khrulkov, V., Novikov, A. & Oseledets, I. Expressive power of recurrent neural networks. *arXiv* (2017).

130. Oord, A. v. d., Dieleman, S., Zen, H., Simonyan, K., Vinyals, O., Graves, A., Kalchbrenner, N., Senior, A. & Kavukcuoglu, K. WaveNet: A Generative Model for Raw Audio. *arXiv:1609.03499 [cs]* (2016).
131. Teed, Z. & Deng, J. RAFT: Recurrent All-Pairs Field Transforms for Optical Flow. *arXiv* (2020).
132. Brown, T. B., Mann, B., Ryder, N., Subbiah, M., Kaplan, J., Dhariwal, P., Neelakantan, A., Shyam, P., Sastry, G., Askell, A., Agarwal, S., Herbert-Voss, A., Krueger, G., Henighan, T., Child, R., Ramesh, A., Ziegler, D. M., Wu, J., Winter, C., Hesse, C., Chen, M., Sigler, E., Litwin, M., Gray, S., Chess, B., Clark, J., Berner, C., McCandlish, S., Radford, A., Sutskever, I. & Amodei, D. Language Models are Few-Shot Learners. *arXiv* (2020).
133. Berner, C., Brockman, G., Chan, B., Cheung, V., Dennison, C., Farhi, D., Fischer, Q., Hashme, S., Hesse, C., Józefowicz, R., Gray, S., Olsson, C., Pachocki, J., Petrov, M., Salimans, T., Schlatter, J., Schneider, J., Sidor, S., Sutskever, I., Tang, J., Wolski, F. & Zhang, S. Dota 2 with Large Scale Deep Reinforcement Learning, 66 (2019).
134. Ha, D. & Schmidhuber, J. World Models. *arXiv:1803.10122 [cs, stat]* (2018).
135. Vinyals, O., Babuschkin, I., Czarnecki, W. M., Mathieu, M., Dudzik, A., Chung, J., Choi, D. H., Powell, R., Ewalds, T., Georgiev, P., Oh, J., Horgan, D., Kroiss, M., Danihelka, I., Huang, A., Sifre, L., Cai, T., Agapiou, J. P., Jaderberg, M., Vezhnevets, A. S., Leblond, R., Pohlen, T., Dalibard, V., Budden, D., Sulsky, Y., Molloy, J., Paine, T. L., Gulcehre, C., Wang, Z., Pfaff, T., Wu, Y., Ring, R., Yogatama, D., Wünsch, D., McKinney, K., Smith, O., Schaul, T., Lillicrap, T., Kavukcuoglu, K., Hassabis, D., Apps, C. & Silver, D. Grandmaster level in StarCraft II using multi-agent reinforcement learning. *Nature* **575**, 350 (2019).
136. Douglas, R. & Martin, K. in *The synaptic organization of the brain* (ed Shepherd, G.) 4th, 459 (Oxford University Press, Oxford, New York, 1998).
137. Douglas, R., Mahowald, M. & Mead, C. Neuromorphic analogue VLSI. *Annual Review of Neuroscience* **18**, 255 (1995).
138. Ambrogio, S., Narayanan, P., Tsai, H., Shelby, R. M., Boybat, I., di Nolfo, C., Sidler, S., Giordano, M., Bodini, M., Farinha, N. C. P., Killeen, B., Cheng, C., Jaoudi, Y. & Burr, G. W. Equivalent-accuracy accelerated neural-network training using analogue memory. *Nature* **558**, 60 (2018).
139. Li, C., Belkin, D., Li, Y., Yan, P., Hu, M., Ge, N., Jiang, H., Montgomery, E., Lin, P., Wang, Z., Song, W., Strachan, J. P., Barnell, M., Wu, Q., Williams, R. S., Yang, J. J. & Xia, Q. Efficient and self-adaptive in-situ learning in multilayer memristor neural network. *Nature Communications* **9**, 1 (2018).
140. Dalgaty, T., Castellani, N., Turck, C., Harabi, K.-E., Querlioz, D. & Vianello, E. In situ learning using intrinsic memristor variability via Markov chain Monte Carlo sampling. *Nature Electronics* **4**, 151 (2021).
141. Cai, F., Kumar, S., Van Vaerenbergh, T., Sheng, X., Liu, R., Li, C., Liu, Z., Foltin, M., Yu, S., Xia, Q., *et al.* Power-efficient combinatorial optimization using intrinsic noise in memristor Hopfield neural networks. *Nature Electronics* **3**, 409 (2020).
142. Sebastian, A., Gallo, M. L. & Eleftheriou, E. Computational phase-change memory: beyond von Neumann computing. *Journal of Physics D: Applied Physics* **52**, 443002 (2019).
143. Payvand, M., Nair, M. V., Müller, L. K. & Indiveri, G. A neuromorphic systems approach to in-memory computing with non-ideal memristive devices: From mitigation to exploitation. *Faraday Discussions* **213**, 487 (2019).
144. Chicca, E. & Indiveri, G. A recipe for creating ideal hybrid memristive-CMOS neuromorphic processing systems. *Applied Physics Letters* **116**, 120501 (2020).
145. Peng, X., Huang, S., Luo, Y., Sun, X. & Yu, S. DNN+NeuroSim: An End-to-End Benchmarking Framework for Compute -in-Memory Accelerators with Versatile Device Technologies. *IEEE International Electron Devices Meeting (IEDM)*, 32.5.1 (2019).

146. Peng, X., Huang, S., Jiang, H., Lu, A. & Yu, S. DNN+NeuroSim V2.0: An End-to-End Benchmarking Framework for Compute-in-Memory Accelerators for On-chip Training. *IEEE Transactions on Computer-Aided Design of Integrated Circuits and Systems* **PP**, 1 (2020).
147. Burr, G. W., Brightsky, M. J., Sebastian, A., Cheng, H.-Y., Wu, J.-Y., Kim, S., Sosa, N. E., Papandreou, N., Lung, H.-L., Pozidis, H., Eleftheriou, E. & Lam, C. H. Recent Progress in Phase-Change Memory Technology. *IEEE Journal on Emerging and Selected Topics in Circuits and Systems* **6**, 146 (2016).
148. Burr, G. W., Shelby, R. M., Sebastian, A., Kim, S., Kim, S., Sidler, S., Virwani, K., Ishii, M., Narayanan, P., Fumarola, A., Sanches, L. L., Boybat, I., Le Gallo, M., Moon, K., Woo, J., Hwang, H. & Leblebici, Y. Neuromorphic computing using non-volatile memory. *Advances in Physics: X* **2**, 89 (2017).
149. Tuma, T., Pantazi, A., Le Gallo, M., Sebastian, A. & Eleftheriou, E. Stochastic phase-change neurons. *Nature Nanotechnology* **11**, 693 (2016).
150. Karunaratne, G., Gallo, M. L., Cherubini, G., Benini, L., Rahimi, A. & Sebastian, A. In-memory hyperdimensional computing. *Nature Electronics* **3**, 327 (2020).
151. Demirag, Y., Moro, F., Dalgaty, T., Navarro, G., Frenkel, C., Indiveri, G., Vianello, E. & Payvand, M. PCM-trace: Scalable Synaptic Eligibility Traces with Resistivity Drift of Phase-Change Materials. *2021 IEEE International Symposium on Circuits and Systems (ISCAS)*, 1 (2021).
152. Gallo, M. L., Sebastian, A., Cherubini, G., Giefers, H. & Eleftheriou, E. Compressed Sensing With Approximate Message Passing Using In-Memory Computing. *IEEE Transactions on Electron Devices* **65**, 4304 (2018).
153. Gallo, M. L. & Sebastian, A. An overview of phase-change memory device physics. *Journal of Physics D: Applied Physics* **53**, 213002 (2020).
154. Gallo, M. L., Athmanathan, A., Krebs, D. & Sebastian, A. Evidence for thermally assisted threshold switching behavior in nanoscale phase-change memory cells. *Journal of Applied Physics* **119**, 025704 (2016).
155. Ielmini, D., Lavizzari, S., Sharma, D. & Lacaita, A. L. Physical Interpretation, Modeling and Impact on Phase Change Memory (PCM) Reliability of Resistance Drift Due to Chalcogenide Structural Relaxation. *2007 IEEE International Electron Devices Meeting*, 939 (2007).
156. Karpov, I., Mitra, M., Kau, D., Spadini, G., Kryukov, Y. & Karpov, V. Fundamental drift of parameters in chalcogenide phase change memory. *Journal of Applied Physics* **102**, 124503 (2007).
157. Redaelli, A., Pirovano, A., Benvenuti, A. & Lacaita, A. L. Threshold switching and phase transition numerical models for phase change memory simulations. *Journal of Applied Physics* **103**, 111101 (2008).
158. Salinga, M., Carria, E., Kaldenbach, A., Bornhöfft, M., Benke, J., Mayer, J. & Wuttig, M. Measurement of crystal growth velocity in a melt-quenched phase-change material. *Nature Communications* **4**, 2371 (2013).
159. Nardone, M., Kozub, V. I., Karpov, I. V. & Karpov, V. G. Possible mechanisms for $1/f$ noise in chalcogenide glasses: A theoretical description. *Physical Review B* **79**, 165206 (2009).
160. Frémaux, N. & Gerstner, W. Neuromodulated spike-timing-dependent plasticity, and theory of three-factor learning rules. *Front. Neur. Circ.* **9**, 85 (2016).
161. Sacramento, J., Costa, R. P., Bengio, Y. & Senn, W. *Dendritic cortical microcircuits approximate the backpropagation algorithm* in *Advances in neural information processing systems* (2018), 8721.
162. Pozzi, I., Bohté, S. & Roelfsema, P. A Biologically Plausible Learning Rule for Deep Learning in the Brain. *arXiv* (2018).
163. Sussillo, D. & Abbott, L. Generating coherent patterns of activity from chaotic neural networks. *Neuron* **63**, 544 (2009).

164. Nicola, W. & Clopath, C. Supervised Learning in Spiking Neural Networks with FORCE Training. *Nature Communications* **8**, 2208 (2017).
165. Neftci, E. O., Mostafa, H. & Zenke, F. Surrogate gradient learning in spiking neural networks: Bringing the power of gradient-based optimization to spiking neural networks. *IEEE Signal Processing Magazine* **36**, 51 (2019).
166. Lee, J. H., Delbruck, T. & Pfeiffer, M. Training Deep Spiking Neural Networks Using Backpropagation. *Frontiers in Neuroscience* **10**, 508 (2016).
167. Hochreiter, S. & Schmidhuber, J. Long short-term memory. *Neural computation* **9**, 1735 (1997).
168. Qiao, N., Mostafa, H., Corradi, F., Osswald, M., Stefanini, F., Sumislawska, D. & Indiveri, G. A reconfigurable on-line learning spiking neuromorphic processor comprising 256 neurons and 128K synapses. *Frontiers in neuroscience* **9**, 141 (2015).
169. Payvand, M., Muller, L. K. & Indiveri, G. *Event-based circuits for controlling stochastic learning with memristive devices in neuromorphic architectures in Circuits and Systems (ISCAS), 2018 IEEE International Symposium on* (2018), 1.
170. Nair, M. V., Mueller, L. K. & Indiveri, G. A differential memristive synapse circuit for on-line learning in neuromorphic computing systems. *Nano Futures* **1**, 1 (2017).
171. Balles, L., Pedregosa, F. & Roux, N. L. The Geometry of Sign Gradient Descent. *arXiv* (2020).
172. Nair, M. V. & Dudek, P. *Gradient-descent-based learning in memristive crossbar arrays in International Joint Conference on Neural Networks (IJCNN)* (2015), 1.
173. Müller, L., Nair, M. & Indiveri, G. *Randomized Unregulated Step Descent for Limited Precision Synaptic Elements in International Symposium on Circuits and Systems, (ISCAS)* (2017).
174. Payvand, M., Fouda, M. E., Kurdahi, F., Eltawil, A. M. & Neftci, E. O. On-Chip Error-Triggered Learning of Multi-Layer Memristive Spiking Neural Networks. *IEEE Journal on Emerging and Selected Topics in Circuits and Systems* **10**, 522 (2020).
175. Kingma, D. P. & Ba, J. Adam: A method for stochastic optimization. *arXiv preprint arXiv:1412.6980* (2014).
176. Athmanathan, A., Stanisavljevic, M., Papandreou, N., Pozidis, H. & Eleftheriou, E. Multilevel-Cell Phase-Change Memory: A Viable Technology. *IEEE Journal on Emerging and Selected Topics in Circuits and Systems* **6**, 87 (2016).
177. Snoek, J., Larochelle, H. & Adams, R. P. *Practical Bayesian Optimization of Machine Learning Algorithms in Proceedings of the 25th International Conference on Neural Information Processing Systems - Volume 2* (Curran Associates Inc., Lake Tahoe, Nevada, 2012), 2951.
178. Davies, M., Wild, A., Orchard, G., Sandamirskaya, Y., Guerra, G. A. F., Joshi, P., Plank, P. & Risbud, S. R. Advancing neuromorphic computing with Loihi: A survey of results and outlook. *Proceedings of the IEEE* **109**, 911 (2021).
179. Frenkel, C., Bol, D. & Indiveri, G. Bottom-Up and Top-Down Neural Processing Systems Design: Neuromorphic Intelligence as the Convergence of Natural and Artificial Intelligence. *arXiv preprint arXiv:2106.01288* (2021).
180. Muller, L. K. & Indiveri, G. Rounding methods for neural networks with low resolution synaptic weights. *arXiv preprint arXiv:1504.05767*, 1 (2015).
181. Frenkel, C., Legat, J.-D. & Bol, D. MorphIC: A 65-nm 738k-Synapse/mm² quad-core binary-weight digital neuromorphic processor with stochastic spike-driven online learning. *IEEE Transactions on Biomedical Circuits and Systems* **13**, 999 (2019).
182. Frenkel, C., Legat, J.-D. & Bol, D. *A 28-nm convolutional neuromorphic processor enabling online learning with spike-based retinas in 2020 IEEE International Symposium on Circuits and Systems (ISCAS)* (2020), 1.
183. Fusi, S. & Abbott, L. Limits on the memory storage capacity of bounded synapses. *Nature Neuroscience* **10**, 485 (2007).

184. Laborieux, A., Ernoult, M., Hirtzlin, T. & Querlioz, D. Synaptic metaplasticity in binarized neural networks. *Nature communications* **12**, 1 (2021).
185. Khaddam-Aljameh, R., Stanisavljevic, M., Fornet Mas, J., Karunaratne, G., Brandli, M., Liu, F., Singh, A., Muller, S. M., Egger, U., Petropoulos, A., Antonakopoulos, T., Brew, K., Choi, S., Ok, I., Lie, F. L., Saulnier, N., Chan, V., Ahsan, I., Narayanan, V., Nandakumar, S. R., Le Gallo, M., Francese, P. A., Sebastian, A. & Eleftheriou, E. HERMES-core—A 1.59-TOPS/mm² PCM on 14-nm CMOS in-memory compute core using 300-ps/LSB linearized CCO-based ADCs. *IEEE J. Solid-State Circuits* **57**, 1027 (4 2022).
186. Le Gallo, M., Sebastian, A., Cherubini, G., Giefers, H. & Eleftheriou, E. Compressed Sensing With Approximate Message Passing Using In-Memory Computing. *IEEE Trans. Electron Devices* **65**, 4304 (2018).
187. Mead, C. How we created neuromorphic engineering. *Nature Electronics* **3**, 434 (2020).
188. Chicca, E., Stefanini, F., Bartolozzi, C. & Indiveri, G. Neuromorphic electronic circuits for building autonomous cognitive systems. *Proceedings of the IEEE* **102**, 1367 (2014).
189. Indiveri, G. & Horiuchi, T. Frontiers in Neuromorphic Engineering. *Frontiers in Neuroscience* **5**, 1 (2011).
190. Mead, C. Neuromorphic Electronic Systems. *Proceedings of the IEEE* **78**, 1629 (1990).
191. Serb, A., Bill, J., Khiat, A., Berdan, R., Legenstein, R. & Prodromakis, T. Unsupervised learning in probabilistic neural networks with multi-state metal-oxide memristive synapses. *Nature Communications* **7**, 12611 (2016).
192. Li, Y., Wang, Z., Midya, R., Xia, Q. & Yang, J. J. Review of memristor devices in neuromorphic computing: materials sciences and device challenges. *Journal of Physics D: Applied Physics* **51**, 503002 (2018).
193. Spiga, S., Sebastian, A., Querlioz, D. & Rajendran, B. in *Memristive Devices for Brain-Inspired Computing* (eds Spiga, S., Sebastian, A., Querlioz, D. & Rajendran, B.) 3 (Woodhead Publishing, 2020).
194. Payvand, M. & Indiveri, G. *Spike-Based Plasticity Circuits for Always-on On-Line Learning in Neuromorphic Systems* in *IEEE International Symposium on Circuits and Systems (ISCAS)* (2019), 1.
195. Widrow, B. & Hoff, M. *Adaptive Switching Circuits* in *1960 IRE WESCON Convention Record, Part 4* (IRE, New York, 1960), 96.
196. Payvand, M., Fouda, M. E., Kurdahi, F., Eltawil, A. & Neftci, E. O. *Error-triggered three-factor learning dynamics for crossbar arrays* in *International Conference on Artificial Intelligence Circuits and Systems (AICAS)* (2020), 218.
197. Gerstner, W., Lehmann, M., Liakoni, V., Corneil, D. & Brea, J. Eligibility traces and plasticity on behavioral time scales: experimental support of neohebbian three-factor learning rules. *Front. Neur. Circ.* **12**, 53 (2018).
198. Neftci, E. O. Data and Power Efficient Intelligence with Neuromorphic Learning Machines. *iScience* **5**, 52 (2018).
199. Sanhueza, M. & Lisman, J. The CaMKII/NMDAR complex as a molecular memory. *Molecular brain* **6**, 1 (2013).
200. Rumelhart, D. E., Hinton, G. E. & Williams, R. J. Learning representations by back-propagating errors. *Nature* **323**, 533 (1986).
201. Qiao, N., Bartolozzi, C. & Indiveri, G. An Ultralow Leakage Synaptic Scaling Homeostatic Plasticity Circuit With Configurable Time Scales up to 100 ks. *IEEE Transactions on Biomedical Circuits and Systems* (2017).
202. Bartolozzi, C. & Indiveri, G. Synaptic dynamics in analog VLSI. *Neural Computation* **19**, 2581 (2007).

203. Bartolozzi, C., Mitra, S. & Indiveri, G. *An ultra low power current-mode filter for neuromorphic systems and biomedical signal processing* in *2006 IEEE Biomedical Circuits and Systems Conference 2006 IEEE Biomedical Circuits and Systems Conference - Healthcare Technology (BioCas)* London, UK (IEEE, 2006), 130.
204. Saxena, V. & Baker, R. J. *Compensation of CMOS op-amps using split-length transistors in Circuits and Systems (MWSCAS), 2008 IEEE 51st International Midwest Symposium on* (2008), 109.
205. Garofolo, John S., Lamel, Lori F., Fisher, William M., Pallett, David S., Dahlgren, Nancy L., Zue, Victor & Fiscus, Jonathan G. *TIMIT Acoustic-Phonetic Continuous Speech Corpus* 1993.
206. Cramer, B., Stradmann, Y., Schemmel, J. & Zenke, F. The Heidelberg spiking data sets for the systematic evaluation of spiking neural networks. *IEEE Transactions on Neural Networks and Learning Systems* (2020).
207. Xiao, H., Rasul, K. & Vollgraf, R. Fashion-MNIST: A novel image dataset for benchmarking machine learning algorithms. *arXiv [cs.LG]* (2017).
208. Orchard, G., Jayawant, A., Cohen, G. K. & Thakor, N. Converting Static Image Datasets to Spiking Neuromorphic Datasets Using Saccades. *Frontiers in Neuroscience* **9** (2015).
209. Krizhevsky, A. *Learning multiple layers of features from tiny images* research rep. (2009).
210. Deng, J., Dong, W., Socher, R., Li, L.-J., Li, K. & Fei-Fei, L. *ImageNet: A large-scale hierarchical image database* in *2009 IEEE Conference on Computer Vision and Pattern Recognition* (IEEE, 2009).
211. Sutton, R. S. & Barto, A. G. *Reinforcement learning: an introduction* (MIT Press, Cambridge, Mass, 1998).
212. Wawrzyński, P. & Tanwani, A. K. Autonomous reinforcement learning with experience replay. *Neural Networks* **41**, 156 (2013).
213. Lehmann, M. P., Xu, H. A., Liakoni, V., Herzog, M. H., Gerstner, W. & Preuschoff, K. One-shot learning and behavioral eligibility traces in sequential decision making. *Elife* **8**, e47463 (2019).
214. Lisman, J. A mechanism for the Hebb and the anti-Hebb processes underlying learning and memory. *Proc. Natl. Acad. Sci. U. S. A.* **86**, 9574 (23 1989).
215. Shouval, H. Z., Bear, M. F. & Cooper, L. N. A unified model of NMDA receptor-dependent bidirectional synaptic plasticity. *Proceedings of the National Academy of Sciences* **99**, 10831 (16 2002).
216. Bosch, M., Castro, J., Saneyoshi, T., Matsuno, H., Sur, M. & Hayashi, Y. Structural and Molecular Remodeling of Dendritic Spine Substructures during Long-Term Potentiation. *Neuron* **82**, 444 (2 2014).
217. He, K., Huertas, M., Hong, S. Z., Tie, X., Hell, J. W., Shouval, H. & Kirkwood, A. Distinct Eligibility Traces for LTP and LTD in Cortical Synapses. *Neuron* **88**, 528 (3 2015).
218. Brzosko, Z., Schultz, W. & Paulsen, O. Retroactive modulation of spike timing-dependent plasticity by dopamine. *eLife* **4**, e09685 (2015).
219. Ielmini, D., Lavizzari, S., Sharma, D. & Lacaita, A. L. Temperature acceleration of structural relaxation in amorphous Ge 2 Sb 2 Te 5. *Applied Physics Letters* **92**, 193511 (2008).
220. Pirovano, A., Lacaita, A. L., Pellizzer, F., Kostylev, S. A., Benvenuti, A. & Bez, R. Low-field amorphous state resistance and threshold voltage drift in chalcogenide materials. *IEEE Transactions on Electron Devices* **51**, 714 (2004).
221. Kim, S., Lee, B., Asheghi, M., Hurkx, F., Reifenberg, J. P., Goodson, K. E. & Wong, H.-S. P. Resistance and threshold switching voltage drift behavior in phase-change memory and their temperature dependence at microsecond time scales studied using a micro-thermal stage. *IEEE Transactions on Electron Devices* **58**, 584 (2011).

222. Demirag, Y. *Multiphysics modeling of Ge₂Sb₂Te₅ based synaptic devices for brain inspired computing* MA thesis (Ihsan Dogramaci Bilkent University, Ankara, Turkey, 2018).
223. Brader, J. M., Senn, W. & Fusi, S. Learning real-world stimuli in a neural network with spike-driven synaptic dynamics. *Neural Computation* **19**, 2881 (2007).
224. Delbruck, T. & Mead, C. *Bump circuits* in *Proceedings of International Joint Conference on Neural Networks* **1** (1993), 475.
225. Liu, S.-C., Kramer, J., Indiveri, G., Delbruck, T. & Douglas, R. *Analog VLSI: Circuits and Principles* (MIT Press, 2002).
226. Rubino, A., Payvand, M. & Indiveri, G. *Ultra-Low Power Silicon Neuron Circuit for Extreme-Edge Neuromorphic Intelligence* in *International Conference on Electronics, Circuits, and Systems, (ICECS), 2019* (2019), 458.
227. Strukov, D. B., Snider, G. S., Stewart, D. R. & Williams, R. S. The missing memristor found. *Nature* **453**, 80 (7191 2008).
228. Kumar, S., Williams, R. S. & Wang, Z. Third-order nanocircuit elements for neuromorphic engineering. *Nature* **585**, 518 (7826 2020).
229. Grollier, J., Querlioz, D., Camsari, K. Y., Everschor-Sitte, K., Fukami, S. & Stiles, M. D. Neuromorphic spintronics. *Nat. Electron.* **3**, 360 (7 2020).
230. Chua, L. Memristor-The missing circuit element. *IEEE Trans. Circuit Theory* **18**, 507 (5 1971).
231. Chicca, E., Stefanini, F., Bartolozzi, C. & Indiveri, G. Neuromorphic electronic circuits for building autonomous cognitive systems. *Proc. IEEE Inst. Electr. Electron. Eng.* **102**. Comment: Submitted to Proceedings of IEEE, spiking neural network implementations in full custom VLSI, 1367 (9 2014).
232. Cheng, Q., Song, S.-H. & Augustine, G. J. Molecular mechanisms of short-term plasticity: Role of synapsin phosphorylation in augmentation and potentiation of spontaneous glutamate release. *Front. Synaptic Neurosci.* **10**, 33 (2018).
233. Boyn, S., Grollier, J., Lecerf, G., Xu, B., Locatelli, N., Fusil, S., Girod, S., Carrétéro, C., Garcia, K., Xavier, S., Tomas, J., Bellaiche, L., Bibes, M., Barthélémy, A., Saïghi, S. & Garcia, V. Learning through ferroelectric domain dynamics in solid-state synapses. *Nat. Commun.* **8**, 14736 (1 2017).
234. Wang, Z., Joshi, S., Savel'ev, S. E., Jiang, H., Midya, R., Lin, P., Hu, M., Ge, N., Strachan, J. P., Li, Z., Wu, Q., Barnell, M., Li, G.-L., Xin, H. L., Williams, R. S., Xia, Q. & Yang, J. J. Memristors with diffusive dynamics as synaptic emulators for neuromorphic computing. *Nat. Mater.* **16**, 101 (1 2017).
235. Mehonic, A., Sebastian, A., Rajendran, B., Simeone, O., Vasilaki, E. & Kenyon, A. J. Memristors—from in-memory computing, deep learning acceleration, and spiking neural networks to the future of neuromorphic and bio-inspired computing. *Adv. Intell. Syst.* **2**, 2000085 (11 2020).
236. Mahmoodi, M. R., Prezioso, M. & Strukov, D. B. Versatile stochastic dot product circuits based on nonvolatile memories for high performance neurocomputing and neurooptimization. *Nat. Commun.* **10**, 5113 (1 2019).
237. Karunaratne, G., Le Gallo, M., Cherubini, G., Benini, L., Rahimi, A. & Sebastian, A. In-memory hyperdimensional computing. *Nat. Electron.* **3**, 327 (6 2020).
238. Tuma, T., Pantazi, A., Le Gallo, M., Sebastian, A. & Eleftheriou, E. Stochastic phase-change neurons. *Nat. Nanotechnol.* **11**, 693 (8 2016).
239. Appeltant, L., Soriano, M. C., Van der Sande, G., Danckaert, J., Massar, S., Dambre, J., Schrauwen, B., Mirasso, C. R. & Fischer, I. Information processing using a single dynamical node as complex system. *Nat. Commun.* **2**, 468 (1 2011).
240. Zhu, X., Wang, Q. & Lu, W. D. Memristor networks for real-time neural activity analysis. *Nat. Commun.* **11**, 2439 (1 2020).

241. Ninan, I. & Arancio, O. Presynaptic CaMKII is necessary for synaptic plasticity in cultured hippocampal neurons. *Neuron* **42**, 129 (1 2004).
242. Yang, J. J., Strukov, D. B. & Stewart, D. R. Memristive devices for computing. *Nat. Nanotechnol.* **8**, 13 (1 2013).
243. Midya, R., Wang, Z., Asapu, S., Joshi, S., Li, Y., Zhuo, Y., Song, W., Jiang, H., Upadhyay, N., Rao, M., Lin, P., Li, C., Xia, Q. & Yang, J. J. Artificial neural network (ANN) to spiking neural network (SNN) converters based on diffusive memristors. *Adv. Electron. Mater.* **5**, 1900060 (9 2019).
244. Yang, K., Li, F., Veeramalai, C. P. & Guo, T. A facile synthesis of CH₃NH₃PbBr₃ perovskite quantum dots and their application in flexible nonvolatile memory. *Appl. Phys. Lett.* **110**, 083102 (8 2017).
245. Jeong, J., Kim, M., Seo, J., Lu, H., Ahlawat, P., Mishra, A., Yang, Y., Hope, M. A., Eickemeyer, F. T., Kim, M., Yoon, Y. J., Choi, I. W., Darwich, B. P., Choi, S. J., Jo, Y., Lee, J. H., Walker, B., Zakeeruddin, S. M., Emsley, L., Rothlisberger, U., Hagfeldt, A., Kim, D. S., Grätzel, M. & Kim, J. Y. Pseudo-halide anion engineering for α -FAPbI₃ perovskite solar cells. *Nature* **592**, 381 (7854 2021).
246. Hassan, Y., Park, J. H., Crawford, M. L., Sadhanala, A., Lee, J., Sadighian, J. C., Mosconi, E., Shivanna, R., Radicchi, E., Jeong, M., Yang, C., Choi, H., Park, S. H., Song, M. H., De Angelis, F., Wong, C. Y., Friend, R. H., Lee, B. R. & Snaith, H. J. Ligand-engineered bandgap stability in mixed-halide perovskite LEDs. *Nature* **591**, 72 (7848 2021).
247. Protesescu, L., Yakunin, S., Bodnarchuk, M. I., Krieg, F., Caputo, R., Hendon, C. H., Yang, R. X., Walsh, A. & Kovalenko, M. V. Nanocrystals of cesium lead Halide perovskites (CsPbX₃, X = Cl, Br, and I): Novel optoelectronic materials showing bright emission with wide color gamut. *Nano Lett.* **15**, 3692 (6 2015).
248. Saidaminov, M. I., Adinolfi, V., Comin, R., Abdelhady, A. L., Peng, W., Dursun, I., Yuan, M., Hoogland, S., Sargent, E. H. & Bakr, O. M. Planar-integrated single-crystalline perovskite photodetectors. *Nat. Commun.* **6**, 8724 (1 2015).
249. Yakunin, S., Sytnyk, M., Kriegner, D., Shrestha, S., Richter, M., Matt, G. J., Azimi, H., Brabec, C. J., Stangl, J., Kovalenko, M. V. & Heiss, W. Detection of X-ray photons by solution-processed organic-inorganic perovskites. *Nat. Photonics* **9**, 444 (7 2015).
250. Wu, W., Han, X., Li, J., Wang, X., Zhang, Y., Huo, Z., Chen, Q., Sun, X., Xu, Z., Tan, Y., Pan, C. & Pan, A. Ultrathin and conformable lead Halide perovskite photodetector arrays for potential application in retina-like vision sensing. *Adv. Mater.* **33**, e2006006 (9 2021).
251. Xiao, Z. & Huang, J. Energy-efficient hybrid perovskite memristors and synaptic devices. *Adv. Electron. Mater.* **2**, 1600100 (7 2016).
252. Xu, W., Cho, H., Kim, Y.-H., Kim, Y.-T., Wolf, C., Park, C.-G. & Lee, T.-W. Organometal Halide perovskite artificial synapses. *Adv. Mater.* **28**, 5916 (28 2016).
253. John, R. A., Yantara, N., Ng, Y. F., Narasimhan, G., Mosconi, E., Meggiolaro, D., Kulkarni, M. R., Gopalakrishnan, P. K., Nguyen, C. A., De Angelis, F., Mhaisalkar, S. G., Basu, A. & Mathews, N. Ionotronic Halide perovskite drift-diffusive synapses for low-power neuromorphic computation. *Adv. Mater.* **30**, e1805454 (51 2018).
254. Lee, S., Kim, H., Kim, D. H., Kim, W. B., Lee, J. M., Choi, J., Shin, H., Han, G. S., Jang, H. W. & Jung, H. S. Tailored 2D/3D Halide perovskite heterointerface for substantially enhanced endurance in conducting bridge resistive switching memory. *ACS Appl. Mater. Interfaces* **12**, 17039 (14 2020).
255. John, R. A., Yantara, N., Ng, S. E., Patdillah, M. I. B., Kulkarni, M. R., Jamaludin, N. F., Basu, J., Ankit, Mhaisalkar, S. G., Basu, A. & Mathews, N. Diffusive and drift Halide perovskite memristive barristors as nociceptive and synaptic emulators for neuromorphic computing. *Adv. Mater.* **33**, 2007851 (15 2021).

256. Tian, H., Zhao, L., Wang, X., Yeh, Y.-W., Yao, N., Rand, B. P. & Ren, T.-L. Extremely low operating current resistive memory based on exfoliated 2D perovskite single crystals for neuromorphic computing. *ACS Nano* **11**, 12247 (12 2017).
257. Wang, Y., Lv, Z., Liao, Q., Shan, H., Chen, J., Zhou, Y., Zhou, L., Chen, X., Roy, V. A. L., Wang, Z., Xu, Z., Zeng, Y.-J. & Han, S.-T. Synergies of electrochemical metallization and valence change in all-inorganic perovskite quantum dots for resistive switching. *Adv. Mater.* **30**, e1800327 (28 2018).
258. Tan, H., Ni, Z., Peng, W., Du, S., Liu, X., Zhao, S., Li, W., Ye, Z., Xu, M., Xu, Y., Pi, X. & Yang, D. Broadband optoelectronic synaptic devices based on silicon nanocrystals for neuromorphic computing. *Nano Energy* **52**, 422 (2018).
259. Jarschel, P., Kim, J. H., Biadala, L., Berthe, M., Lambert, Y., Osgood 3rd, R. M., Patriarche, G., Grandidier, B. & Xu, J. Single-electron tunneling PbS/InP heterostructure nanoplatelets for synaptic operations. *ACS Appl. Mater. Interfaces* **13**, 38450 (32 2021).
260. Wang, Y., Lv, Z., Chen, J., Wang, Z., Zhou, Y., Zhou, L., Chen, X. & Han, S.-T. Photonic synapses based on inorganic perovskite quantum dots for neuromorphic computing. *Adv. Mater.* **30**, e1802883 (38 2018).
261. Jiang, T., Shao, Z., Fang, H., Wang, W., Zhang, Q., Wu, D., Zhang, X. & Jie, J. High-performance nanofloating gate memory based on lead Halide perovskite nanocrystals. *ACS Appl. Mater. Interfaces* **11**, 24367 (27 2019).
262. Hao, J., Kim, Y.-H., Habisreutinger, S. N., Harvey, S. P., Miller, E. M., Foradori, S. M., Arnold, M. S., Song, Z., Yan, Y., Luther, J. M. & Blackburn, J. L. Low-energy room-temperature optical switching in mixed-dimensionality nanoscale perovskite heterojunctions. *Sci. Adv.* **7** (18 2021).
263. Subramanian Periyal, S., Jagadeeswararao, M., Ng, S. E., John, R. A. & Mathews, N. Halide perovskite quantum dots photosensitized-amorphous oxide transistors for multimodal synapses. *Adv. Mater. Technol.* **5**, 2000514 (11 2020).
264. Xiao, X., Hu, J., Tang, S., Yan, K., Gao, B., Chen, H. & Zou, D. Recent advances in Halide perovskite memristors: Materials, structures, mechanisms, and applications. *Adv. Mater. Technol.* **5**, 1900914 (6 2020).
265. Xiao, Z., Yuan, Y., Shao, Y., Wang, Q., Dong, Q., Bi, C., Sharma, P., Gruverman, A. & Huang, J. Giant switchable photovoltaic effect in organometal trihalide perovskite devices. *Nat. Mater.* **14**, 193 (2 2015).
266. Chen, L.-W., Wang, W.-C., Ko, S.-H., Chen, C.-Y., Hsu, C.-T., Chiao, F.-C., Chen, T.-W., Wu, K.-C. & Lin, H.-W. Highly uniform all-vacuum-deposited inorganic perovskite artificial synapses for reservoir computing. *Adv. Intell. Syst.* **3**, 2000196 (1 2021).
267. Midya, R., Wang, Z., Zhang, J., Savel'ev, S. E., Li, C., Rao, M., Jang, M. H., Joshi, S., Jiang, H., Lin, P., Norris, K., Ge, N., Wu, Q., Barnell, M., Li, Z., Xin, H. L., Williams, R. S., Xia, Q. & Yang, J. J. Anatomy of Ag/Hafnia-based selectors with 1010 nonlinearity. *Adv. Mater.* **29** (12 2017).
268. Wang, Z., Rao, M., Midya, R., Joshi, S., Jiang, H., Lin, P., Song, W., Asapu, S., Zhuo, Y., Li, C., Wu, H., Xia, Q. & Yang, J. J. Threshold switching of Ag or Cu in dielectrics: Materials, mechanism, and applications. *Adv. Funct. Mater.* **28**, 1704862 (6 2018).
269. Guo, M. Q., Chen, Y. C., Lin, C. Y., Chang, Y. F., Fowler, B., Li, Q. Q., Lee, J. & Zhao, Y. G. Unidirectional threshold resistive switching in Au/NiO/Nb:SrTiO₃ devices. *Appl. Phys. Lett.* **110**, 233504 (23 2017).
270. Du, C., Cai, F., Zidan, M. A., Ma, W., Lee, S. H. & Lu, W. D. Reservoir computing using dynamic memristors for temporal information processing. *Nat. Commun.* **8**, 2204 (1 2017).
271. Gibbons, T. E. *Unifying quality metrics for reservoir networks* in *The 2010 International Joint Conference on Neural Networks (IJCNN)* 2010 International Joint Conference on Neural Networks (IJCNN)Barcelona, Spain (IEEE, 2010), 1.

272. Suri, M., Bichler, O., Querlioz, D., Cueto, O., Perniola, L., Sousa, V., Vuillaume, D., Gamrat, C. & DeSalvo, B. *Phase change memory as synapse for ultra-dense neuromorphic systems: Application to complex visual pattern extraction in 2011 International Electron Devices Meeting 2011 IEEE International Electron Devices Meeting (IEDM) Washington, DC, USA (IEEE, 2011)*, 4.4.1.
273. Hu, M., Strachan, J. P., Li, Z., Grafals, E. M., Davila, N., Graves, C., Lam, S., Ge, N., Yang, J. J. & Williams, R. S. *Dot-product engine for neuromorphic computing: programming 1T1M crossbar to accelerate matrix-vector multiplication in Proceedings of the 53rd Annual Design Automation Conference DAC '16: The 53rd Annual Design Automation Conference 2016 Austin Texas (ACM, New York, NY, USA, 2016)*, 1.
274. Boybat, I., Le Gallo, M., Nandakumar, S. R., Moraitis, T., Parnell, T., Tuma, T., Rajendran, B., Leblebici, Y., Sebastian, A. & Eleftheriou, E. Neuromorphic computing with multi-memristive synapses. *Nat. Commun.* **9**, 2514 (1 2018).
275. Sun, X., Wang, N., Chen, C.-Y., Ni, J., Agrawal, A., Cui, X., Venkataramani, S., El Maghraoui, K., Srinivasan, V. (& Gopalakrishnan, K. *Ultra-Low Precision 4-bit Training of Deep Neural Networks in Advances in Neural Information Processing Systems* (eds Larochelle, H., Ranzato, M., Hadsell, R., Balcan, M. F. & Lin, H.) **33** (Curran Associates, Inc., 2020), 1796.
276. Payvand, M., Demirag, Y., Dalgaty, T., Vianello, E. & Indiveri, G. *Analog weight updates with compliance current modulation of binary ReRAMs for on-chip learning in 2020 IEEE International Symposium on Circuits and Systems (ISCAS) 2020 IEEE International Symposium on Circuits and Systems (ISCAS) Seville, Spain.* **00** (IEEE, 2020), 1.
277. Tanaka, G., Yamane, T., Héroux, J. B., Nakane, R., Kanazawa, N., Takeda, S., Numata, H., Nakano, D. & Hirose, A. Recent advances in physical reservoir computing: A review. *Neural Netw.* **115**, 100 (2019).
278. Gerstner, W., Kistler, W. M., Naud, R. & Paninski, L. *Neuronal Dynamics: From Single Neurons to Networks and Models of Cognition* 590 pp. (Cambridge University Press, Cambridge, England, 2014).
279. Watts, D. J. & Strogatz, S. H. Collective dynamics of 'small-world' networks. *Nature* **393**, 440 (1998).
280. Kawai, Y., Park, J. & Asada, M. A small-world topology enhances the echo state property and signal propagation in reservoir computing. *Neural Networks* **112**, 15 (2019).
281. Loeffler, A., Zhu, R., Hochstetter, J., Li, M., Fu, K., Diaz-Alvarez, A., Nakayama, T., Shine, J. M. & Kuncic, Z. Topological Properties of Neuromorphic Nanowire Networks. *Frontiers in Neuroscience* **14**, 184 (2020).
282. Park, H.-J. & Friston, K. Structural and Functional Brain Networks: From Connections to Cognition. *Science* **342** (2013).
283. Gallos, L. K., Makse, H. A. & Sigman, M. A small world of weak ties provides optimal global integration of self-similar modules in functional brain networks. *Proceedings of the National Academy of Sciences* **109**, 2825 (2012).
284. Sporns, O. & Zwi, J. D. The Small World of the Cerebral Cortex. *Neuroinformatics* **2**, 145 (2004).
285. Bullmore, E. & Sporns, O. Complex brain networks: graph theoretical analysis of structural and functional systems. *Nature Reviews Neuroscience* **10**, 186 (2009).
286. Bullmore, E. & Sporns, O. Complex brain networks: graph theoretical analysis of structural and functional systems. *Nature Reviews Neuroscience* **10**, 186 (2009).
287. Hasler, J. Large-scale field-programmable analog arrays. *Proceedings of the IEEE* **108**, 1283 (2019).
288. Jo, S. H., Chang, T., Ebong, I., Bhadviya, B. B., Mazumder, P. & Lu, W. Nanoscale memristor device as synapse in neuromorphic systems. *Nano letters* **10**, 1297 (2010).
289. Ielmini, D. & Waser, R. *Resistive Switching: From Fundamentals of Nanoionic Redox Processes to Memristive Device Applications* (John Wiley & Sons, 2015).

290. Strukov, D., Indiveri, G., Grollier, J. & Fusi, S. Building brain-inspired computing. *Nature Communications* **10** (2019).
291. Kingra, S. K., Parmar, V., Chang, C.-C., Hudec, B., Hou, T.-H. & Suri, M. SLIM: Simultaneous Logic-In-Memory computing exploiting bilayer analog OxRAM devices. *Scientific Reports* **10**, 1 (2020).
292. Woźniak, S., Pantazi, A., Bohnstingl, T. & Eleftheriou, E. Deep learning incorporating biologically inspired neural dynamics and in-memory computing. *Nature Machine Intelligence* **2**, 325 (2020).
293. Ambrogio, S., Narayanan, P., Okazaki, A., Fasoli, A., Mackin, C., Hosokawa, K., Nomura, A., Yasuda, T., Chen, A., Friz, A., *et al.* An analog-AI chip for energy-efficient speech recognition and transcription. *Nature* **620**, 768 (2023).
294. Le Gallo, M., Khaddam-Aljameh, R., Stanisavljevic, M., Vasilopoulos, A., Kersting, B., Dazzi, M., Karunaratne, G., Brändli, M., Singh, A., Müller, S. M., *et al.* A 64-core mixed-signal in-memory compute chip based on phase-change memory for deep neural network inference. *Nature Electronics* **6**, 680 (2023).
295. Sebastian, A., Le Gallo, M., Khaddam-Aljameh, R. & Eleftheriou, E. Memory devices and applications for in-memory computing. *Nature Nanotechnology* **15**, 529 (2020).
296. Jouppi, N. P., Young, C., Patil, N., Patterson, D., Agrawal, G., Bajwa, R., Bates, S., Bhatia, S., Boden, N., Borchers, A., *et al.* In-datacenter performance analysis of a Tensor Processing Unit in *Proceedings of the 44th annual international symposium on computer architecture* (2017), 1.
297. Yu, S., Sun, X., Peng, X. & Huang, S. Compute-in-memory with emerging nonvolatile-memories: challenges and prospects in 2020 *IEEE Custom Integrated Circuits Conference (CICC)* (2020), 1.
298. Joksas, D., Freitas, P., Chai, Z., Ng, W., Buckwell, M., Li, C., Zhang, W., Xia, Q., Kenyon, A. & Mehonic, A. Committee machines—a universal method to deal with non-idealities in memristor-based neural networks. *Nature Communications* **11**, 1 (2020).
299. Zidan, M. A., Strachan, J. P. & Lu, W. D. The future of electronics based on memristive systems. *Nature Electronics* **1**, 22 (2018).
300. Mannocci, P., Farronato, M., Lepri, N., Cattaneo, L., Glukhov, A., Sun, Z. & Ielmini, D. In-memory computing with emerging memory devices: Status and outlook. *APL Machine Learning* **1** (2023).
301. Duan, S., Hu, X., Dong, Z., Wang, L. & Mazumder, P. Memristor-based cellular nonlinear/neural network: design, analysis, and applications. *IEEE Transactions on Neural Networks and Learning Systems* **26**, 1202 (2014).
302. Ascoli, A., Messaris, I., Tetzlaff, R. & Chua, L. O. Theoretical foundations of memristor cellular nonlinear networks: Stability analysis with dynamic memristors. *IEEE Transactions on Circuits and Systems I: Regular Papers* **67**, 1389 (2019).
303. Wang, R., Shi, T., Zhang, X., Wei, J., Lu, J., Zhu, J., Wu, Z., Liu, Q. & Liu, M. Implementing in-situ self-organizing maps with memristor crossbar arrays for data mining and optimization. *Nature Communications* **13**, 1 (2022).
304. Likharev, K., Mayr, A., Muckra, I. & Türel, Ö. CrossNets: High-performance neuromorphic architectures for CMOL circuits. *Annals of the New York Academy of Sciences* **1006**, 146 (2003).
305. Betta, G., Graffi, S., Kovacs, Z. M. & Masetti, G. CMOS implementation of an analogically programmable cellular neural network. *IEEE Transactions on Circuits and Systems II: Analog and Digital Signal Processing* **40**, 206 (1993).
306. Khacef, L., Rodriguez, L. & Miramond, B. Brain-inspired self-organization with cellular neuromorphic computing for multimodal unsupervised learning. *Electronics* **9**, 1605 (2020).
307. Lin, P., Pi, S. & Xia, Q. 3D integration of planar crossbar memristive devices with CMOS substrate. *Nanotechnology* **25**, 405202 (2014).

308. Boahen, K., Nomura, M., Ros Vidal, E. & Van Rullen, R. *Address-Event Senders and Receivers: Implementing Direction-Selectivity and Orientation-Tuning* (eds Cohen, A., Douglas, R., Horiuchi, T., Indiveri, G., Koch, C., Sejnowski, T. & Shamma, S.) 1998.
309. Park, J., Yu, T., Joshi, S., Maier, C. & Cauwenberghs, G. Hierarchical address event routing for reconfigurable large-scale neuromorphic systems. *IEEE transactions on neural networks and learning systems* **28**, 2408 (2016).
310. Cai, F., Kumar, S., Van Vaerenbergh, T., Sheng, X., Liu, R., Li, C., Liu, Z., Foltin, M., Yu, S., Xia, Q., *et al.* Power-efficient combinatorial optimization using intrinsic noise in memristor Hopfield neural networks. *Nature Electronics* **3**, 409 (2020).
311. Bartolozzi, C. & Indiveri, G. Synaptic dynamics in analog VLSI. *Neural computation* **19**, 2581 (2007).
312. Esmanhotto, E., Brunet, L., Castellani, N., Bonnet, D., Dalgaty, T., Grenouillet, L., Ly, D., Cagli, C., Vizioz, C., Allouti, N., *et al.* *High-Density 3D Monolithically Integrated Multiple 1T1R Multi-Level-Cell for Neural Networks in 2020 IEEE International Electron Devices Meeting (IEDM)* (2020), 36.
313. Chen, J., Wu, C., Indiveri, G. & Payvand, M. *Reliability Analysis of Memristor Crossbar Routers: Collisions and On/off Ratio Requirement in 2022 29th IEEE International Conference on Electronics, Circuits and Systems (ICECS)* (2022), 1.
314. Werbos, P. J. Backpropagation through time: What it does and how to do it. *Proceedings of the IEEE* **78**, 1550 (1990).
315. Dalgaty, T., Castellani, N., Turck, C., Harabi, K.-E., Querlioz, D. & Vianello, E. In situ learning using intrinsic memristor variability via Markov chain Monte Carlo sampling. *Nature Electronics* **4**, 151 (2021).
316. Zhao, M., Wu, H., Gao, B., Zhang, Q., Wu, W., Wang, S., Xi, Y., Wu, D., Deng, N., Yu, S., Chen, H.-Y. & Qian, H. *Investigation of statistical retention of filamentary analog RRAM for neuromorphic computing in 2017 IEEE International Electron Devices Meeting (IEDM)* (2017), 39.4.1.
317. Moro, F., Esmanhotto, E., Hirtzlin, T., Castellani, N., Trabelsi, A., Dalgaty, T., Molas, G., Andrieu, F., Brivio, S., Spiga, S., *et al.* Hardware calibrated learning to compensate heterogeneity in analog RRAM-based Spiking Neural Networks. *IEEE International Symposium in Circuits and Systems* (2022).
318. Moody, G. B. & Mark, R. G. The impact of the MIT-BIH arrhythmia database. *IEEE Engineering in Medicine and Biology Magazine* **20**, 45 (2001).
319. Lee, H.-Y., Hsu, C.-M., Huang, S.-C., Shih, Y.-W. & Luo, C.-H. Designing low power of sigma delta modulator for biomedical application. *Biomedical Engineering: Applications, Basis and Communications* **17**, 181 (2005).
320. Corradi, F. & Indiveri, G. A neuromorphic event-based neural recording system for smart brain-machine-interfaces. *IEEE Transactions on Biomedical Circuits and Systems* **9**, 699 (2015).
321. Brockman, G., Cheung, V., Pettersson, L., Schneider, J., Schulman, J., Tang, J. & Zaremba, W. *OpenAI Gym* 2016.
322. Luo, W., Sun, P., Zhong, F., Liu, W., Zhang, T. & Wang, Y. End-to-End Active Object Tracking and Its Real-World Deployment via Reinforcement Learning. *IEEE Transactions on Pattern Analysis and Machine Intelligence* **42**, 1317 (2020).
323. Lee, J., Hwangbo, J., Wellhausen, L., Koltun, V. & Hutter, M. Learning quadrupedal locomotion over challenging terrain. *Science Robotics* **5** (2020).

324. Vinyals, O., Babuschkin, I., Czarnecki, W. M., Mathieu, M., Dudzik, A., Chung, J., Choi, D. H., Powell, R., Ewalds, T., Georgiev, P., Oh, J., Horgan, D., Kroiss, M., Danihelka, I., Huang, A., Sifre, L., Cai, T., Agapiou, J. P., Jaderberg, M., Vezhnevets, A. S., Leblond, R., Pohlen, T., Dalibard, V., Budden, D., Sulsky, Y., Molloy, J., Paine, T. L., Gulcehre, C., Wang, Z., Pfaff, T., Wu, Y., Ring, R., Yogatama, D., Wünsch, D., McKinney, K., Smith, O., Schaul, T., Lillicrap, T., Kavukcuoglu, K., Hassabis, D., Apps, C. & Silver, D. Grandmaster level in StarCraft II using multi-agent reinforcement learning. *Nature* **575**, 350 (2019).
325. OpenAI, Andrychowicz, M., Baker, B., Chociej, M., Jozefowicz, R., McGrew, B., Pachocki, J., Petron, A., Plappert, M., Powell, G., Ray, A., Schneider, J., Sidor, S., Tobin, J., Welinder, P., Weng, L. & Zaremba, W. Learning Dexterous In-Hand Manipulation. *arXiv:1808.00177 [cs, stat]* (2019).
326. Jordan, J., Schmidt, M., Senn, W. & Petrovici, M. A. Evolving interpretable plasticity for spiking networks. *eLife* **10**, e66273 (2021).
327. Rabaey, J. M., Chandrakasan, A. P. & Nikolić, B. *Digital integrated circuits: a design perspective* (Pearson education Upper Saddle River, NJ, 2003).
328. Yik, J., Ahmed, S. H., Ahmed, Z., Anderson, B., Andreou, A. G., Bartolozzi, C., Basu, A., Blanken, D. d., Bogdan, P., Bohte, S., *et al.* NeuroBench: Advancing neuromorphic computing through collaborative, fair and representative benchmarking. *arXiv preprint arXiv:2304.04640* (2023).
329. Merolla, P., Arthur, J., Alvarez, R., Bussat, J.-M. & Boahen, K. A Multicast Tree Router for Multichip Neuromorphic Systems. *Circuits and Systems I: Regular Papers, IEEE Transactions on* **61**, 820 (2014).
330. Painkras, E., Plana, L., Garside, J., Temple, S., Galluppi, F., Patterson, C., Lester, D., Brown, A. & Furber, S. SpiNNaker: A 1-W 18-Core System-on-Chip for Massively-Parallel Neural Network Simulation. *IEEE Journal of Solid-State Circuits* **48**, 1943 (2013).
331. Benjamin, B. V., Gao, P., McQuinn, E., Choudhary, S., Chandrasekaran, A. R., Bussat, J., Alvarez-Icaza, R., Arthur, J., Merolla, P. & Boahen, K. Neurogrid: A Mixed-Analog-Digital Multichip System for Large-Scale Neural Simulations. *Proceedings of the IEEE* **102**, 699 (2014).
332. Basu, A., Deng, L., Frenkel, C. & Zhang, X. *Spiking neural network integrated circuits: A review of trends and future directions in 2022 IEEE Custom Integrated Circuits Conference (CICC)* (2022), 1.
333. Pan, X., Ye, T., Xia, Z., Song, S. & Huang, G. *Slide-Transformer: Hierarchical Vision Transformer with Local Self-Attention in Proceedings of the IEEE/CVF Conference on Computer Vision and Pattern Recognition* (2023), 2082.
334. Yu, T., Li, X., Cai, Y., Sun, M. & Li, P. *S2-mlp: Spatial-shift mlp architecture for vision in Proceedings of the IEEE/CVF winter conference on applications of computer vision* (2022), 297.
335. Strother, J. A., Nern, A. & Reiser, M. B. Direct observation of ON and OFF pathways in the *Drosophila* visual system. *Current Biology* **24**, 976 (2014).
336. Davies, M., Wild, A., Orchard, G., Sandamirskaya, Y., Guerra, G. A. F., Joshi, P., Plank, P. & Risbud, S. R. Advancing neuromorphic computing with Loihi: A survey of results and outlook. *Proceedings of the IEEE* **109**, 911 (2021).
337. Dalgaty, T., Mesquida, T., Joubert, D., Sironi, A., Vivet, P. & Posch, C. *HUGNet: Hemi-Spherical Update Graph Neural Network applied to low-latency event-based optical flow in Proceedings of the IEEE/CVF Conference on Computer Vision and Pattern Recognition* (2023), 3952.
338. Aimone, J. B., Date, P., Fonseca-Guerra, G. A., Hamilton, K. E., Henke, K., Kay, B., Kenyon, G. T., Kulkarni, S. R., Mniszewski, S. M., Parsa, M., *et al.* A review of non-cognitive applications for neuromorphic computing. *Neuromorphic Computing and Engineering* **2**, 032003 (2022).
339. Dalgaty, T., Payvand, M., De Salvo, B., *et al.* *Hybrid CMOS-RRAM neurons with intrinsic plasticity in IEEE ISCAS* (2019), 1.

340. Joshi, V., Gallo, M. L., Haefeli, S., Boybat, I., Nandakumar, S. R., Piveteau, C., Dazzi, M., Rajendran, B., Sebastian, A. & Eleftheriou, E. Accurate deep neural network inference using computational phase-change memory. *Nature Communications* **11** (2020).
341. Corradi, F., Bontrager, D. & Indiveri, G. *Toward neuromorphic intelligent brain-machine interfaces: An event-based neural recording and processing system in Biomedical Circuits and Systems Conference (BioCAS)* (2014), 584.
342. Freeman, C. D., Frey, E., Raichuk, A., Girgin, S., Mordatch, I. & Bachem, O. *Brax - A Differentiable Physics Engine for Large Scale Rigid Body Simulation* version 0.0.13. 2021.
343. Zucchet, N., Meier, R., Schug, S., Mujika, A. & Sacramento, J. Online learning of long-range dependencies. *arXiv [cs.LG]* (2023).
344. Scellier, B. & Bengio, Y. Equilibrium Propagation: Bridging the gap between energy-based models and Backpropagation. *Front. Comput. Neurosci.* **11**, 24 (2017).
345. Polimeni, J. M., Mayumi, K., Giampietro, M. & Alcott, B. *The Jevons paradox and the myth of resource efficiency improvements* 200 pp. (Routledge, London, England, 2012).
346. Newman, M. & Watts, D. Renormalization group analysis of the small-world network model. *Physics Letters A* **263**, 341 (1999).
347. Zamarreño-Ramos, C., Camuñas-Mesa, L., Pérez-Carrasco, J., Masquelier, T., Serrano-Gotarredona, T. & Linares-Barranco, B. On spike-timing-dependent-plasticity, memristive devices, and building a self-learning visual cortex. *Frontiers in Neuroscience* **5**, 1 (2011).
348. Zhu, X., Lee, J. & Lu, W. D. Iodine vacancy redistribution in organic-inorganic Halide perovskite films and resistive switching effects. *Adv. Mater.* **29**, 1700527 (29 2017).
349. Nedelcu, G., Protesescu, L., Yakunin, S., Bodnarchuk, M. I., Grotevent, M. J. & Kovalenko, M. V. Fast anion-exchange in highly luminescent nanocrystals of cesium lead Halide perovskites (CsPbX₃, X = Cl, Br, I). *Nano Lett.* **15**, 5635 (8 2015).

This thesis consists of six selected publications, conducted in collaboration with electrical engineers, computer scientists, material designers and neuroscientists. In this section, I roughly discuss my personal contributions to each project.

Analog weight updates with compliance current modulation of binary ReRAMs for on-chip learning (Chapter 2)

- collaborated with material scientists for data collection and modeling (e.g., Fig. 1)
- coded training and evaluation of RRAM-based neural network simulations (e.g., Alg. 1)
- assisted circuit design with simulation findings (e.g., Fig. 2)
- contributed to majority of the manuscript including figures

Online training of spiking recurrent neural networks with Phase-Change Memory synapses (Chapter 3)

- performed literature review to identify the problem
- coded e-prop, PCM-based analog simulation framework, and neural network training
- conducted all data analysis and visualization
- contributed to majority of the manuscript including figures

Biologically-inspired training of spiking recurrent neural networks with neuromorphic hardware (Chapter 3)

- collaboratively planned the project with IBM researchers and INI (e.g., work assignments, experiments, deadlines)
- assisted with experiment datasets, architecture design following prior work [126]
- weekly supervision of Anja Šurina (e.g., debugging, hyperparameter opt...)
- assisted paper writing and designed several figures

PCM-trace: scalable synaptic eligibility traces with resistivity drift of Phase-Change Materials (Chapter 3)

- performed literature review to identify the problem
- collaborated with material scientists for data collection and modeling
- coded pcm-trace and multi-pcm trace experiments and analysis
- assisted circuit design with simulation findings
- contributed to majority of the manuscript

Reconfigurable halide perovskite nanocrystal memristors for neuromorphic computing (Chapter 4)

- performed literature review to identify the problem
- collaborated with material scientists for data collection, required device specifications and modeling (e.g. non-volatility time constant, Fig.4b-c)
- coded training and evaluation of simulations with volatile and non-volatile memristor models (e.g., RC framework)
- designed I_{CC} modulated training following prior work [276] (e.g., Supplementary Fig. 28)
- contributed to majority of the manuscript

Mosaic: in-memory computing and routing for small-world spike-based neuromorphic systems (Chapter 5)

- performed extensive literature review to identify the strengths the idea
- collaborated with material scientists for data collection and modeling (e.g., Fig. 2d)
- coded layout-aware training and evaluation of SHD with backprop and RL with ES benchmarks (e.g., Fig. 4)
- contributed to majority of the manuscript

Articles in peer-reviewed journals:

1. John, R. A., Demirag, Y., Shynkarenko, Y., Berezovska, Y., Ohannessian, N., Payvand, M., Zeng, P., Bodnarchuk, M. I., Krumeich, F., Kara, G., Shorubalko, I., Nair, M. V., Cooke, G. A., Lippert, T., Indiveri, G. & Kovalenko, M. V. Reconfigurable halide perovskite nanocrystal memristors for neuromorphic computing. *Nat. Commun.* **13**, 2074 (1 2022).
2. Dalgaty, T., Moro, F., Demirag, Y., De Pra, A., Indiveri, G., Vianello, E. & Payvand, M. Mosaic: in-memory computing and routing for small-world spike-based neuromorphic systems. *Nat. Commun.* **15**, 1 (1 2024).
3. D'Agostino, S., Moro, F., Torchet, T., Demirag, Y., Grenouillet, L., Castellani, N., Indiveri, G., Vianello, E. & Payvand, M. DenRAM: neuromorphic dendritic architecture with RRAM for efficient temporal processing with delays. *Nat. Commun.* **15**, 1 (1 2024).

Preprints:

4. Demirag, Y., Frenkel, C., Payvand, M. & Indiveri, G. *Online training of spiking recurrent neural networks with Phase-Change Memory synapses* 2021.

Conference contributions:

5. Demirag, Y., Moro, F., Dalgaty, T., Navarro, G., Frenkel, C., Indiveri, G., Vianello, E. & Payvand, M. *PCM-trace: Scalable synaptic eligibility traces with resistivity drift of phase-change materials* in 2021 IEEE International Symposium on Circuits and Systems (ISCAS) 2021 IEEE International Symposium on Circuits and Systems (ISCAS)Daegu, Korea. **00** (IEEE, 2021), 1.
6. Demirag, Y. & Indiveri, G. *Network of biologically plausible neuron models can solve motor tasks through heterogeneity* in Computational and Systems Neuroscience (COSYNE) (Lisbon, Portugal, 2024).
7. Demirag, Y., Dittmann, R., Indiveri, G. & Neftci, E. *Overcoming phase-change material non-idealities by meta-learning for adaptation on the edge* in Proceedings of Neuromorphic Materials, Devices, Circuits and Systems (NeuMatDeCaS) (2023).
8. Payvand, M., Demirag, Y., Dalgaty, T., Vianello, E. & Indiveri, G. *Analog weight updates with compliance current modulation of binary ReRAMs for on-chip learning* in 2020 IEEE International Symposium on Circuits and Systems (ISCAS) 2020 IEEE International Symposium on Circuits and Systems (ISCAS)Seville, Spain. **00** (IEEE, 2020), 1.
9. Bohnstingl, T., Surina, A., Fabre, M., Demirag, Y., Frenkel, C., Payvand, M., Indiveri, G. & Pantazi, A. *Biologically-inspired training of spiking recurrent neural networks with neuromorphic hardware* in 2022 IEEE 4th International Conference on Artificial Intelligence Circuits and Systems (AICAS) 2022 IEEE 4th International Conference on Artificial Intelligence Circuits and Systems (AICAS)Incheon, Korea, Republic of. **00** (IEEE, 2022), 218.
10. Payvand, M., D'Agostino, S., Moro, F., Demirag, Y., Indiveri, G. & Vianello, E. *Dendritic computation through exploiting resistive memory as both delays and weights* in Proceedings of the 2023 International Conference on Neuromorphic Systems International Conference on Neuromorphic Systems (ICONS) (New York, USA, 2023), 1.
11. Raghunathan, K. C., Demirag, Y., Neftci, E. & Payvand, M. *Hardware-aware Few-shot Learning on a Memristor-based Small-world Architecture* in Neuro Inspired Computational Elements Conference (NICE) (IEEE, 2024).
12. Raghunathan, K. C., Demirag, Y., Moro, F., Neftci, E. & Payvand, M. *Few-shot learning on brain-inspired small-world graphical hardware* in International Conference on Neuromorphic, Natural and Physical Computing (NNPC 2023) (Hannover, Germany, 2023).
13. Yu, Z., Bégon-Lours, L., Demirag, Y. & Offrein, B. J. *BEOL compatible cross-bar array of ferroelectric synapses* in Proceedings of the 2021 International Conference on Neuromorphic Systems International Conference on Neuromorphic Systems (ICONS) (2021).

14. Yik, J., Ahmed, S. H., Ahmed, Z., Anderson, B., Andreou, A. G., Bartolozzi, C., Basu, A., Blanken, D. d., Bogdan, P., Bohte, S., Bouhadjar, Y., Buckley, S., Cauwenberghs, G., Corradi, F., de Croon, G., Danielescu, A., Daram, A., Davies, M., Demirag, Y., Eshraghian, J., Forest, J., Furber, S., Furlong, M., Gilra, A., Indiveri, G., Joshi, S., Karia, V., Khacef, L., Knight, J. C., Kriener, L., Kubendran, R., Kudithipudi, D., Lenz, G., Manohar, R., Mayr, C., Michmizos, K., Muir, D., Neftci, E., Nowotny, T., Ottati, F., Ozelikkale, A., Pacik-Nelson, N., Panda, P., Pao-Sheng, S., Payvand, M., Pehle, C., Petrovici, M. A., Posch, C., Renner, A., Sandamirskaya, Y., Schaefer, C. J. S., van Schaik, A., Schemmel, J., Schuman, C., Seo, J.-S., Sheik, S., Shrestha, S. B., Sifalakis, M., Sironi, A., Stewart, K., Stewart, T. C., Stratmann, P., Tang, G., Timcheck, J., Verhelst, M., Vineyard, C. M., Vogginger, B., Yousefzadeh, A., Zhou, B., Zohora, F. T., Frenkel, C. & Reddi, V. J. *NeuroBench: Advancing neuromorphic computing through collaborative, fair and representative benchmarking* in (2023).